Atomic layer deposition of silicon nitride from novel precursor DSBAS and nitrogen plasma

van Drunen, M.

Award date:
2015

Technische Universiteit Eindhoven University of Technology
Department of Applied Physics
Plasma & Materials Processing

Atomic Layer Deposition of Silicon Nitride from novel precursor DSBAS and nitrogen plasma

Maarten van Drunen

September 2015 PMP 15-05

Under supervision of:

Prof.dr.ir W.M.M. Kessels

Abstract

The deposition of high-quality silicon nitride (SiN_x) layers is required in the manufacturing of state-of-the-art field-effect transistors (FETs), which are used everywhere throughout modern computing. An important application of SiN_x in FETs is as a side-wall gate spacer, where it functions as a barrier layer to protect sensitive inner layers, against for example oxygen ingress and etch processing steps. From a literature study further opportunities and applications of SiN_x films in future three-dimensional FET architectures will be discussed. It will be shown that a low thermal budget is essential for these applications of SiN_x, in addition to obtaining a high quality and a high conformality.

A novel precursor Di(*Sec*-Butyl)AminoSilane (DSBAS, $SiH_3N(C_4H_9)_2$) was employed to develop a plasma-assisted atomic layer deposition (ALD) process to grow high-quality SiN_x at low substrate temperatures. Material properties have been characterised over a wide temperature range and have been compared with properties of a similar organosilane precursor Bis(*Tert*-Butyl-Amino)Silane (BTBAS, $SiH_2[NH(C_4H_9)]_2$). Compared to the BTBAS process and other plasma-assisted ALD processes reported in the literature, the obtained growth per cycle was low. However, typically high-quality SiN_x films were obtained as was demonstrated by low wet etch-rates, low C, O, and H content, high mass densities and N/Si values close to stoichiometric Si_3N_4.

The high-quality of the SiN_x was also investigated in trenches with aspect ratio $\sim$ 1:4.5, relevant for FET applications. High quality was confirmed at horizontal surfaces in the trench, while at vertical surfaces the quality was slightly poorer. However, the conformality was proven to be not sufficient. The reduced thickness and quality at vertical side-walls also suggest that ions play a role in the quality and growth of SiN_x films.

The results in this work provide support for a growth mechanism, previously proposed for BTBAS. This mechanism explains how the split-off of the only amino-ligand in a DSBAS-molecule in the precursor half-cycle, reduces redeposition of ligand fragments in the subsequent plasma half-cycle leading to high film quality. The new insights obtained in this work have resulted in new proposed experiments, in order to further investigate the reaction mechanisms involved.

Contents

Chapter 1

Introduction

In order to prevent too much repetition between this Introduction Chapter and the introduction sections in the later chapters, some aspects will be discussed here only generally. The detailed outline will be discussed in the final section of this Introduction Chapter.

1.1 Silicon Nitride film deposition

Silicon nitride (SiN_x) is one of the most widely used materials in thin film growth. SiN_x is currently used in a variety of applications ranging from passivation layers in solar cells to encapsulation layers in displays.[1] An important application of SiN_x is as a sidewall gate spacer in Field-Effect Transistors (FETs), where it serves as a barrier layer against for example water and oxygen to which it usually is exposed in subsequent processing steps[2]. SiN_x can also be important in defining source and drain, in strain engineering where it can increase the channel mobility or as a hard mask in spacer defined patterning.[2–7] However, obtaining SiN_x films suited for these applications is not trivial. Since FET architectures are currently transforming into three-dimensional structures, it is important that the SiN_x film thickness is uniform throughout high-aspect-ratio structures (HARS), of which the conformality is a measure. In order to successfully apply SiN_x as a sidewall gate spacer in increasingly smaller and faster transistors, methods need to be developed to deposit conformal SiN_x films of high quality at low deposition temperatures.[7,8] These challenges for SiN_x films applied in FETs will be further discussed in Chapter 2.

1.1.1 Chemical Vapour Deposition

A suitable way to grow such SiN_x films is by using Chemical Vapour Deposition (CVD). In CVD based processes one or multiple molecules react on a target substrate surface in order to produce thin films. Typically in such processes, a precursor and a reactant are involved. A precursor can basically be any gas-phase-species which can be used to grow SiN_x films. As reactant, other gas-phase-species can be used, but for example also a plasma. In CVD processes, both precursor as the reactant are present in the reactor simultaneously. Traditionally, either low-pressure CVD or plasma-enhanced CVD processes were employed in order to grow SiN_x spacer layers.[9] Low-pressure CVD typically requires high substrate temperatures ($\sim$ 750 °C) though, which is not preferred in SiN_x spacer manufacturing processes. Plasma-enhanced CVD can be used as an alternative, since typically low substrate temperatures ($\sim$ 400 °C) are required for film growth.[10] However, typically reduced conformality is reported with plasma-assisted CVD compared to low-pressure CVD. Furthermore, all CVD processes typically suffer from loading conditions, meaning film growth is influenced by loading conditions, such as gas flow, wafer characteristics and amount of gas species present.[11]

1.1.2 Plasma-assisted atomic layer deposition

Atomic Layer Deposition (ALD) is an excellent deposition technique to grow such films in a more controlled way. ALD is a cyclic growth method via which ultra thin layers can be grown, while being able to control film thickness precisely. A typical ALD cycle consists of two self-limiting half-cycles with sub-monolayer growth per cycle (GPC), which is schematically depicted in Figure 1.1. Every cycle (and consequently the first half-cycle) starts with a reaction of gas-phase-species, or precursor, with reactive species at the surface. In the case of SiN_x film growth, the silicon precursor bonds to groups which contain nitrogen atoms at the surface. When the available precursor molecules have adsorbed to all available reactive surface sites, no further reactions can happen, which leads to the specific self-limiting feature of ALD. After this precursor step, the reactor is purged to ensure all precursor molecules or precursor fragments leave the reactor. In case of plasma-assisted ALD, in the second half-cycle a plasma is ignited which serves as the reactant. In this work, a nitrogen (N_2) plasma serves as the reactant. The various reactive species created in the plasma can potentially contribute to surface chemistry and film growth. The main function of the plasma is to create reactive surface sites, onto which the precursor can adsorb in the next half-cycle. After growth has again saturated in this step, a new purge step ensures that all species in the reactor are purged out of the reactor. The second half-cycle, and consequently the total cycle, is now completed.

Typically every cycle a virtually constant number of atoms adsorb on the surface, leading to very linear growth behaviour as function of the amount of deposition cycles, which is shown in Figure 1.2. In this figure it can also be seen that by varying temperature the slope of the plots, which corresponds to the GPC, varies slightly, demonstrating the thickness control that is possible by carefully selecting deposition conditions and the amount of deposition cycles.

Traditionally thermal ALD processes have been tried in order to grow thin SiN_x films. In thermal

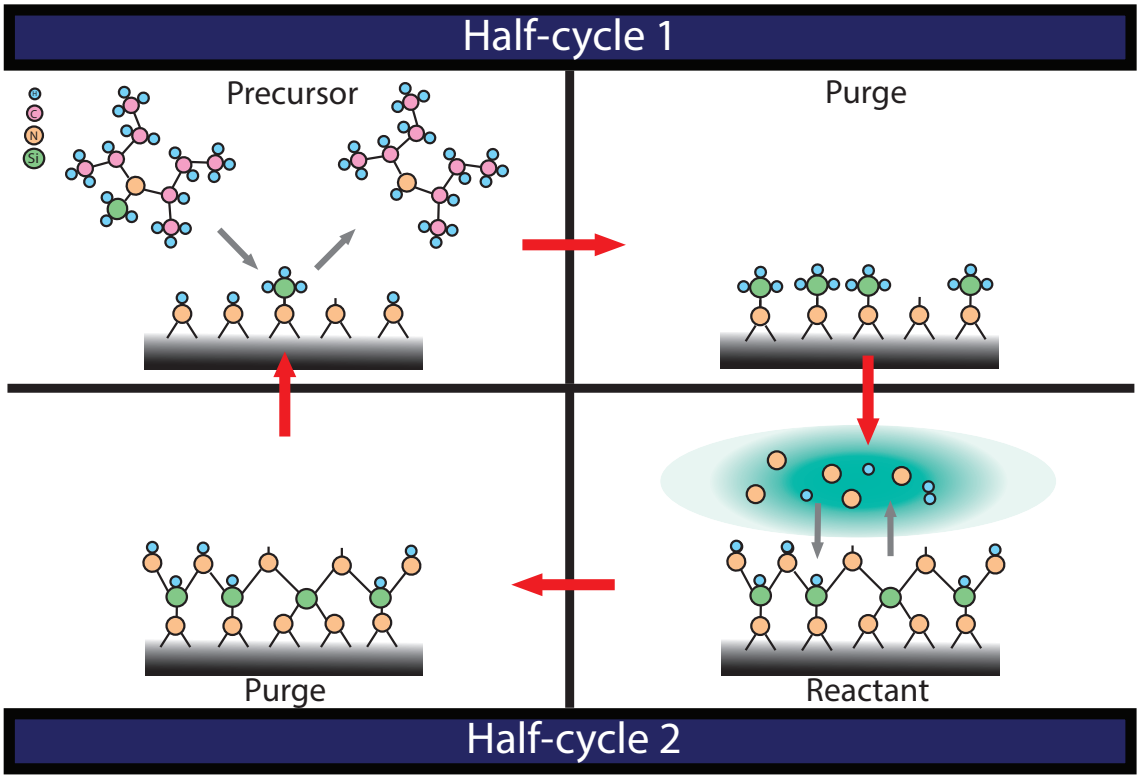

Figure 1.1: Schematic and simplified representation of an ALD cycle using a precursor and a plasma as reactant. To illustrate the ALD cycle, the case with DSBAS as precursor and a nitrogen plasma is chosen. The DSBAS precursor reacts in a self-limiting way with reactive surface sites, after which the reactor is purged. Then the reactive plasma species react with the silicon species at the surface, after which the reactor is purged again and the cycle is completed.

ALD processes, both precursor and reactant are gas-phase-species necessary to grow SiN_x films. In thermal ALD the reactions of the gas-phase-species with the surface species are driven by the substrate temperature. For several thermal ALD processes though, similarly as in low-pressure CVD processes, thermal reactions cannot provide the film quality and low contamination content that is required.[1] The use of radicals, ions and other energetic species in plasmas allow for unique surface chemistries that are ruled by reactive species. It has been shown by Profijt *et al.*[12] that the use of the plasma enables a wider choice of materials, substrate temperatures and processing conditions.

1.2 Plasma-assisted ALD processes for SiN_x: precursors and plasmas

Various plasma-assisted ALD processes have been developed and applied in order to deposit SiN_x films, using a variety of precursors and plasmas.[1,2,8,13,14] In this brief overview, we will mention

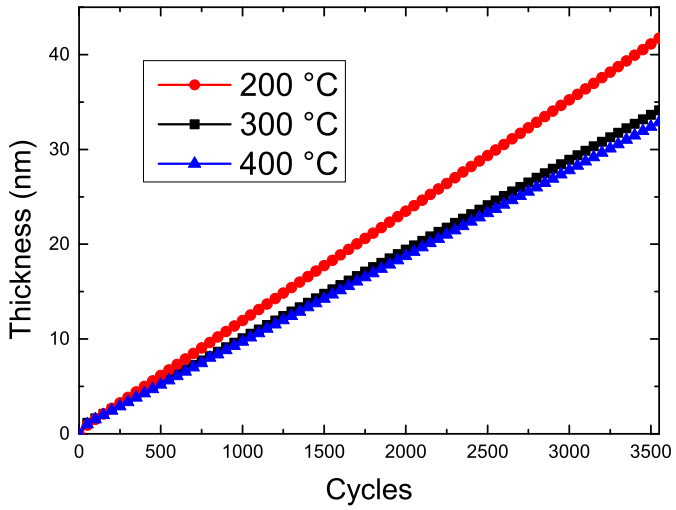

Figure 1.2: Thickness as function of the number of atomic layer deposition (ALD) cycles, as measured with *in-situ* spectroscopic ellipsometry (SE) for three different stage temperatures. The data is for SiN_x films deposited by DSBAS.

the different sorts of precursors used in plasma-assisted ALD processes, which have been reported in literature, accompanied by important process or material characteristics. In the introduction sections of Chapter 4 about Process Development and Chapter 5 about Conformality, these aspects will be covered as well, with a focus on the topic of the chapter.

The precursors most commonly employed for plasma-assisted ALD of SiN_x films can be classified as either silicon hydrides, silylamine, silicon halides or aminosilanes. An example of a silicon hydride is silane (SiH_4), which has been used to grow SiN_x films at temperatures between 250 and 400 °C.[15] However, long cycle times ($>$ 1 minute) makes this process less attractive for commercial use. An example of a silylamine precursor is trisilylamine ($N(SiH_3)_3$), which was used in combination with a H_2-N_2 plasma at low temperatures ($<$ 400 °C).[2] Relatively low wet etch-rates of 1 nm/min demonstrated the relatively good film quality.[2] Good conformality was reported, with side/top ratios of $\sim$ 80%. Conformality, however, was only tested in trenches with a relatively low aspect ratio (AR = 1:2).

Alternatives are silicon halides, like SiH_2Cl_2 [13,16] and Si_2Cl_6 [8], which all involved a NH_3 plasma. While Ovanesyan *et al.* [8] reported good conformality at low stage temperatures ($<$ 400 °C), also significant hydrogen content ($\sim$ 23%) and a relatively low film density of 2.35 g/cm^3 was reported. Halide containing precursors are, however, not preferred since they can cause the incorporation of chlorines in SiN_x films, which can lead to detrimental effects.[17]

Other plasma-assisted ALD processes make use of aminosilane precursors. The past years, plasma-assisted ALD of SiN_x has been investigated extensively by multiple members of the PMP group. In

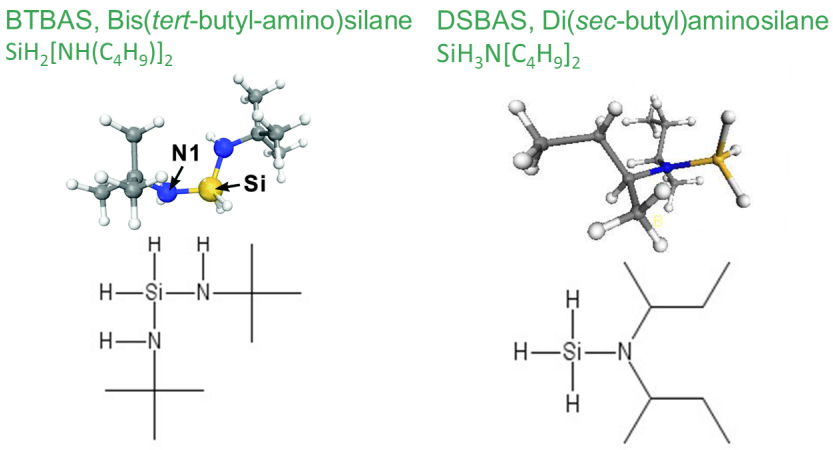

Figure 1.3: Schematic representation of both the DSBAS and the BTBAS precursor. The DSBAS precursor consists of 1 large ligand, whereas the BTBAS precursor consists of 2 less bulky ligands.

recent work conducted in the PMP group a plasma-assisted ALD process using a Bis(*Tert*-Butyl-Amino)Silane (BTBAS, $SiH_2[NH(C_4H_9)]_2$) precursor (depicted in Figure 1.3) has been developed and studied in detail.[14,18–21] SiN_x films were deposited at low substrate temperatures (< 400 °C) using BTBAS in combination with a nitrogen plasma. Decent quality SiN_x films were deposited using the BTBAS precursor, which is embodied by films with reasonable contamination contents ([C]<10% and [O]<5%). Moreover, the H-content was relatively low (<11%) and low wet-etch rates were obtained ($\sim$ 0.2 nm/min at 400 °C).[14] A disadvantage of aminosilane precursors in general occurs from the presence of carbon and hydrogen in the precursor ligands. The presence of carbon and hydrogen in the ligands of BTBAS can cause the carbon and hydrogen to be incorporated in the SiN_x films. Knoops *et al.*[21] has shown that redeposition of precursor fragments of BTBAS could lead to a reduction in SiN_x film quality. This has motivated a study into the deposition of SiN_x films using a similar precursor, Di(*Sec*-Butyl)AminoSilane (DSBAS, $SiH_3N(C_4H_9)_2$) (depicted in Figure 1.3). It can be observed that DSBAS contains one ligand, whereas BTBAS contains 2 ligands. It is hypothesised that the use of DSBAS leads to a decrease in redeposition of ligand fragments and subsequent higher quality SiN_x films, compared to films deposited by BTBAS.

1.3 Goals of the project

The five goals of this project will be discussed separately in this section.

Process Development

In this work, we have developed an ALD process of SiN_x from novel precursor DSBAS precursor and N_2 plasma. The main goal of this work comprised *the establishment and development of the silicon nitride plasma-assisted ALD process with DSBAS*. In order to do this, saturation experiments have been conducted to confirm the self-limiting behaviour, typical for ALD film growth. These experiments have led to standard process conditions, after which the SiN_x films were characterised. The material properties will be compared to results obtained with a similar aminosilane precursor; BTBAS. These comparisons help in the understanding of the SiN_x film growth by DSBAS, considering the known material properties and insights into the growth mechanism of SiN_x films grown with BTBAS.

Conformality

The second goal comprises the investigation of the conformality of SiN_x films, since important applications of silicon nitride in semiconductor industry, such as a sidewall gate spacer, require the deposition of highly conformal SiN_x films in trenches. Typically in the literature no studies are reported in which SiN_x are deposited in high-aspect-ratio structures (HARS), showing both high conformality and high quality. This motivated a study into both the quality and conformality of SiN_x films. We will focus on identifying and understanding the parameters that govern both the quality and conformality in HARS.

Reaction Mechanism

The third goal comprises the reaction mechanisms of both the DSBAS and BTBAS precursors. As already mentioned briefly before, extensive research has been conducted into the film growth of SiN_x films with BTBAS by members of the PMP group. The identification and understanding of the parameters that govern film growth of BTBAS, and aminosilane precursors in general remained however, complex and incomplete. Furthermore, it has been briefly discussed how an improvement in film quality can be expected as a result of a reduced redeposition effect for DSBAS, compared to BTBAS. This motivated a study into the reaction mechanisms of both BTBAS and DSBAS.

X-ray Photoelectron Spectroscopy investigation

The fourth goal comprised an investigation into potential errors and uncertainties in X-ray Photoelectron Spectroscopy (XPS) of SiN_x thin films. It will be argued how XPS could serve as an alternative for RBS in determining the absolute film composition. Furthermore, these investigations are meant to raise awareness of the limitations in the XPS analysis of SiN_x thin films. The study will lead to a set of recommendations and limitations.

FinFET literature study

Finally, in this literature study the road from traditional MOSFETs towards state-of-the-art FinFETs will be described. FET fundamentals will be briefly explained, before it will be discussed how SiN_x films can be applied as a side-wall gate spacer in FETs. This will facilitate a discussion about the opportunities for applying SiN_x films in future-generation FETs.

1.4 Thesis outline

This thesis is built up slightly different than regular theses. The main part of the results is presented in two chapters about process development and conformality. These two chapters are organised and written in paper style to make the chapters suited for publication. These chapters will contain separate and specific introduction, experimental setup, results and conclusion sections. Furthermore, throughout this thesis, DSBAS results or mechanisms will be often compared to BTBAS results or mechanisms, in order to facilitate in-depth discussions. The structure of other chapters in this thesis remains similar compared with ordinary theses. The build-up and contents of the chapters are briefly described hereunder.

Chapter 2: from MOSFET to FinFET and beyond
: This chapter will give background information and an overview of the development of Field Effect Transistors (FETs) over the years. It will be shown how SiN_x films can have an important role in current and future FinFETs.

Chapter 3: Experimental Setup and Diagnostics
: This chapter will cover the basics of the experimental setup and the diagnostics used in this work. In this chapter, there is a special focus on X-ray Photoelectron Spectroscopy (XPS), which is an important tool for characterising material properties of thin films in general. However, performing an XPS measurement on SiN_x films is complex and no standard procedure has been developed for such experiments yet, in our group. Therefore, via an in-depth study, potential errors and uncertainties in XPS of SiN_x thin films have been investigated, identified and benchmarked.

Chapter 4: Process Development
: In this paper-style chapter, the development of the plasma-assisted ALD process using a DSBAS precursor and nitrogen plasma will be described.

Chapter 5: Conformality
: In this paper-style chapter, a systematic study into the conformality and quality of SiN_x films deposited in high-aspect-ratio trenches is described and discussed.

Chapter 6: Aspects Regarding the Reaction Mechanism
: This chapter will cover the aspects regarding the reaction mechanisms of BTBAS and DSBAS. Previously obtained results and insights regarding the BTBAS process will be supplemented by new insights and results regarding the DSBAS process.

The work will be concluded in Chapter 7: Conclusion and Outlook.

Chapter 2

From MOSFET to FinFET and beyond

Dialling the emergency number with your mobile phone directly after an accident, processing a thesis on a Mac Book or driving a car with features like GPS: it is easy to take all these habits for granted. While our daily lives revolve around technological applications making use of transistors, the majority of society remains unaware of the significance of such a tiny device and the rapid developments in transistor technology that were necessary to reach to this point. Over the past 50 years the size of these building blocks for electronic devices has halved roughly every two years, still following Moore's law.[22] Multimillion dollar industries have already been created because of the transistor. Because of these big interests and heavy competition in semiconductor industry people are able to afford amazing devices which society currently already regards as ordinary. A major part of all this progress, both technological and scientific, would not have been possible without the transistor.

Innovation in semiconductor industry has become a race, one in which every nanometre matters. Literally small but simultaneously highly significant improvements can have big impact on total transistor design, but also on subsequent application design. At the time of this write-up, the 14nm node is considered as state of the art, where the term node historically refers to the transistor channel length but now serves more as a marketing term. Nevertheless, with transistor components scaling down to these dimensions, it will become increasingly complex to improve performance parameters.

In order to understand the challenges in transistor technology, the basic functions of a transistor need to be properly understood. Therefore, in this chapter the most common and widely used form of transistor will be discussed; the Field-Effect Transistor (FET). FET fundamentals will be briefly discussed, before discussing state of the art FinFETs and their production processes. Schematic images of a FinFET are shown in Figure 2.1. In this overview there will be a special focus on the role and opportunities of SiN_x in FinFETs, with which this chapter will also be specifically

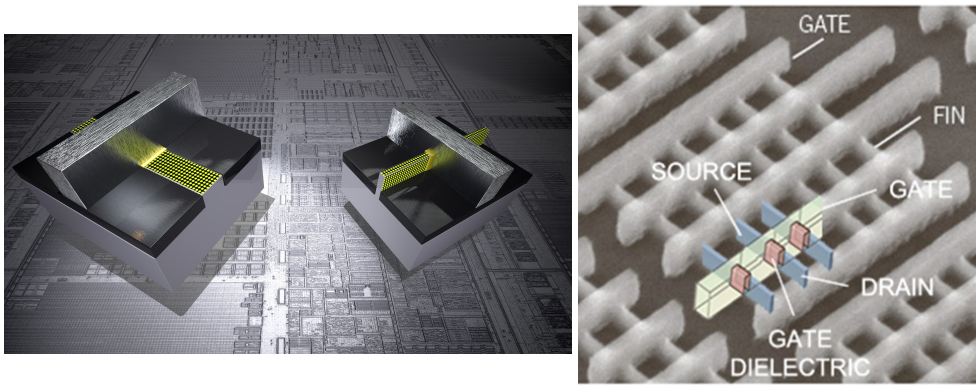

Figure 2.1: Schematic images of FinFETs. The left image shows a comparison of a traditional MOSFET with state-of-the-art FinFETS (obtained from Intel). The right image shows a network of FinFETs showing gate arrays perpendicularly to the array of fins connecting multiple FinFETs.[23]

concluded.

2.1 Field Effect Transistor fundamentals

The most important and basic function of a transistor is fairly simple: it is a switch. One of the most known and widely implemented transistors is called a metal-oxide-semiconductor Field-Effect Transistor, or MOSFET in short. The main components are the metal gate electrode, the dielectric (oxide) insulator and the semiconductor body. The gate electrode serves as the control input, where the application of a specific voltage (known as the gate voltage) allows a current to flow through the semiconductor from source to drain. This gate voltage allows a conducting pathway or channel to be formed in the semiconductor body, through which the current will flow. The dielectric insulator serves as a conduction barrier, located in between the gate and semiconductor body.

The total stack of metal gate conductor, gate dielectric and conductive channel through the semiconductor body resembles a traditional capacitor. Just as in a traditional capacitor, applying a voltage on one of the conductors will attract an equal number of opposite carriers to each side of the dielectric. When a gate voltage is applied, the mobile charge carriers concentrated near the interface of the dielectric and the semiconductor body give rise to a channel through which charge carriers can flow from source to drain, which is schematically represented in Figure 2.2. Controlling the gate voltage enables control of the amount of charge carriers in the channel and consequently, controls the effective thickness of the channel and resistance between drain and source. But even with zero gate voltage applied, a current can flow from source to drain. A voltage difference between source and drain can give rise to an internal electrical field, which will cause a current from source to drain. Total current, I_d, flowing from source to drain is therefore controlled by both gate voltage and the voltage difference between source and gate.

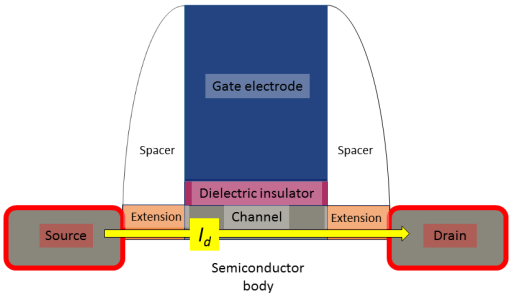

Figure 2.2: Schematic representation showing a basic MOSFET consisting of a metal gate (blue), an dielectric insulator (pink) and a semiconductor body (grey drain, source, channel and bulk substrate). In ohmic mode, explained in section 2.1.1, a channel is formed allowing carriers to flow from source to drain.

2.1.1 Operation fundamentals

Traditional MOSFETs consist of a planar channel connecting source and drain, where the current throughput is controlled by the gate voltage. By applying a specific voltage on the gate electrode, the current through the channel is controlled. If the gate voltage surpasses a certain threshold, V_{th}, a current will start to flow from source to drain. The magnitude of this current is dependent on the voltage difference between the gate and source, V_{gs}, or drain and source, V_{ds}. Three different operating regimes can be identified:

1) $V_{gs} < V_{th}$
2) $V_{gs} > V_{th}$ and $V_{ds} < (V_{gs} - V_{th})$
3) $V_{gs} > V_{th}$ and $V_{ds} \geq (V_{gs} - V_{th})$

In operation regime **1)** there is no conduction between source and drain, the switch is turned off. In operation regime **2)** a channel between source and drain is created, which effectively switches on the FET. The channel thickness and subsequent current through the channel is now controlled by both V_{gs} and V_{ds}. This regime is also referred to as the ohmic regime because the MOSFET acts as a resistor. With increasing V_{ds} the channel becomes more tapered, until the channel thickness is reduced to zero near the end of the channel close to either drain or source (depending on the charge of the mobility carriers in the channel). Operation regime **3)** occurs when V_{ds} is increased above this threshold voltage, which is called the pinch-off voltage, V_{po}. Above V_{po}, V_{ds} does not control the magnitude of the current through the channel any more: I_d is now saturated for V_{ds}. V_{gs} now controls the width of the channel and resistance, making I_d only dependent on V_{gs}. The switch is now turned on and the FET is in active mode.[24]

In order for the switch to work effectively, these operation regimes need to be very clear and distinguished. Very good voltage control is essential in order to obtain a stable and clear I_d current when the switch is turned on, which is key for good operation of a FET. Also when the switch is turned off, it is important that leakage currents are minimised. Since FET dimensions and power consumption keep decreasing, all the loss mechanisms occurring in a FET are becoming more significant. Therefore, these loss mechanisms need to be minimised, which will be explained further in this chapter.

2.1.2 Field Effect Transistor components

As already stated in the previous section 2.1.1, the main components of a MOSFET are the semiconductor body, dielectric insulator and the metal gate electrode. In an actual FET there are more components that affect FET performance. In this section the gate spacer, the high-κ metal gate and the doped source and drain regions will be highlighted. The specific components are depicted in Figure 2.4, in which the components are identified in both a real FinFET as more clear in a Lego^{TM}model of a FinFET.

One of these components is the spacer, which is often composed of SiN_x. The main function of this spacer is to protect the gate stack from e.g. air diffusion and oxidation from subsequent processing steps. As will be shown in the next section 2.2.1, the production of a FinFET involves multiple etching steps, high temperature anneal steps and steps that involve exposures of plasmas. Such exposures of sensitive gate materials like the high-κ and the metal gate stack (HKMG) would result in damage to these structures, since materials like HfO_2 and TiN are very sensitive towards oxygen ingress.[9] Therefore, very robust spacers are needed to encapsulate the gate stack in order to prevent damage from these processing steps. Materials showing very low etch rates are necessary in order to be suited as a gate spacer. As will be discussed in following section, the spacer is also important in defining the source and drain regions in the FET and for introducing strain, which can increase carrier mobility.

The high-κ metal gate (HKMG) stack is typically composed of 2 separate layers: a high-κ (HK) layer, such as HfO_x and a metal gate (MG) layer, such as TiN. High-κ materials typically refer to a class of metal oxide insulators with a relative dielectric constant > 9.[25] According to Robertson and Wallace[26] a key requirement for high-κ materials is that the κ values should be over 12, preferentially even between 25-35. The use of such high-κ materials enables both further downscaling of transistor size and the use of thicker gate dielectrics, while keeping the capacitance constant or at even higher values.[9] This can be seen by the following relation of a parallel plate capacitor, with which the gate dielectric can be modelled: $C_{ox} = \kappa\varepsilon_0 A/t_{ox}$.[7] In this relation, κ refers to the dielectric constant of a specific dielectric material, ε_0 refers to the vacuum permittivity, A to the surface of the considered material and t the material thickness. When the switch is in active mode, C_{ox} scales with saturated I_d (see Appendix F.1 for this relation). In active mode, it is, therefore, important to not let C_{ox} decrease, since this will increase saturated I_d and consequently total FET power usage. In addition to this, the use of high-κ materials allows for an increase in thickness of the gate dielectric, while keeping the gate capacitance constant. This increased dielectric thickness leads to a decrease in electron tunnelling, consequently leakage current and, therefore, decrease in

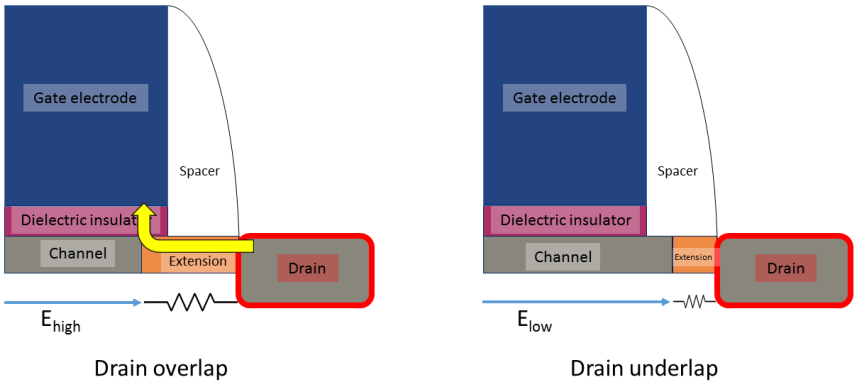

Figure 2.3: A schematic representation of a part of a traditional MOSFET shows how both extension overlap and underlap affect the performance of the transistor. A drain overlap leads to increased tunnelling, whereas a drain underlap leads to both a decreased electric field and an increased resistance.

total power consumption of the FET. How this affects transistor design will be described further in the next section 2.2, where design challenges will be discussed.

Within a network of FETs, multiple regions are specifically doped in order to prevent unwanted parasitic capacitances and resistances. Focusing on all these dopant regions goes beyond the scope of this thesis. The discussion will be limited to the doped source and drain regions within one FET switch since the gate spacer plays an important role in this source-drain doping. When the switch is turned on, a current will flow from drain to source through a channel in the semiconductor body. But as can be seen in Figure 2.2, carriers also have to flow through extension regions located underneath the side-wall spacer. These extension regions act as a transition region from the channel to the highly doped source and drain regions. The extension regions are mildly doped and prevent drain to body and source to body depletion leading to lower transistor performance[27]. When the extension region overlaps with the gate region, leakage current flows via tunnelling from drain or source to gate, which is depicted in Figure 2.3. When the extension region is too short, this leakage current decreases because the side-wall spacer prevents tunnelling to the gate. A shorter extension region consequently leads to a reduced electric field[28]. Controlling the length of the extension region precisely is therefore, important in controlling FinFET performance. Later in section 2.2, it will be shown how the SiN_x gate spacer can contribute to a precise definition of the extension regions in addition to a precisely definition of source and drain regions.

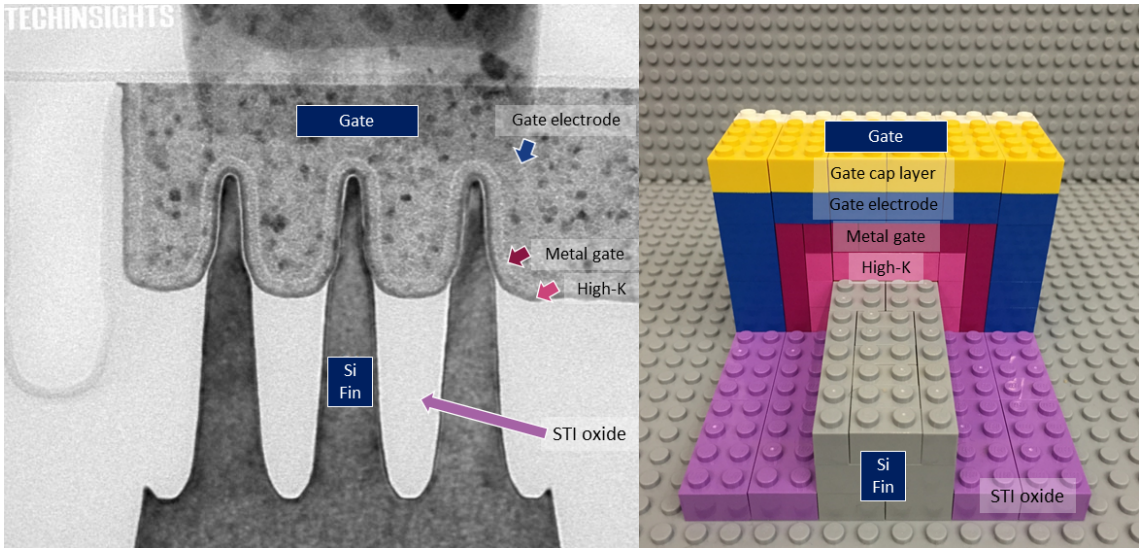

Figure 2.4: The left image shows Samsung's Exynos 7420 transistor, used in for example Samsung's Galaxy S6, which is obtained from TechInsights.[29] The right image depicts a Lego^{TM} model showing individual FinFET components. In both images, the gate and silicon fin are perpendicularly orientated facilitating one gate to control multiple fin channels. The gate electrode, metal gate, high-κ dielectric insulator and shallow trench isolation (STI) oxide are indicated in both images. A separate gate cap layer might be present in Samsung's FinFET, but cannot be clearly identified.

2.2 The road to FinFETs

The traditional MOSFET as described in section 2.1 recently reached complex scaling limits. This necessitated a shift towards new FET architectures, among which the FinFET is being readily adopted as the mainstream design in transistor technology. In this section a brief historic overview will be given to show how the focus shifted from lithographic challenges to architectural constraints.

For decades, downscaling of MOSFET size mainly involved reducing the wavelength in order to pattern smaller features via etching. Transistor performance, operating voltage and transistor current scaled down accordingly with transistor size. This general relation has been proposed by Dennard *et al.*[30] in 1974. This scaling law roughly states that as a function of decreasing transistor sizes, the power density remains constant. Dennard's scaling law has been a roadmap for semiconductor industry for years until it hit a limit roughly ten years ago.[31] Transistor dimensions had reduced to a point at which leakage current became so large that they severely affected transistor performance.

New challenges arised when lithographic techniques reached fundamental limits involving wavelength and numeric aperture. Since resolution in lithography technology is proportional to wavelength of the light source, attempts have been made to decrease source wavelength for patterning. For roughly the past ten years, efforts have been made to go from the currently highest resolution

193 nm lithography to extreme ultraviolet lithography (EUV) at 13.5 nm.[32] However, the adoption of EUV as a mainstream industrial standard is not expected before 2023, demonstrating the complexity and challenges in lithography-enabled-scaling.[33] Currently these lithographic limits can be bypassed by innovative and relatively complex masking techniques. An example with which these lithographic limits can be overcome uses spacer defined patterning. With this technique, the fin width can be narrower than fins which are defined via current lithography, but very good quality spacers are required. This will be discussed in the next section 2.2.1 about the production of FinFETs. Spacer defined patterning has been successfully applied already in 2003.[34] However, a drawback for such spacer defined double and triple patterning techniques lie in them being relatively expensive and imposing severe limitations on layout design.[35,36]

A way to reduce costs involve increasing the wafer size from current 300 mm to 450 mm, increasing production efficiency by reducing per transistor costs. However, the economics of this 450 nm technique have been linked to the EUV technique, resulting in similar delays before it is expected to be adopted commercially.[33]

At a certain point the focus shifted to materialistic enabled scaling techniques, which might have been a result of lithography based scaling limitations. Challenges in material dependent scaling involve increasing channel mobility, improving short channel control and decreasing parasitic resistance and capacitance[37]. A means through which this decrease in parasitic resistance can be reached involves the introduction of high-κ materials, which was already briefly mentioned in section 2.1.2. The use of high-κ materials results in a higher equivalent oxide thickness (EOT), which facilitates a decrease in electron tunnelling and subsequent increase in FET performance. EOT is defined as $EOT = t_{high_\kappa}(\kappa_{SiO_2}/\kappa_{high_\kappa})$ and indicates how thick a traditionally used silicon oxide dielectric insulator film would be in in order to maintain a specific capacitance. As transistor size reduced, a critical limit for standard SiO_2 dielectric insulators was reached. Traditional silicon oxide dielectric insulators had reached thicknesses close to 1.2 nm, at which significant tunnelling had started to occur[26]. In order to maintain a specific C_{ox}, the use of a high-κ material allows for a much thicker t_{ox}, which reduces electron tunnelling and consequently decreases leakage current. The introduction of high-κ materials resulted in additional prerequisites in the FET production process. As already mentioned in section 2.1 high-κ materials can be easily degraded during further processing steps[9]. In order to protect these stacks from such subsequent plasma, etch or high temperature anneal steps, a protective and robust spacer needs to be deposited.

The exploitation of lithographic and materials based techniques gave space for a new range of improvements. Recently a new generation of FETs has been successfully employed commercially in the newest designs, the so called FinFETs. In these devices the semiconductor body has been raised from the planar to a three-dimensional fin, depicted in Figure 2.1 **(a)**. Instead of one interface in traditional MOSFETs three interfaces between semiconductor and gate have been created by depositing the HKMG stack and gate materials around these fins, which is depicted in Figure 2.4.

Future designs will probably combine the new EUV lithography techniques on larger 450 nm wafers with developing FET architectures. Kuhn[37] proposed an *ultimate* CMOS device consisting of a nanowire channel with a gate all around, depicted in Figure 2.5. But what is currently

Table 2.1: A brief and simplistic overview showing current challenges in lithography, materials based techniques and architecture.

	Area	Future challenges
1)	Lithography	Extreme UV
		Advanced patterning
2)	Material	High-κ
		Stress via SiN_x
3)	Architecture	Optimizing FinFET
		From Quantum Well FinFET to gate all around?

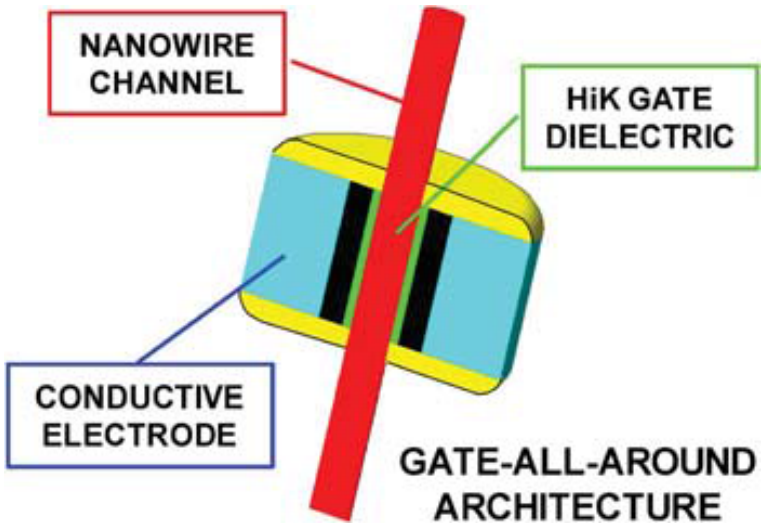

Figure 2.5: An example of Gate-All-Around Architecture, as proposed by Kuhn [37]

perceived to be an *ultimate* CMOS device now could end up being completely different in the future. New issues at smaller transistor size will inevitably come up. Interface effects will become increasingly important compared to bulk effects, in addition to other effects that will become more significant at smaller dimensions.

So far the focus has been on both past and future challenges regarding lithography, specific materials and architecture. However, in order to design an effective manufacturing process all these challenges need to be overcome collectively. Apart from large scale production and economic considerations, production of simply one transistor is rather complex by itself. In the next section, this will be showed by focusing on the various steps that are necessary for manufacturing a FinFET.

2.2.1 FinFET manufacturing

In this section multiple steps involved in the manufacturing of a FinFET will be discussed. Since all semiconductor companies have their own detailed methods of manufacturing a FinFET, the focus here will be on giving a more general overview of all manufacturing steps. One of the most significant differences in the manufacturing of a FinFET revolves around the choice between a gate-first or a gate-last strategy. Traditionally MOSFETs were produced using a gate-first strategy. For the manufacturing of FinFETs, IBM initially stuck with gate-first technology whereas for example Intel initially opted for the gate-last strategy. In order to visualise how this choice affects the manufacturing strategy, the fundamentally different manufacturing steps have been reconstructed in our Lego^{TM}-lab, depicted in Figure 2.7. First the similar manufacturing steps preceding these gate deposition steps will be briefly discussed.

The process starts with an anisotropic etch step, in order to form an array of trenches on the substrate. However, as mentioned in section 2.2, current lithography capabilities alone lack the necessary resolution for patterning the required fin pitch. While current fin pitches have reached values around 80 nm, the optical resolution is relatively low with only 193 nm. Immersion lithography is a technique with which smaller dimensions can be reached, supposedly even $\sim$ 25 nm. Briefly, with immersion lithography, a liquid is put between lens and wafer, increasing the resolution with a factor which scales with the refractive index of the material. Another way to work around the optical limits and to reach higher fin pitches is via double, triple or even quadruple patterning as already mentioned in 2.1. With this technique a sacrificial mandrel is deposited. For example via ALD a spacer layer is deposited around this mandrel. After an etch step the mandrel is removed leaving only the standing spacer layers. This spacer layer functions as a hard mask in a subsequent etch step or can even serve as another mandrel to reach even smaller pitches, as can be seen in Figure 2.6.

After the fins have been patterned, a local insulation layer is deposited. This insulation layer, e.g. SiO_2, serves as a barrier between the fins and channels. This layer, often called a shallow trench isolation (STI) layer, can be recognised in figure 2.7 as the purple 'STI oxide' blocks. At this point either a gate-first or gate-last FinFET manufacturing strategy can be employed of which the separate steps are shown and described in Figure 2.7. The biggest difference follows from the anneal

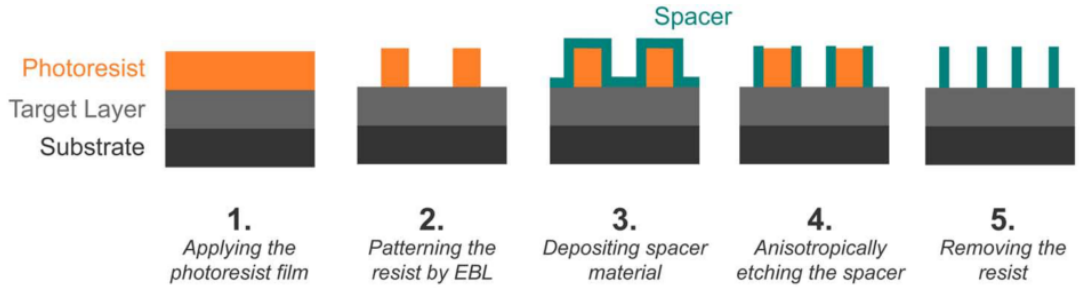

Figure 2.6: A schematic representation of spacer defined pattering, obtained from Roelofs[38] First a sacrificial mandrel layer is deposited and patterned via conventional lithography. Then a spacer layer is deposited around the mandrel. After an anisotropic etch the mandrel is removed leaving the standing spacer layer, which can serve as a hard mask for patterning the fins.

step onwards that has to be performed after the implantation of source and drain, basically repairing the damage done during the implantation.[40] This high temperature (typically around 1000 °C[26]) anneal can damage the gate stack, so ideally this annealing step is done before depositing the gate stack as is the case in gate-last. Recently semiconductor manufacturers like IBM and GlobalFoundries decided to shift to the gate-last manufacturing strategy, possibly resulting from this severe disadvantage of the gate-first strategy. Nevertheless, gate-last in principle, remains disadvantageous over gate-first. According to Moyer[40] the gate-last process gives restrictive design rules leading to an overall density penalty of 10 to 20 % compared to gate-first. In future transistor nodes a shift back to gate-first may occur when gate stack quality can be properly preserved.

A problem arises when SiN_x spacers are not only deposited around the gate, but also around the fins. There are multiple ways to selectively remove these layers, but these methods involve some non-trivial production steps. One option to selectively remove these SiN_x spacers around the fin is via a dry etch while using a hardmask on top of the gate. This hardmask needs to be taller/'more resistant' than the side-wall spacer on the fin, as is showed in Figure 2.8. In other words, the total spacer on the side-wall needs to be removed before the hardmask is completely removed ensuring the gate itself is always well protected. In case the gate is not completely covered with high quality SiN_x, defects can result in short circuits between drain and gate or source and gate can occur, resulting in reduced FET performance. This is more likely to occur, since it is common to widen source and drain regions by widening the FET in order to reduce fin resistance, making short circuits even more likely.[28] Conformal and uniform deposition of SiN_x with good thickness control is therefore, essential in this step. Other techniques involve the use of filling material that prevents any SiN_x side-wall formation near the fin.[41] Another strategy has been employed by Basker *et al.*[42]. Here fin side-wall spacer was selectively damaged by an angled ion impurity implant by aiming the ions at the fin side-wall. In this case, the ions are directed parallel to the direction of the gate, resulting in selective etching of the fin spacer and missing the perpendicularly placed gate spacer material.[42] As a result of the selectively caused damage, the spacer around the fin can be removed using an etch step with high selectivity in comparison to the gate spacer. In order to successfully employ this strategy, good control over the ion angle and ion energy is key.

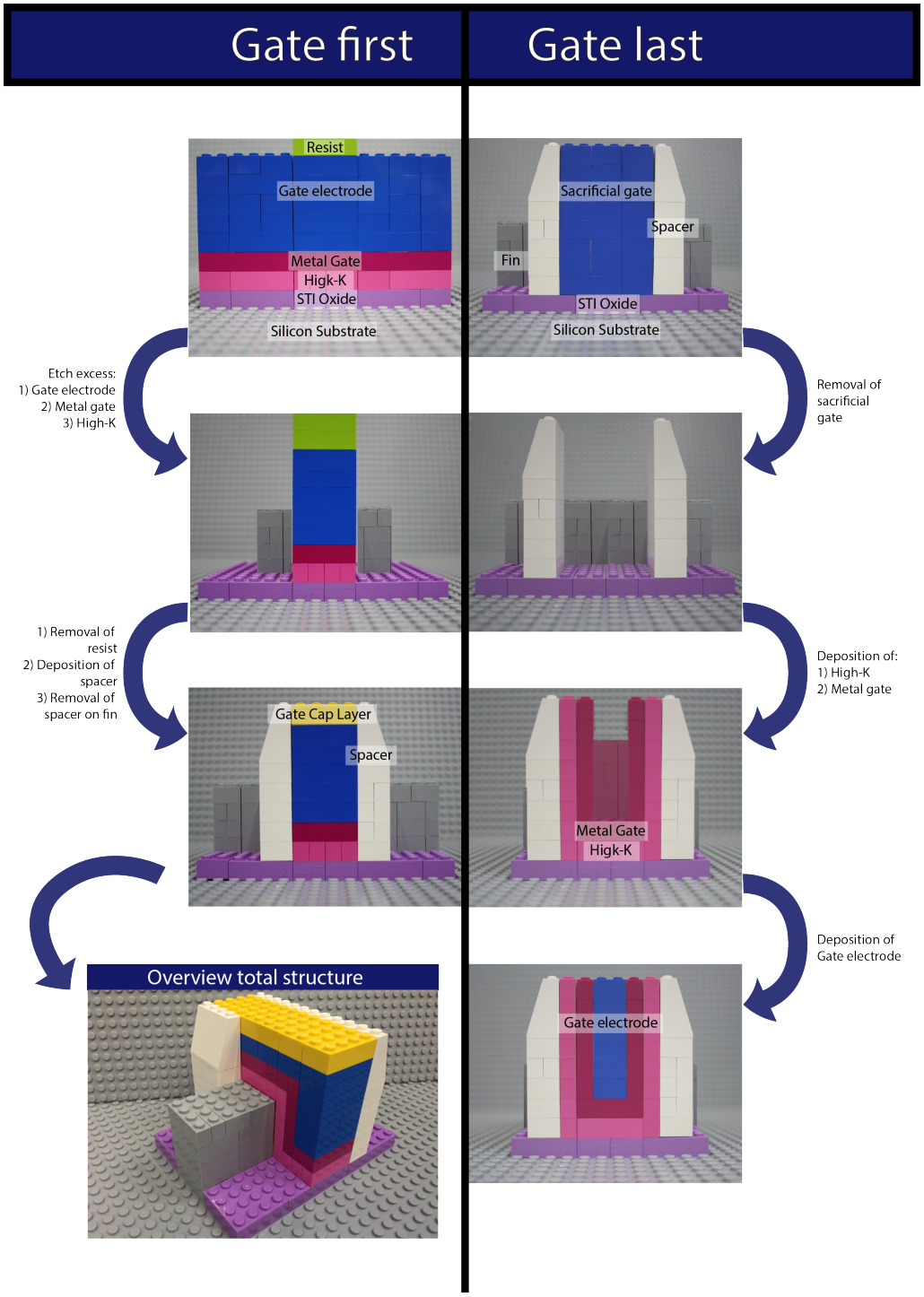

Figure 2.7: In this overview, based on Nojiri [32] and a patent describing spacer formation from Cai *et al.* [39], both gate-first and gate-last manufactering processes are visualised. In the gate-first process (left) all layers making up the gate stack are deposited first. By applying a resist an etch step removes excess gate material. Not visualised are subsequent steps involving doping source and drain regions. Finally side-wall gate spacer is deposited. In the gate-last process (right) first the side-wall gate spacer is deposited around a sacrificial gate. Again, all steps involving doping source and drain regions are not shown. After removing the sacrificial gate the gate stack materials are deposited.

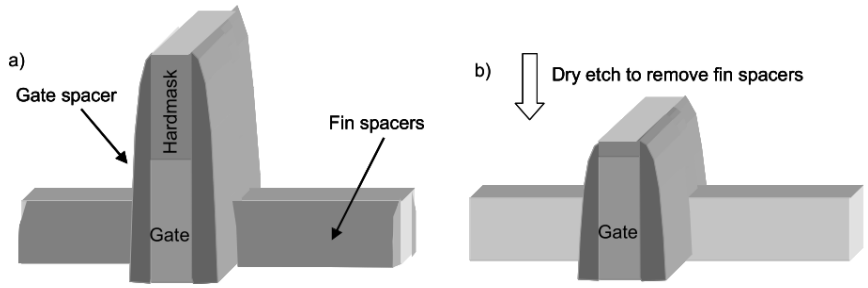

Figure 2.8: A schematic representation of a gate first process in which in **(a)** a tall hardmask can be seen on top of the gate. In **(b)**, it is shown how in a subsequent etch step the fin side-walls are removed together with a part of the hardmask. The image is obtained from Colinge [28]

In addition to that high quality SiN_x gate spacers need to be deposited so the spacer remains unaffected after such an etch.

2.3 Opportunities for silicon nitride?

So far we have focused primarily on SiN_x as a gate spacer. SiN_x, however, can also be important in several other configurations in FinFETs. In this section SiN_x gate spacers will be discussed, after which other opportunities for applying SiN_x in FinFETs will be addressed and briefly discussed.

2.3.1 Gate spacers

Kuhn [37] identified the challenge for finding a suitable spacer and contact etch stop material as key in reducing parasitic capacitance around the transistor. Both these requirements can be simultaneously achieved by using a gate spacer which is both low-κ and very robust.[37] Silicon nitride can be considered a decent candidate, since it is very robust and has a reasonable low κ-value. Typically, stoichiometric silicon nitride (Si_3N_4) has a κ-value of 7.5.[43] In this work, SiN_x films of very high quality were deposited showing no significant etch after a one minute dip in diluted HF. Since these depositions were performed at low temperatures ($<$500 °C), SiN_x can be considered a suitable candidate for a robust spacer layer in FinFETs. However, other materials with lower κ-values could also be considered as spacer in FinFETs.[43] Ko *et al.* [43] recently developed such a gate spacer consisting of SIBCN which they deposited at 550 °C via a thermal CVD process. They were able to produce SIBCN with a κ-value of 5.2 illustrating the potential of such alternative materials. Altogether, Ko *et al.* [43] showed improvements in total effectiveness, but also partly because a 6% increase in electron mobility specifically by building in stress in the FinFET channel.

2.3.2 Strain engineering

Another opportunity for successfully applying SiN_x in FinFETs and future FETs is by using it to build in stress, as already mentioned above. It has been shown that FET performance can be improved by increasing the mobility, μ, of the carriers through the semiconductor channel (see Appendix F.2). A method with which this can be achieved is by strain engineering. It has been shown that carrier mobility in a FET channel increases significantly when the FET channel is either stretched or compressed, depending on the charge of the mobile carriers in the channel. While a tensile stress is beneficial for a NFET (a MOSFET with electrons acting as mobile carriers) in longitudinal direction (from source to drain), compressive stress is necessary for an increase in PFET (a MOSFET with holes acting as mobile carriers).[36] A way to increase the mobility of both NFET and PFET is by applying a dual stress capping liner. With this technique initially a tensile stress liner is deposited over the whole structure. Hereafter, the tensile layer is selectively etched away from PFET sites, where the mobility would have been degraded otherwise. This step is then repeated but with a compressive stress liner, which is selectively etched away from the NFET sites. Yang *et al.*[4] obtained an increase in NFET current of 11% and an increase of PFET current of 20% using a SiN_x stress liner.

Another method with which carrier mobility can be improved is by depositing a SiN_x capping layer on top of the gate. The tension or compression of this cap layer will lead to subsequent strain in the channel, which increases carrier mobility. By combining this with the aforementioned dual stress liner technique, both NFET and PFET mobility can be increased simultaneously. Shin *et al.*[5] modeled and predicted that by using SiN_x as a capping layer a $>$100% increase of electron carrier mobility (in NFET) and $<$25% increase in hole mobility (in PFET) can be obtained. showing the promise of this application of SiN_x. Since typically NFET and PFET are integrated in circuits and manufactured accordingly, being able to simultaneously increase both mobilities is very useful.

Sacrificial SiN_x layer can also be used to built in and retain stress. This retention is achieved by depositing the SiN_x around the gate, followed by a high temperature anneal to transfer the tensile stress into the channel. After the stress transfer the SiN_x layer is removed again. With this technique only NMOS mobility can be increased. An improvement in NMOS current of 15% has been achieved.[3]

Although mobility increases are very specific to both the technique used to apply the stress as the materials itself, it shows this can significantly improve FET performance. An advantage is that strain methods are additive, so multiple of the aforementioned techniques can be exploited to improve carrier mobilities even more.[36]

2.3.3 Other applications

As already mentioned in section 2.1.2, the gate spacer can contribute in a precise source and drain definition. When drain underlap or overlap occurs (see Figure 2.3), FET performance is reduced significantly. In addition to this, the narrow width of the fins in current FETs results in a high

parasitic resistance in these extension regions. Therefore, the extension regions need to be as short as possible in order to reduce the parasitic resistance.[44] Since source and drain ion implantation occurs after deposition of the gate spacer, a high quality SiN_x gate spacer reduces the thickness of the gate spacer required to protect the gate stack, which also reduces the thickness of the extension region.

SiN_x has also been used for patterning fins very accurately in spacer defined patterning techniques.[6] The process flow, see Figure 2.6, has already been described in section 2.2.1. When FinFET dimensions decrease, accurate patterning of the fins is becoming increasingly important. As a result of this, good thickness control and conformality of these spacers is essential in patterning fins with uniform thicknesses.

2.3.4 Summary

Altogether, SiN_x can be applied in multiple different ways and with different functionalities. It is commonly used as a gate spacer to act as a barrier for the HKMG stack against water and oxygen ingress and subsequent etch processing steps. Silicon nitride gate cap layers or stress liners can be used for strain engineering. To prevent short-circuits and subsequent current losses from both source to gate and drain to gate, a high quality SiN_x deposition combined with high conformality, uniformity and good thickness control is vital. In addition, the high conformality also facilitates a better definition of source and drain, resulting in higher transistor currents. Being able to do these depositions at low temperature is advantageous, since high thermal budgets could induce unwanted diffusion of materials. Plasma assisted atomic layer deposition of SiN_x is therefore, promising since it possesses most of these characteristics simultaneously. However, as will be shown later in this work, obtaining high conformality is not trivial and leads to other challenges. These will be presented and discussed in Chapter 4 and Chapter 5.

Chapter 3

Experimental Setup and Diagnostics

In this chapter an overview of the experimental setup and diagnostics used in this work will be given. First, the reactor design and deposition conditions will be covered. This coverage will be rather general, since experimental design and deposition conditions of specific experiments will be explained in more detail in the following chapters. Secondly, the diagnostics used in this work will be described. These descriptions will be very general, with exceptions of Rutherford Back Scattering (RBS) and Elastic Recoil Detection (ERD), and X-ray Photoelectron Spectroscopy (XPS), which are important tools for characterising material properties of the thin films in this work. It will be shown how RBS and ERD can yield better measures for quantifying film growth, compared to the conventional GPC. Furthermore, via an in-depth study, potential errors and uncertainties in XPS of SiN_x thin films have been investigated, identified and benchmarked.

3.1 Experimental setup

3.1.1 ALD reactor design

All experiments have been carried out in a FlexAL®Atomic Layer Deposition (ALD) reactor developed by Oxford Instruments. The plasma is produced by a remote inductively-coupled (ICP) plasma source. The plasma RF source operates at a frequency of 13.56 MHz with a maximum input power of 600 W. The pressure during individual deposition steps can be accurately controlled by a butterfly valve, which is located between the reactor and the turbo pump, as is depicted in Figure 3.1. The plasma pressure was typically between 10 and 80 mTorr. Wafers with diameters in the range of 2 to 8 inch can be placed on a substrate table of which the temperature can be controlled between 25 and 500 °C. The reactor is equipped with a *in-situ* spectroscopic ellipsometer

(SE) with which we were able to monitor film growth and refractive index during the deposition. Other specifics of the reactor have been reported more elaborately by Heil *et al.* [45].

In the experiments described in Chapter 4 about process development, the depositions were performed on 8 inch planar wafers, which were positioned on top of the substrate table directly. In the experiments described in Chapter 5 about conformality, the depositions were performed on small coupons, which contained high-aspect-ratio structures (HARS). The lay-out of these structures is shown in Appendix C. Since these coupons did not fit on the loading-holder, a holder used for transporting the sample into the reactor, a carrier wafer was necessary. To that end, an 8 inch carrier wafer was placed on the loading holder, on top of which the coupons were placed and carried into the reactor. As a result of this, the coupons are located on top of the carrier wafer in the reactor. In turn this carrier wafer is located on top of the stage/substrate table, as is depicted schematically in Figure 3.1.

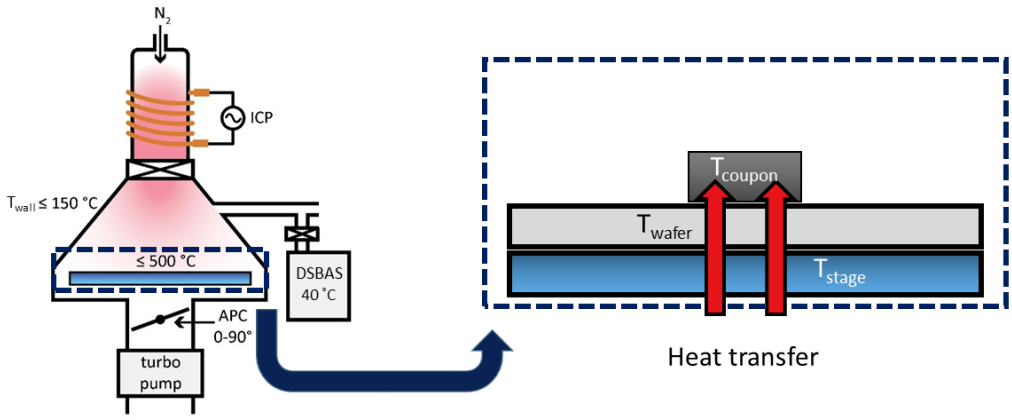

Figure 3.1: Schematic overview of the FlexAL®reactor by Oxford Instruments used for the deposition of SiN_x thin films. The setup allows for *in-situ* spectroscopic ellipsometry measurements. The enlarged schematic shows how limited heat transfer through point contacts can lead to reduced sample temperatures.

3.1.2 Sample temperature control

Ideally, the temperature of the wafer is equal to the temperature of the stage table, on top of which the sample is placed. However, due to poor thermal contact between the stage table and the wafer that is located on top, the actual sample temperature is significantly lower than the temperature of the stage table. The poor thermal contact between stage table and wafer is mainly a result of

Table 3.1: Relation between stage temperature, wafer temperature and coupon temperature, as defined in Figure 3.1. These temperatures have been estimated with *in-situ* spectroscopic ellipsometry. Note that the substrate table in the reactor was upgraded to a newer model. This seems to have resulted in a slightly increased heat conduction and subsequently sample temperature, after the update. The values of T_{wafer} were determined before the upgrade and concern the experiments described in Chapter 4. The values of T_{coupon} were estimated after the upgrade when a majority of the experiments described in Chapter 5 were conducted. However, since a few experiments in Chapter 5 were conducted before the update, T_{coupon} can be lower in those cases (very rough estimate: $\sim$ 50 °C) compared to the temperatures mentioned in this Table.

Stage temperature °C	Wafer temperature °C	Coupon Temperature °C
200	200 +/- 20	–
300	280 +/- 20	240 +/- 20
400	320 +/- 20	–
500	360 +/- 20	330 +/- 30

the typically low pressures in the reactor ($<$ 100 mTorr). This causes the heat transfer between stage table and sample to occur via point contacts, i.e. only a few points at which the wafer and stage table touch. As a result, heat transfer from stage to wafer is limited drastically. In order to determine the effect of the limited heat transport on the wafer temperature, the wafer temperature was measured during film depositions, of which the results are shown in Table 3.1. In the Table it is shown how the limited heat transport leads to a reduced wafer temperature T_{wafer}. In case of deposition on coupons (which were used in the conformality experiments), heat not only has to be transferred from stage to carrier wafer, but also from carrier wafer to coupon (see Figure 3.1). This results in an even lower coupon temperature, T_{coupon}. Note that these values denoted in Table 3.1 should be interpreted as an estimation of the actual sample temperature, due to case-to-case variations in thermal contact.

A few factors introduce fluctuations and uncertainties in the actual sample temperature. First of all, the experiments via which the wafer temperatures were determined have limited accuracy. The temperatures mentioned in Table 3.1 were determined via *in-situ* spectroscopic ellipsometry, with which the temperature of the wafer or coupon could be measured. The accuracy of this temperature measurement is, unfortunately, difficult to verify. On top of this, the heat transport depends heavily on the reactor pressure, which influences the thermal contact between stage table and wafer in the reactor. Braeken *et al.* [18] has investigated this previously and has shown that the an increase in plasma pressure from 20 to 100 mTorr can lead to an increase in wafer temperature of $\sim$ 30 °C. This influences comparisons between films deposited at different plasma pressures. Another factor that has to be considered, concerns an upgrade of the reactor stage table. The upgrade seems to have led to slightly better heat conduction and subsequent higher wafer temperatures. Unfortunately, some experiments were conducted before the upgrade, whereas some experiments were performed after the upgrade. This complication only concerns the experiments mentioned in Chapter 5 about conformality. In Chapter 5, it will be explicitly mentioned which samples were

conducted before and which after the upgrade. Altogether, it has to be noted that determination of the actual sample temperature is complex and only rough estimates of the sample temperature can be given.

3.1.3 Standard SiN_x ALD process

All steps in the standard SiN_x ALD process are schematically shown and explained in Table 3.2. This process has been developed by conducting a set of saturation experiments, which will be described later in Chapter 4. Unless mentioned otherwise, the deposition were carried out using the settings mentioned in Table 3.2. All steps involved in the ALD cycle are depicted in Figure 3.2. During all precursor steps a continuous 50 sccm flow of inert N_2 gas was introduced into the reactor through the plasma source to prevent the precursor from adsorbing on the surface near the ICP source in the reactor chamber.

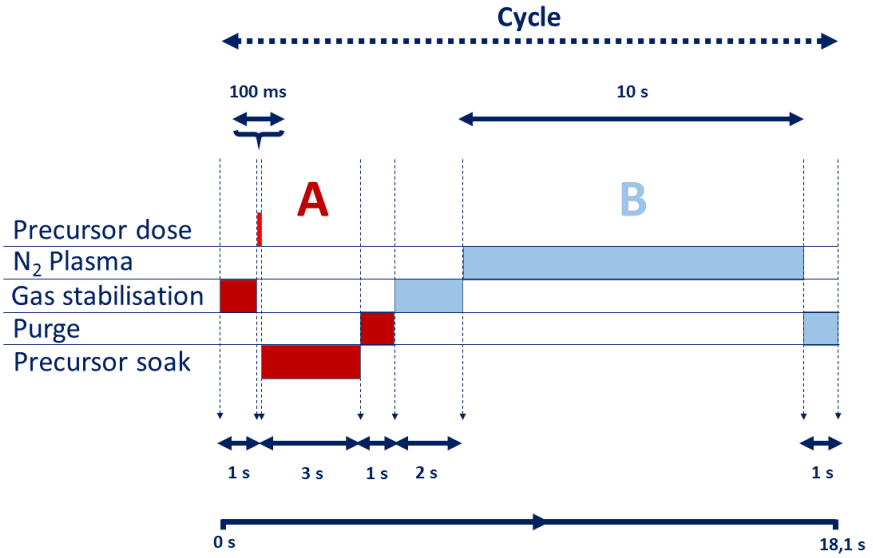

Figure 3.2: Schematic overview of all the steps in an ALD cycle. In step A), the precursor-steps during the first half-cycle are mentioned. In step B), the plasma-steps during the second half-cycle are mentioned. More specifics about process parameters can be found in Table 3.2

3.1.4 Diagnostics

Several diagnostics have been used to investigate and characterise the SiN_x films. Spectroscopic Ellipsometry (SE), Transmission Electron Microscopy (TEM), wet chemical etch-rate experiments, Rutherford Back Scattering (RBS), Elastic Recoil Detection (ERD) and X-ray Spectroscopic Spectroscopy (XPS) have been used in this work. SE, TEM and wet chemical etch-rate

Table 3.2: Overview of all the steps, in chronological order, in the standard SiN_x plasma-assisted ALD process we developed. After the wafer warm-up and initialisation steps, the ALD-cycle starts. The ALD-cycle can be repeated until the target thickness is reached. The final step consist of a pump down step.

ALD-steps chronologically	Typical duration (seconds)	Specifics
Wafer warm-up	840	The wafer is heated at an elevated reactor pressure of 900 mTorr
Initialisation	10	The reactor pressure is lowered back to deposition pressure
Start of ALD-cycle		
Gas stabilisation flow	1	Precursor delivery lines are purged with Argon to remove contaminants and ensure a stable flow
Precursor dose	0.1	Bubbler valve opens and precursor is vapour drawn into the reactor. Butterfly valve is closed
Soaking step	3	The butterfly valve is opened only slightly to allow precursor adsorption to saturate
Precursor purge	1	Reactor is purged completely to remove all reaction products. Butterfly valve is completely open.
Gas stabilisation flow	2	Plasma gas flows are started. This step is added to ensure gas flows and pressure has stabilised
Plasma	10	The plasma is ignited
Plasma purge	1	Reactor is purged completely to remove all reaction products and plasma species Butterfly valve is completely open.
End of ALD cycle		
Pump down	30	Reactor is pumped down

experiments will be described briefly. Both RBS and ERD, and XPS will be discussed in more detail, in specific sections 3.2 and 3.3 respectively.

Spectroscopic ellipsometry

Spectroscopic Ellipsometry (SE) is an optical technique in which the change of polarisation of light upon reflection on the surface of a sample is measured. Via SE measurements, film thickness and optical properties have been determined. *Ex-situ* measurements have been conducted using a J.A. Woollam Variable Angle SE with a VB-400 Control Module and an HS-190 monochromator (1.2 eV - 6.5 eV). *In-situ* measurements have been conducted using a J.A. Woollam SE M-2000F (1.2 eV - 5.0 eV) under an angle of 70 °. More specifics regarding SE for analysis of films deposited via ALD have been reported in detail by Langereis *et al.* [46].

For modelling of film thickness and refractive index a Cauchy model has been employed. This model has been applied for fitting data over a limited range (1.2 - 4.0 eV), since SiN_x is optically transparent in this region.[47] The Cauchy model describes the dispersion of the refractive index and can be used to determine film thickness.[46] These parameters are the parameters of interest regarding the SE experiments conducted in this work.

Furthermore, the SiN_x film uniformity has been studied by analysing SiN_x films deposited on 8 inch wafers. To this end, 8 inch wafers have been mapped in order to obtain spatially resolved thickness profiles. These experiments were performed at Roth & Rau B.V. using specific mapping software. A Cauchy model has been employed to analyse film thickness. These results are presented in Appendix D.

Transmission Electron Microscopy

Transmission Electron Microscopy (TEM) is a microscopy technique with which high resolution images of nano-structures can be produced.[48] With TEM, a beam of electrons travels through the sample of interest, where it will be scattered dependent on several material properties, such as density of the material. Furthermore, the electrons can be diffracted, dependent on the morphology of the material. Based on these properties, some electrons will be scattered heavily, leading to dark areas, while some electrons will not, leading to bright areas. This leads to contrasts, which are used to construct an image.

TEM was employed to study the conformality of SiN_x films deposited on coupons, containing HARS. Cross-sectional images of the SiN_x samples were obtained on a JEOL 2010F ultra-high-resolution scanning TEM at 200 kV. In order to employ TEM, cross-sectional samples had to be prepared. In order to ensure the deposited SiN_x were protected during preparation of the cross-sectional samples, the SiN_x films were coated with a layer of spin-on epoxy. Hereafter, the SiN_x samples were attached onto a Cu TEM grid, after which they were milled using an ion beam at 30 kV, 100 pA. Finally the cross-sectional samples were polished using a 5kV, 40 pA, ion beam.

The coupons were provided by Lam Research Corporation. The coupons contained high aspect-ratio ($\sim$ 1:4.5) trenches. The lay-out of the coupons is shown in Appendix C. The preparation of the samples and conduction of the TEM experiments referred to in this work were conducted by Lam Research Corporation.

Wet chemical etch-rate experiments

Wet etches have been employed in order to characterize the chemical inertness and barrier properties of thin films. In a wet etch, the sample is dipped in an acid solution (such as HF) for a set amount of time. By comparing film thickness before and after the dip, the wet etch rate can be determined. This rate, i.e. the rate with which material is etched away, is typically an important material parameter for determining the quality.

The samples were dipped into a 100:1 HF solution for 30 s. The wet etch experiments referred to in this work have been conducted by Lam Research Corporation.

3.2 Rutherford Backscattering and Elastic Recoil Detection

In this section Rutherford Backscattering (RBS) and Elastic Recoil Scattering (ERD) techniques will be described. In addition to this, the analysis strategy will be highlighted. Furthermore, the power of the techniques for characterising SiN_x film growth by ALD will be briefly discussed.

3.2.1 RBS and ERD fundamentals

Both RBS and ERD are techniques with which absolute elemental concentrations can be measured. The RBS and ERD experiments and simulations referred to in this work have been performed by AccTecc B.V. in Eindhoven. In this work, both techniques employ high energy (1.8-2 MeV) beams of helium ions (He^+), which are directed on the sample at various angles. The He^+ ions will interact, or even collide, with nuclei in the film. A detector is placed at an specific angle with respect to the incident helium beam. Only a specific fraction of the helium ions are backscattered from the material into the detector and in RBS, the remaining energy of those ions will be measured. How much energy the He^+ ions have lost, mainly depends on the energy that is lost during the collision (which depends primarily on the mass of the nuclei) and on the distance travelled in the material. In other words, a He^+ ion that is backscattered at the surface will have more energy than a He^+ ion backscattered from some depth in the material, which is schematically shown in Figure 3.3. Furthermore, the magnitude of this energy loss depends on several film properties, such as density and composition of the film. A measured energy spectrum, therefore, contains a lot of information about the material. The elements in the film can be quantified with help of simulations which takes the aforementioned effects into account. With traditional RBS however, it is not possible to measure hydrogen atoms. Since hydrogen is lighter than helium, the forward

trajectory of the helium is only altered slightly as a result of interactions with the hydrogen, so no backscattering occurs. Therefore, ERD has been employed. Briefly, with ERD, the He^+ ions hit the surface at very small incident angles, kicking out the hydrogen atoms present in the film. These forward-scattered hydrogen atoms can then be detected by the detector, which should be placed at a small angle with respect to the sample surface as well.

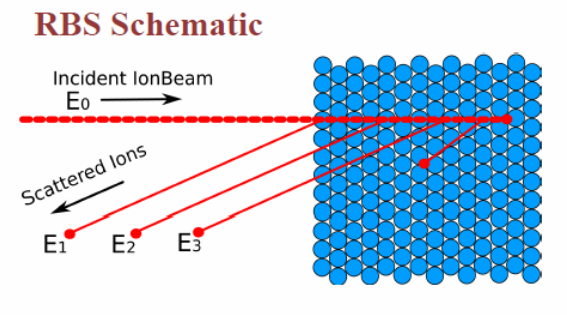

Figure 3.3: Schematic image showing scattered ions with different energies as a function of the depth at which the ion was scattered. The image is obtained from Space Propulsion Laboratory, MIT.

As depicted in Figure 3.3, He^+ ions can scatter from elements, which could be located all throughout the film. The ions ideally would have a specific energy depending precisely on the distance travelled through the material. This would combine elemental concentrations with detailed depth resolution. However, experimental limitations and various other effects can lead to uncertainties in ion energy. As a result of this, the measurements and simulations described above, both lead to a number of atoms per element per unit area, integrated over a particular thickness over which the stoichiometry is constant. Therefore, with RBS it is not possible to acquire detailed depth profiles. Other techniques need to be employed in order to measure more detailed film composition as a function of depth in the film.

3.2.2 SiN_x film analysis

With RBS, elemental concentrations of SiN_x films have been determined. Furthermore, these concentrations can be used to calculate atomic percentages (at.%), number of atoms deposited per deposition cycle per unit area (at./cycle/nm^2) or mass densities (g/cm^3) of specific elements. However, film composition was not always constant throughout the film, as a result of surface oxidation and contaminations. In SiN_x films deposited at lower stage temperatures (100 °C), the relatively large surface contaminations caused the composition of the film close to the air-surface interface to differ significantly from bulk film composition. As a result of this, this air-surface layer could be distinguished from bulk and consequently modelled separately. In those cases, stoichiometry of bulk SiN_x is mentioned. In other cases, so with SiN_x films deposited at higher stage temperatures (> 200 °C), the air-surface and bulk composition did not differ significantly and only one layer could be modelled. In those cases, the combined stoichiometry of air-surface

and bulk SiN_x is mentioned. Note that small surface contaminations and oxidation are present and could have led to a small overestimation of these elements in the SiN_x film. Furthermore, the oxygen that comprised the native oxide layer on the c-Si substrate also introduced some extra uncertainty. However, for this oxide layer has been corrected, since this layer is approximately the same for all samples in this work.

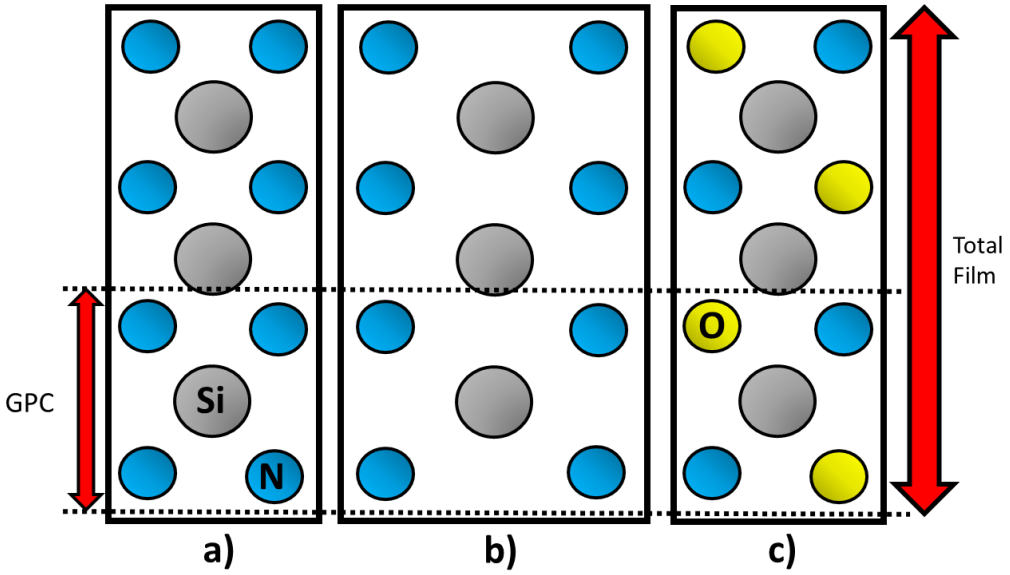

Figure 3.4: A schematic (hypothetical) representation how variations in **b)** film density, **c)** stoichiometry/contamination (for example by the built-in of [O]), can lead to the same GPC as *stoichiometric* material **a)**, illustrating the limitation of using only GPC in terms of thickness for characterising film growth.

3.2.3 GPC

The absolute accuracy of the RBS technique, make it a reliable way to characterise film stoichiometry and density. This absolute accuracy allows for a deconvolution of the GPC, i.e. a decomposition of the total GPC into GPC's of all specific elements in terms of number of adsorbed atoms per cycle per unit area. As is depicted in Figure 3.4, films with different density, stoichiometry or with contaminations can lead to a similar GPC, despite their different material properties. Since, in the process we employed with DSBAS or BTBAS as a precursor, the only source of silicon is the single silicon atom present in the precursor, the number of adsorbed silicon atoms per cycle is a good measure for precursor adsorption. It is assumed that silicon can only end up in the SiN_x film after successful precursor adsorption. Therefore, the number of adsorbed precursor atoms per cycle per unit of area is a better measure for quantifying the growth of a film, compared to the GPC in terms of thickness.

3.3 X-ray Photoelectron Spectroscopy benchmark

In this section the X-ray Photoelectron Spectroscopy (XPS) technique will be briefly described. Moreover, in this section structural and experimental errors have been investigated and specifically benchmarked, for the analysis of SiN_x films. This benchmark has been performed, since conducting a proper XPS measurement on SiN_x films is complex and no standard procedure has been developed for such experiments yet, in our group. It will be discussed how carefully adjusting experimental settings of the XPS measurement can lead to a more reliable determination of the SiN_x film composition. However, XPS usually lacks absolute accuracy because of structural and experimental errors. Combining RBS and XPS is, therefore, a suitable way to combine quantitative and qualitative information about film composition. It will be argued how XPS could serve as an alternative for RBS in determining the absolute film composition, in case this relatively expensive technique is not available. Furthermore, these investigations are meant to raise awareness of the limitations in the XPS analysis of SiN_x thin films.

3.3.1 XPS fundamentals

While techniques like RBS and ERD can give accurate information about absolute film composition, these techniques lack information about chemical properties of the films and the depth profile. XPS is a diagnostic with which the binding energy of elements in the film can be measured. Furthermore, the peak area of the elements present in the film can give information about film composition. To this purpose, however, the peak areas need to be scaled properly, in such a way that the peak areas correspond to actual film composition. These scaling factors are the sensitivity factors, which are obtained by calibration of the XPS setup. By combining XPS measurements with sputtering steps, it is possible to obtain depth profiles, with which the stoichiometry throughout the film can be determined. XPS basics, sensitivity factors and sputtering fundamentals will be discussed separately, in the sections hereafter.

For XPS measurements a Thermo Scientific K-Alpha spectrometer with a Al Kα X-ray source ($h\nu$ = 1486.6 eV) has been employed. XPS involves high energy photons kicking out electrons from the target sample, as is depicted in Figure 3.5. A part of the electrons that are released from the sample will reach the electron analyser, or spectrometer. These electrons will have a specific kinetic energy (E_k), depending on the X-ray photon energy ($h\nu$) of the X-ray and the binding energy of the kicked-out electrons (E_B), or in formula: $E_B = h\nu - E_k - \phi$.[49] In this relation ϕ is the spectrometer work function, of which the value is determined by calibration of the spectrometer and can be considered as a constant. Since ($h\nu$) is known, measuring E_k yields E_B of the specific electron. The counting and subsequent plotting of all electron signals with different kinetic electron energies leads to a distribution of binding energies, or a spectrum. It has to be noted that hydrogen cannot be detected by XPS. This causes a limitation in the determination of the absolute film composition of SiN_x films, which generally contain significant amounts of hydrogen.

One of the strengths of XPS is that the accurate determination of the binding energy of electrons makes it possible to study the bonds present in the film. The obtained spectra can contain multiple

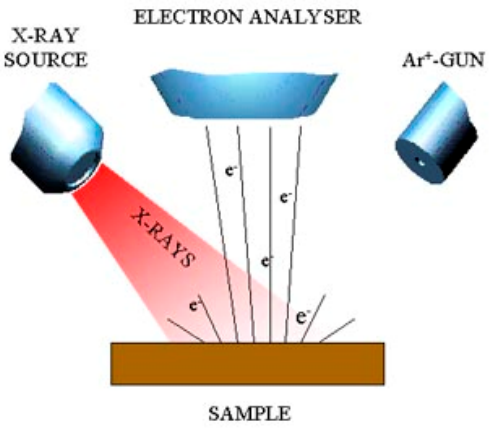

Figure 3.5: A schematic representation of the XPS setup. A beam of high energy photons (X-rays) are used to kick out electrons from the sample. Some of these electrons will reach the electron analyser, in which the remaining kinetic energy of the incoming electrons is determined. This kinetic energy is a measure for the binding energy of the elements in the film, which is the parameter of interest. With an (Ar^+) ion gun, material can be sputtered away, making it possible to obtain depth profiles by alternating sputtering and X-ray steps. The image is obtained from the Belgian Nuclear Research Centre (SCK·CEN)

peaks, which can represent multiple bonding chemistries of the element of interest. For example, not only [C] can be measured, but also whether it is likely to be bonded to an N-atom, or to another C-atom. In order to do this, the spectra need to be deconvoluted into several peaks, which is depicted in Figure 3.6 for [C] in a SiN_x film, deposited at a stage temperature of 400 °C. What can complicate the deconvolution is the observation that peaks of interest can be very close to each other and often even overlap (see Appendix E.3). This can make the identification of peaks complex. Especially when large peaks overlap with small peaks, it is very difficult to distinguish all individual peaks. Furthermore, when the peaks suffer from significant broadening, large peak overlap can make the deconvolution and subsequent identification of chemical bonds increasingly complex. This shows that an accurate determination of the binding energy is key in the identification of the bonds present in the film, which could eventually contribute in the understanding reaction mechanisms. In order to also quantify the bonds present in the film, the peaks need to be properly scaled, for which the sensitivity factors are used.

Sensitivity factor

The sensitivity factors scale the measured peak areas in such a way that the peak areas are representative of the actual concentrations of the elements present in the film surface. Those scaling factors have been determined via calibration measurements. In these calibrations, samples with known composition are analysed and used to scale the measured peak areas with the known film compositions. These sensitivity factors were determined previously and can be found in Appendix

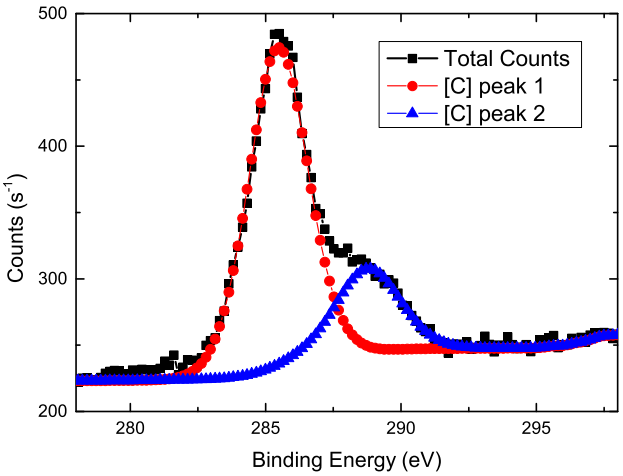

Figure 3.6: An example of peak deconvolution of the [C] spectrum. Two peaks have been identified, as C bonded to N (C-N) and a carbide (Si-C) (see Appendix E.3). The SiN_x film was deposited at a stage temperature of 400 °C.

E. The sensitivity factors can be replaced when more accurate calibrations are available. The errors in the accuracy of the sensitivity factors used in this work are typically $< 1\%$.

Sputtering step

As already briefly mentioned before, depth profiles can be obtained when XPS measurement are combined with a sputtering step. In order to do so, material has to be sputtered away from the surface before doing the actual measurement. In this work, Ar^+ ions are used to sputter material away from the surface of the SiN_x films. The energy of the ions can be controlled between 100 eV and 3 keV. In this work, Ar^+ ions with energies of 500 eV are used. As a result of the sputtering with the positively charged Ar^+ ions, positive charge can accumulate on the surface. An electron flood gun is used to compensate for this charge accumulation, by directing a beam of low energy (0 - 0.5 eV) electrons at the surface. However, it can take finite time for all charge is compensated, which can influence the binding energy of the electrons. Furthermore, the use of Ar^+ ions can lead to the preferential sputtering of one of the elements in the film. Preferential sputtering can depend on the energy of the Ar^+ ions used for sputtering. The effects of charging and preferential sputtering on the analysis of SiN_x films will be discussed in the next section.

3.3.2 Experimental and structural errors

In the upcoming paragraphs will be discussed how several experimental effects can lead to shifts in binding energy, errors in absolute peak areas of the measured peaks and errors in stoichiometry,

in SiN_x films. That is also how this section will be structured. First of all, it will be discussed how uncertainties in the determination of the binding energy can complicate the identification of the bonds present in the spectra. Secondly, it will be discussed how uncertainties in peak area can influence the determination of the absolute film composition. A strategy will then be described how binding energy and peak area can be corrected for. Furthermore, it will be discussed how preferential sputtering can lead to errors in the quantitative film composition. Finally, this section will be concluded with recommendations and a brief overview of important limitations that need to be taken into account when conducting XPS experiments on SiN_x films.

Binding energy

In a typical XPS experiment spectra of multiple elements are obtained at a specific depth in the film. In order to obtain a depth profile, material has to be sputtered away from the surface before doing the actual measurement. During such an Ar^+ sputtering step, charges will accumulate on the newly exposed surface layer. A flood gun is employed to correct for this positive charge on the surface. The energy of these electrons in the flood gun is, however, relatively low (0 - 0.5 eV) to prevent negative charging of the surface. For conductive samples, the excess positive charge is transported rapidly to the ground, but for insulating materials this takes more time. The accumulated net positive charge will produce a retarding electrical field that slows down the electrons that are emitted from the surface.[49] Since the electrons are slowed down, this effectively reduces E_K, which consequently leads to higher apparent E_B (as described in section 3.3.1). It takes finite time before all this excess charge has disappeared, even when the earlier mentioned flood gun is applied. This is depicted in Figure 3.7 **a)**. In this experiment, the effect of charge compensation is visualised by repeating measurements of the peak position of the elements [O] and [Si], after the same sputtering step. In other words, multiple measurements of the binding energy were conducted after increased waiting times, or delay, after the sputtering of the film. It can be observed that the electrons measured directly after the sputtering step suffered from the retarded electrical field. As a result of the retarding field, E_K of these electrons was reduced and subsequently, the apparent peak position (or binding energy: E_B), was too high. When the time between sputtering and XPS measurement (t_{meas}) is long enough, a shift of the measured E_B of both the [O] and [Si] to an equilibrium value E_{B-eq} can be observed. Based on these curves, it can be determined what the overestimation (ΔB) of the actual peak position (E_{B-eq}) is, at every possible time (t_{meas}) of conducting the XPS measurement after sputtering. Therefore, in order to determine E_{B-eq}, the measured E_B of these elements has to be reduced by ΔB.[49] Since ΔB is a function of time, the time of the XPS measurement after the sputtering step (t_{meas}) has to be known in order to accurately determine ΔB and correct the binding energy accordingly. This will be shown further in this section, where these correction factors will be determined.

Peak Area

Ideally, XPS can also be used to quantify film composition. However, quantification of the film composition by XPS is difficult, since multiple factors can introduce errors in the measured peak

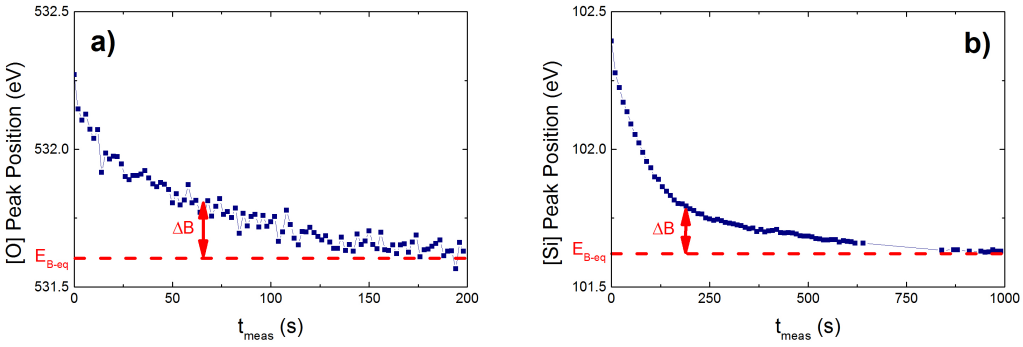

Figure 3.7: Oxygen peak position **a)** and silicon peak position **b)** as a function of measurement delay after sputtering (t_{meas}). After every sputtering step positive charges have accumulated on the surface. This leads to an electrical field which slows down the electrons that are kicked out of the surface. As a result of this, the the kinetic energy of the electrons can be reduced, which can lead to an overestimation of the extracted binding energy (E_B). This can lead to an overestimation (ΔB) of the actual binding energy (E_{B-eq}), which is indicated by the red dotted line. ΔB depends on the time of the measurement after sputtering and can be used to correct the measured E_B when t_{meas} is known.

area or measured composition. In order to calculate the stoichiometry, the peak areas of the deconvoluted peaks of all elements in the film (as shown for [C] in Figure 3.6) are calculated and summed. One of the factors that influences the peak area is ion induced oxidation. Ion induced oxidation occurs readily, which is demonstrated when ambient oxygen bonds to the exposed top surface of the SiN_x. This oxidation can lead to an overestimation of the oxygen content, depicted in Figure 3.8 **a)**. It can be observed that the oxygen content measured at about 150 s has increased with more than 50 % with respect to the [O] peak area measured directly after the sputtering step. This big increase in [O] leads to an underestimation of the concentration of other elements in our film, depicted in Figure 3.8 **b)**. This underestimation has been visualised by repeating measurements of the peak area of [Si], after the same sputtering step. It is assumed that the Si trend is representative for [C] and [N] as well. Since the surface of SiN_x films typically oxidises readily, we hypothesize that the bonded oxygen atoms blocks the other elements that are located in the few monolayers below the surface. This would explain the slight decrease of the normalised [Si] peak area over time, which can be observed in Figure 3.8 **b)**. Therefore, the measured peak area (S) of the measured [Si], [N] and [C] elements have to be increased with a correction factor (ΔS), in order to obtain the actual peak areas S_{eq}. For [O], the measured peak area (S)has to be decreased by a correction factor (ΔS). Since ΔS is a function of time, the time of the XPS measurement (t_{meas}) after the sputtering step has to be known in order to accurately determine ΔS and correct the peak area accordingly.

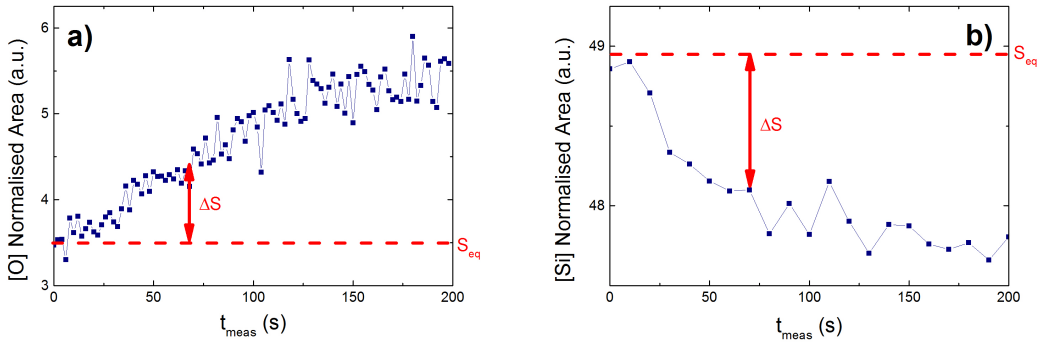

Figure 3.8: Oxygen peak area **a)** and silicon peak area **b)** as a function of measurement delay after sputtering (t_{meas}). Oxidation of the measured surface during the XPS measurement lead to structural errors, e.g. an overestimation of [O] content and underestimation of [Si] content. The magnitude of ΔS depends on the time of the measurement after sputtering and can be used to correct the measured S when t_{meas} is known.

Correcting peak area and binding energy

Above, it has been explained how the binding energy shifted as a result of charging. It was shown how ΔB can be used to correct E_B, such that E_{B-eq} is obtained. It was shown how ΔB depends on the time delay after the sputtering step (t_{meas}), as was shown in Figure 3.7. When all 4 elements ([O], [Si], [C] and [N]) are measured, each measurement will take place after one another, resulting in different time delays (t_{meas}) after the sputtering step. Therefore, the binding energy of every element needs to be corrected with a different charging shift. These charging shifts are shown in Table 3.3, where $<t_{meas}>$ denotes the average measurement time after the sputtering step. Since all measurements have a duration of either 10 or 30 s, $<t_{meas}>$ was determined per element, by summing t_{meas} at the beginning and end of the measurement and dividing this number by 2.[a] It can then be observed that significant shifts (0.5-0.7 eV) are required in order to obtain E_{B-eq}. It has to be noted that a validation of the corrected binding energies by comparing with the literature is difficult, since binding energies of peaks reported in the literature typically spread out over a significant range, which is shown in Appendix E.3. Furthermore, it is unknown whether the values reported in the literature took charging effects into account. A similar strategy as just described, was also employed in the correction of the peak area.

In the previous section, it has been explained how peak area was affected as a result of ion induced oxidation. It was shown how ΔS can be used to correct the measured peak area, such that the actual peak area S_{eq} is obtained. However, rather than estimating an offset (ΔS) for all elements, a correction (multiplication) factor was determined in order to convert the measured S into the *actual* S_{eq}. This was necessary since the magnitude of the peak area varied per element. Using similar argumentation as described in the correction of the binding energy, also for the measurement of

[a] An example for calculating $<t_{meas}>$ for carbon: The measurement starts 25 s after the sputtering step, has a duration of 30 s and, therefore, ends 55 s after the sputtering step. $<t_{meas}>$ = (25+55)/2 = 40 s.

Table 3.3: All steps involved in an XPS experiment for SiN_x films. For the measurement of every element, the average measurement delay $<t_{meas}>$ has been shown. $<t_{meas}>$ was calculated by determining the times at the beginning and end of the measurement of an element, summing the two times and dividing the number by 2. The table shows the benchmarked correction factors, in order to obtain the corrected binding energy and peak area. It is specifically recommended that [O] is measured first, since ion induced oxidation influences the [O] peak area the most significantly.

Step	Duration (s)	$<t_{meas}>$ (s)	Charging shift (eV)	Oxidation factor
Waiting step	5	-		
Oxygen	10	10	0.7	0.96
Silicon	10	20	0.6	1.01
Carbon	30	40	0.5	1.01
Nitrogen	10	50	0.5	1.02

the peak area of each of the elements ([O], [Si], [C] and [N]) correction factors were determined, shown in Table 3.3. Since ion induced oxidation influenced the [O] content very drastically, this element was measured first.

Note that the atomic concentrations mentioned in the next section 3.3.2 are calculated using the corrected peak areas, according to the strategy just described. XPS results described further in this work, also mention the corrected binding energies and peak areas.

Stoichiometry errors

In this section errors regarding the stoichiometry will be discussed. It will be shown how preferential sputtering can lead to small errors in the measured stoichiometry. Note that the limited accuracy of the sensitivity factor (typically $< 1\%$) also introduces an uncertainty in the stoichiometry. Furthermore, no hydrogen can be measured via XPS, which is a limitation that needs to be taken into account when determining stoichiometry with XPS.

Preferential sputtering can cause specific elements in the film to be sputtered away more readily than others. This can be a source for uncertainty in stoichiometry. However, it is unknown whether this also occurs in SiN_x films and what the impact is. Therefore, to investigate what the influence of ion beam energy is, stoichiometry has been measured as a function of ion beam energy (0.1 - 3 keV) for SiN_x films deposited at 400 °C, of which the results are shown in Table 3.4. In Appendix E, stoichiometry of films deposited at 200 °C can be found for different sputtering energies, which shows quite similar results. Looking at the stoichiometry results, it can be observed that the measured stoichiometry is rather constant as a function of ion beam energy. However, a few trends can be observed. First, it can be observed that an increasing ion beam energy leads to an increase of the measured [O] content, which seems to correspond better with the results obtained via RBS. This increase in oxygen content is likely to be caused by increased surface oxidation, as

Table 3.4: The effect of varying ion beam energy during the sputtering step on the film stoichiometry, at 400 °C . RBS concentrations are used as a reference, with which the XPS concentrations can be compared. In order to compare these absolute concentrations, the XPS values are scaled using the [H] content as determined with RBS ([H] content: 4.5%).

Ion Beam Energy (eV)	C at.%	O at.%	Si at.%	N at.%	N/Si
200	1.6	2.4	41	51	1.3
1000	1.6	2.8	40	51	1.3
3000	1.6	3.3	40	51	1.3
RBS ref	2.3 +/- 0.9	3.4 +/- 0.5	38 +/- 1	52 +/- 1	1.4 +/- 0.1

a function of increasing ion beam energy. The [Si] content seems to be slightly overestimated by a value of roughly 2 +/- 1 %, independently of ion beam energy. The [N] content though, seems to be underestimated slightly. This underestimation of the [N] content also seems to be independent of ion beam energy. Because of the overestimation of [Si] content and underestimation of N content, the N/Si value as determined with XPS is slightly lower compared to the reference RBS value. Altogether, the results show that the obtained film stoichiometry is rather constant at different ion beam energies, indicating preferential sputtering is not a big issue that needs to be taken into account in the analysis of SiN_x samples.

3.3.3 Recommendations

In the previous sections, it has been investigated for SiN_x films how charging and ion induced oxidation in XPS experiments can affect the binding energy and peak area. Furthermore, it has been investigated how the stoichiometry of the SiN_x films changed as a function of increased ion beam energy, when XPS is combined with a sputtering step. Finally, it was shown how some elements might be slightly underestimated or overestimated, by comparing stoichiometry obtained by XPS with stoichiometry obtained by RBS of the same SiN_x film. In this sections these findings will be summarised and implemented into a set of recommendations and limitations.

The observations have led to two recommendations. Since ion induced oxidation affects the oxygen content severely as function of time, it is advised to first measure the oxygen content in a XPS experiment. Since a typical SiN_x XPS experiment consists of four independent measurements ([O], [Si], [C] and [N]), this recommendation is easy to implement. Furthermore, it is shown how binding energy and peak area were significantly influenced as a function of the time of the measurement, after the sputtering step t_{meas}. These correction factors have been determined and can be used to correct the measured binding energy and peak area in future experiments into stoichiometry of SiN_x films, in order to obtain more accurate values. More generally, it is important to realise that this correction has led to significant shifts in the binding energy (0.5 - 0.7 eV). Unfortunately, it is often not clear whether other references have investigated and corrected for charging in their

setup, which can complicate the comparison of binding energies.

In addition to these recommendations, also some important limitations need to be taken into account. By comparing stoichiometry of XPS with the stoichiometry as determined with RBS, it appeared that the XPS measurements showed an overestimation of the measured [Si] and [O] content and an underestimation of the measured [N] content. These findings are consistent over this small dataset, but it needs to be stated that the values are also only on the verge of being significant. Two other inevitable limitations for determining absolute SiN_x composition with XPS are caused by the limited accuracy of the sensitivity factor (typically $< 1\%$) and the fact that no [H] content is measurable with XPS. Since in this work, typically 5-10% of the SiN_x films consist of [H] (which will be shown in Chapter 4), absolute composition cannot be obtained accurately and RBS is recommended for detailed, absolute, quantification of thin films. However, considering the typical low uncertainties in the sensitivity factors, XPS can still be considered as a powerful and reliable diagnostic in order to draw quantitative conclusions, i.e. when comparing the similar material deposited under different experimental conditions.

Chapter 4

Process Development

One of the main goals of this work comprised the development of a plasma-assisted ALD process using DSBAS, a novel aminosilane precursor, to grow high-quality SiN_x films at low temperatures. In order to make this chapter a solid base for potential publication, the process development will be described in paper style. The process development results will be presented in section 4.3 and will cover saturation curves and material characterisation.

Abstract

The deposition of high quality SiN_x layers is required in the manufacturing of state-of-the-art transistors, such as FinFETs. A low thermal budget is essential for application of SiN_x as gate spacers in such transistors. In this work we employed a novel precursor Di(*Sec*-Butyl)AminoSilane (DSBAS, $SiH_3N(C_4H_9)_2$) to develop a plasma-assisted ALD process to grow high-quality SiN_x at low substrate temperatures (< 400 °C). Material properties have been analysed over a wide stage temperature range (100 - 500 °C) and compared with properties of a similar aminosilane precursor Bis(*Tert*-Butyl-Amino)Silane (BTBAS, $SiH_2[NH(C_4H_9)]_2$), studied in our previous work. With DSBAS, high quality films were obtained compared to those obtained with BTBAS and those reported for other precursors in literature, yet the obtained GPC values were relatively low (typically between 0.01 and 0.02 nm). The films typically showed low contamination ([C] and [O]) and [H] contents, high mass densities and N/Si values close to that of stoichiometric Si_3N_4. Wet-etch experiments showed no significant etching of the SiN_x on top of planar surfaces even at low stage temperatures (300 °C), confirming the robustness of the SiN_x films. The findings support a hypothesis that can explain the differences in material properties between BTBAS and DSBAS on

the basis of the surface reactions during the ALD process.

4.1 Introduction

SiN_x is one of the most widely used materials in various thin-film applications, including micro- and nanoelectronics.[1] An important application of SiN_x is as a side-wall gate spacer in Field Effect Transistors (FETs), where it can have multiple functions. An important function of SiN_x is as a barrier layer, in order to protect the high-k metal gate (HKMG) stack.[2] Since HKMG stacks are sensitive towards oxygen ingress and damage during later processing steps, it is necessary to encapsulate them with a high-quality barrier layer.[9] Furthermore in transistor technology, SiN_x can also be important in defining source and drain regions in FETs, in strain engineering for increasing channel mobility or as a hard mask in spacer defined patterning.[2–6] An overview describing these various applications of SiN_x films in FETs has been given in Chapter 2.

In future transistor processes, it becomes more and more critical that substrate temperatures are kept low (< 400 °C).[8] In addition to low deposition temperatures, current FinFETs and other future three-dimensional FET-architectures require precise thickness control, high quality films showing low wet etch rates and high conformality in three-dimensional structures.[15] Generally, chemical vapour deposition (CVD) processes are not able to provide this precise thickness control at low deposition temperatures.[15] The self-limiting nature of ALD can offer this offer precise thickness control.[13] Therefore, ALD can be considered as a suitable alternative over more conventional CVD processes. However, thermal ALD processes are typically not able to fulfil these requirements in order to grow high quality films at low temperatures.[1] Plasma-assisted ALD is expected to provide a suitable alternative deposition process for these applications. However, growing high quality and highly conformal SiN_x is not trivial to achieve, even with plasma-assisted ALD.[17]

Multiple thermal ALD processes have been demonstrated and conformal SiN_x film growth has been reported in the literature, using a variety of precursors and reactants.[50–54] For plasma-assisted ALD of SiN_x, only a handful of studies have been reported in the literature.[1,2,8,13–15] Ovanesyan *et al.*[8] provided an elaborate overview of these ALD processes, both thermal and plasma-assisted. Therefore, only a brief overview of plasma-assisted ALD processes will be given here.

Silicon hydride precursors, like silane (SiH_4) have been used in combination with an N_2 plasma at low temperatures (< 400 °C).[15] However, there are concerns whether this process is really a self-limiting ALD process, while also the long cycle times (> 1 minute) make this process less attractive for commercial employment. Other processes make use of silicon halides, e.g. Si_2Cl_6 recently employed by Ovanesyan *et al.*[8] in combination with a NH_3 plasma. At relatively low temperatures (350 °C - 450 °C) they were able to deposit SiN_x films showing high conformality (>95%) with a growth per cycle (GPC) of ~ 1.2 Å. However, relatively large amounts of hydrogen $\sim 23\%$ were incorporated in the films which had a low mass density of 2.35 g/cm^3. In addition to that, halide containing precursors are not preferred since they can cause the incorporation of chlorines in SiN_x films, which can lead to detrimental effects.[17]

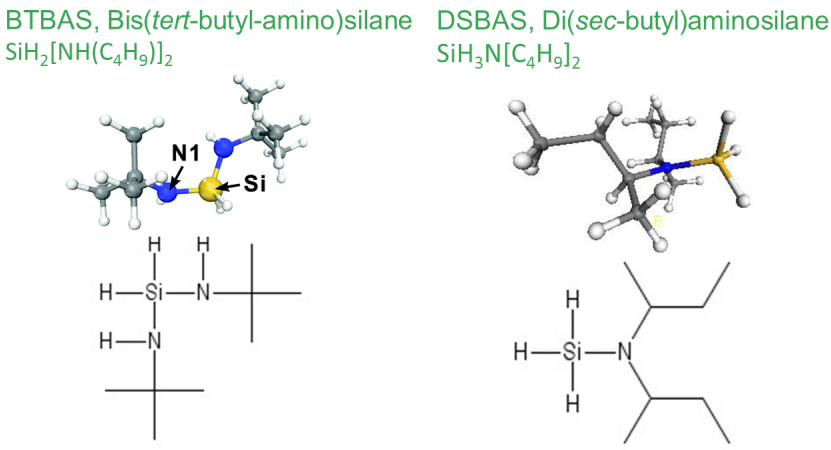

Figure 4.1: Schematic representation of both the DSBAS and the BTBAS precursor. The DSBAS precursor consists of one aminosilane ligand, whereas the BTBAS precursor consists of such ligands.

Aminosilane precursors can offer a halide-free alternative. Knoops *et al.* [14] developed a SiN_x process employing a Bis(*Tert*-Butyl-Amino)Silane (BTBAS) precursor, depicted in Figure 4.1, in combination with a nitrogen (N_2) plasma. It has been shown by Ande *et al.* [55] that SiN_x film growth by BTBAS is strongly reduced when NH_3, N_2+H_2 or H_2 plasmas were used, explaining the choice for a N_2 plasma over other hydrogen-containing plasmas. Decent quality SiN_x films have been deposited, which is embodied by films with reasonable contamination contents ([C]<10% and [O]<5%). Moreover, the [H] content was relatively low (<11%) and low wet etch rates were obtained ($\sim$ 0.2 nm/min at 400 °C). [14]

In another study, Knoops *et al.* [21] focused on the identification of the key parameters that rule the film quality of SiN_x films deposited by plasma-assisted ALD. They showed how redeposition of fragments of BTBAS-ligands, which contain carbon and hydrogen, can have a big role in determining the quality of the film. [21] Knoops *et al.* [21] showed that carbon-containing ligands remain on the surface after the precursor half-cycle. In the subsequent plasma half-cycle, they showed how the remaining ligand is removed by the energetic plasma. However, once these ligand fragments enter the plasma, the fragments can readily dissociate into reactive species, which could redeposit on the surface of the sample. Knoops *et al.* [21] identified the gas residence time as the key parameter that rules the film quality. Furthermore, they showed that lowering the residence time led to an increased film quality, which was demonstrated by SiN_x films with high wet-etch resistance ($\sim$ 0.5 nm/min).

However, these findings also suggest another method to increase film quality, by preventing the redeposition of ligand fragments altogether. Hypothetically, this could be achieved by designing a precursor that contains only one carbon-containing ligand. In this case, ideally the ligand would be released in the precursor half-cycle. This would prevent its presence in the reactor in the plasma half-cycle, where dissociation of the ligands by the plasma could lead to redeposition.

Therefore, a novel precursor, Di(*Sec*-Butyl)AminoSilane (DSBAS), has been employed to test this hypothesis. DSBAS only contains one carbon-containing ligand, but an equal amount of carbon atoms. In Figure 4.1 this has been visualised by comparing DSBAS to BTBAS. The absence of a second ligand, and consequent reduction of the redeposition-effect, is hypothesised to lead to higher quality films.

4.2 Experimental setup

The deposition experiments were carried out using a FlexAL®ALD reactor, which has been developed by Oxford Instruments Plasma Technology. The plasma is produced by a remote inductively-coupled plasma (ICP) source. The plasma RF source operates at a frequency of 13.56 MHz with a maximum input power of 600 W. The set temperature of the substrate table, to which from now on will be referred to as stage temperature, can be controlled between 25 and 500 °C. Due to poor thermal contact between the stage table and sample, the actual sample temperature is lower than the stage temperature. The relation between substrate and stage temperature has been discussed in Chapter 3. Furthermore, the reactor is equipped with a butterfly valve, with which the pressure in the reactor can be accurately controlled. Other specifics of the reactor have been reported more elaborately in earlier work from our group.[45]

SiN_x films have been deposited via a plasma-assisted atomic layer deposition (ALD) process using a Di(Sec-Butyl)AminoSilane (DSBAS) precursor and a N_2 plasma (the MSDS for DSBAS is given in Appendix A). Depositions have been performed on c-Si substrates with a thin native oxide layer ($\sim$ 2 nm). DSBAS precursor was contained at a bubbler temperature of 40 °C and was vapour drawn into the reactor. During this step the butterfly valve was completely closed, in order to confine the precursor in the reactor. After this, via a three second soaking step the precursor was granted extra time to react with the surface. During this step the butterfly valve was opened slightly at an angle of 10 ° to prevent the build-up of high pressures in the reactor. This was necessary, because during all steps a continuous 50 sccm flow of inert N_2 gas was introduced into the reactor through the plasma source. This N_2 gas flow is used to prevent the precursor from adsorbing on the surface near the ICP-source in the reactor chamber. After the reaction step, the reactor was purged using an nitrogen flow of 50 sccm, while the butterfly valve was completely open at 90 °. A two seconds gas stabilisation flow ensured a stable N_2 gas flow of 100 sccm at a minimum pressure of 12 mTorr (the butterfly valve was completely open now) before the N_2 plasma was ignited, for the reactant step of the cycle. After the plasma exposure the reactor was purged again and the cycle was completed.

In order to confirm basic ALD film growth, a set of saturation experiments was conducted. The deposition parameters of the saturation experiments were based on the experience with the previously developed ALD process using BTBAS, which is a very similar aminosilane precursor.[21] These deposition parameters are given in Table 4.1. Compared to the BTBAS standard process parameters, a lower plasma pressure was chosen to reduce the residence time and reduce the potential redeposition-effect.

Table 4.1: Process parameters for the DSBAS and BTBAS experiments mentioned in this work. In the saturation experiments, only one parameter has been varied at a time. The DSBAS standard process parameters were determined after carrying out the saturation experiments. The BTBAS standard process has been described by Knoops *et al.* [14].

Parameter	DSBAS		BTBAS
	Saturation Exp.	Standard Cond.	Standard Cond.
Stage temperature (°C)	400	100-500	100-500
Precursor dose (ms)	100	100	150
Precursor purge (s)	5	1	1
Reaction step (s)	3	3	3
Plasma exposure (s)	5	10	10
Plasma purge (s)	5	1	1
Plasma power (W)	600	600	600
Plasma pressure (mTorr)	12	12	40

4.3 SiN_x film and growth analysis

4.3.1 Saturation experiments

GPC saturation curves as function of precursor dose time, plasma exposure time, precursor purge time and plasma purge time were produced via *in-situ* SE measurements. The results are depicted in Figure 4.2. First of all it can be noticed that typical GPC is relatively low (< 0.1 Å). Furthermore, typical ALD-behaviour can be observed in Figures 4.2 **(a)**, **(c)** and **(d)**. In these figures, it can be seen how the GPC saturates rapidly as a function of DSBAS precursor dose time, precursor purge time and plasma purge time, which is typical for self-limiting half-reactions in ALD. The rapid saturation of the GPC as function of DSBAS precursor dose implies that the DSBAS precursor quickly occupies the available reactive surface sites. The rapid saturation of the GPC as function of both the precursor purge time and the plasma purge time, indicates that the DSBAS precursor and plasma species are purged out of the reactor efficiently. Contrary to this typical ALD behaviour, the GPC as a function of N_2 plasma exposure time shows only soft saturation. This soft saturation can be observed in Figure 4.2 **(b)**, where it can be seen that the GPC has not saturated yet after a plasma exposure of 20 s. This soft saturation is unlike self-limiting behaviour of half-cycles typically observed in ALD (see Chapter 1), and will be further discussed in the Discussion 4.4.

Based on these findings a standard process was defined, of which the most important process parameters are shown in Table 4.1. Ideally, all process parameters are chosen, such that the GPC is in saturation. Therefore, purge times of 1 second were chosen in order to ensure all species

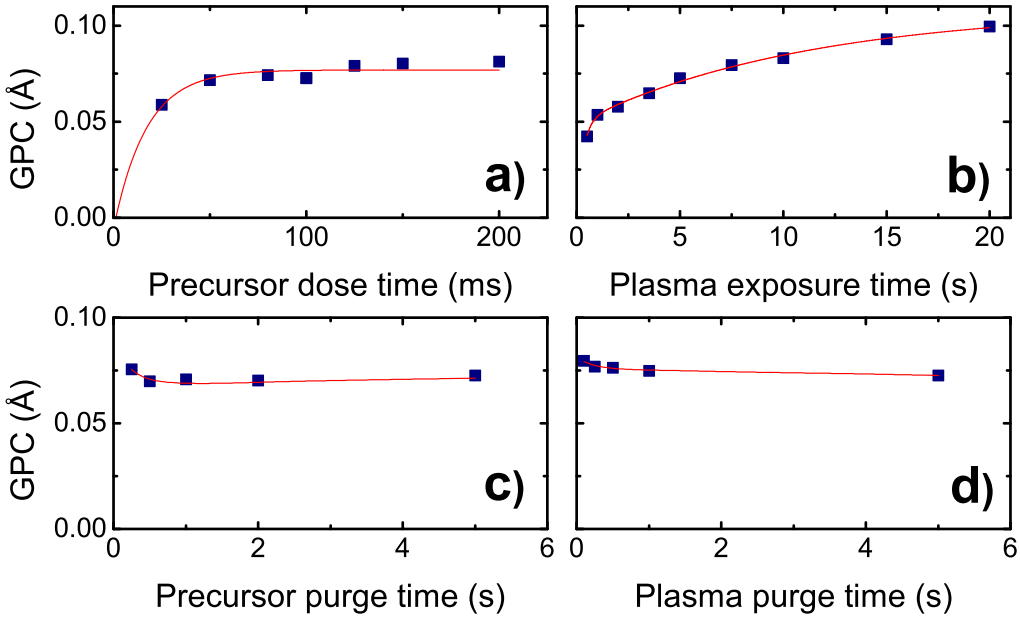

Figure 4.2: Growth per cycle (GPC) as determined with in-situ spectroscopic ellipsometry as a function of ALD parameters at a stage temperature of 400 °C (actual wafer temperature is $\sim$ 320 +/- 20 °C, see Table 3.1). GPC as a function of precursor dose time **(a)**, plasma exposure time **(b)**, precursor purge time **(c)** and plasma purge time **(d)** are shown. The red lines serve as a guide to the eye.

were purged out of the reactor after each half-cycle, so no CVD could occur. As shown before, however, the GPC showed soft saturation as a function of plasma exposure time. The choice of a long plasma exposure time ($\geq$ 20 s) would result in film growth closer to saturation. This would simultaneously also result in long cycle times ($\geq$ 30 s). Considering the low GPC and the subsequent long deposition duration ($\sim$ 20 hours) to grow SiN_x films (of 30 nm[a]), a plasma time of 10 s was chosen to reduce cycle time ($\sim$ 20 s), while maintaining a relatively acceptable GPC. This motivated a precursor dose time of 100 ms. Looking at Figure 4.2 **(b)**, a precursor dose time of 100 ms is roughly double the precursor dose time required for saturation, combined with a plasma exposure time of 5 s (50 ms). As a result, a 100 ms precursor dose is expected to be a sufficient precursor dose to also result in saturated film growth with an increased plasma exposure time of 10 s.

Table 4.2: GPC, refractive index at 2 eV, mass density, and elemental composition of SiN_x films deposited at various stage temperatures. Typical uncertainties are given in the first row. Note that stage temperature is typically lower than substrate temperature (see Table 3.1).

Stage temp. (°C)	Plasma pressure (mTorr)	GPC (Å)	Refractive index	Mass density (g/cm^3)	N/Si	RBS [C] at. %	RBS [O] at. %	ERD [H] at. %
100	12	0.19 +/- 0.02	1.86 +/- 0.05	2.34 +/- 0.05	1.9 +/- 0.1	11[a]	2 +/- 1%	11 +/- 1%
200	12	0.12	1.93	2.70	1.4	3 +/- 1.5%	3	7
200	40	0.12	1.89	2.67	1.5	6	4	8
300	12	0.10	1.98	2.89	1.3	2	3	5
400	12	0.09	1.99	3.06	1.4	2	1	5
500	12	0.10	1.97	3.14	1.6	<2	<1.4	5

[a]Uncertainty of 5%

4.3.2 Characterisation of the SiN_x films

SiN_x film growth has been confirmed over a wide range of stage temperatures between 100 and 500 °C. Material properties and film growth have been characterised at several temperatures in this range. The results are depicted in Figure 4.3 and listed in Table 4.2. Note that the DSBAS results in Figure 4.3 are accompanied with previously obtained BTBAS results, in order to facilitate comparisons between the material properties of the two precursors.

In Figure 4.3 **(a)** it can be observed that the GPC of films grown by DSBAS is significantly lower than the GPC of films grown by BTBAS. This difference is more pronounced at lower stage temperatures, while at 500 °C the difference has reduced to roughly 0.05 Å. The GPC of films grown by DSBAS was fairly constant over temperature ($\sim$0.1 Å), with the exception of 100 °C, where the growth was significantly higher ($\sim$0.2 Å). This trend of decreasing GPC as function of increasing temperature is comparable to the trend obtained with films grown by BTBAS.

[a]Roughly the minimum film thickness required for accurate material characterisation with RBS

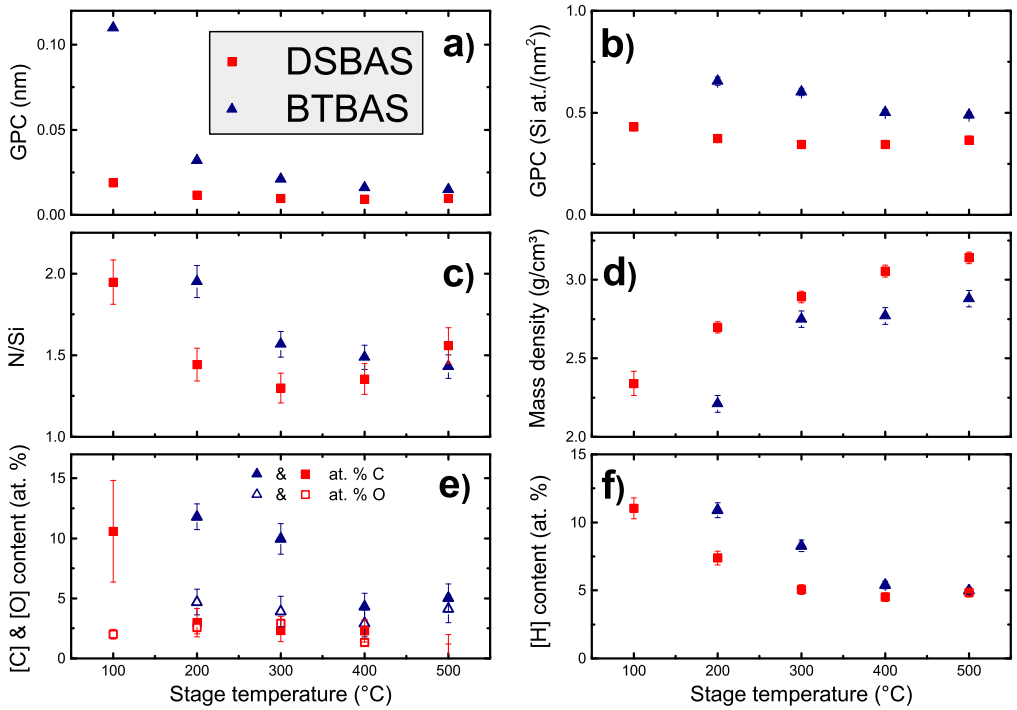

Figure 4.3: Material properties of SiN_x films of DSBAS compared to BTBAS. Total GPC **(a)**, the number of adsorbed silicon atoms per ALD cycle **(b)**, the nitrogen over silicon ratio **(c)**, the mass density **(d)**, carbon [C] and oxygen [O] contamination in atomic % **(e)** and hydrogen [H] content in atomic % **(f)** are shown as a function of temperature. Note that deposition conditions differ slightly for BTBAS and DSBAS series, primarily because of a difference in plasma pressure (12 mTorr for DSBAS, 40 mTorr for BTBAS). Results in **(a)** have been obtained via Spectroscopic Ellipsometry (SE), in **(b-e)** via Rutherford Back Scattering (RBS) and in **(f)** via Elastic Recoil Detection (ERD).

In Figure 4.3**(b)** the number of adsorbed silicon atoms per nm^2 per cycle is shown, denoted as GPC [Si] (at./nm^2). Since the only source of [Si] is the one Si-atom present in both BTBAS and DSBAS precursor molecules, GPC [Si] is considered a measure of the precursor adsorption. It can also be observed how the GPC [Si] stays rather constant ($\sim$ 0.4 at./nm^2) as a function of stage temperature. This deviates from the trend observed for films grown by BTBAS, which shows a monotonic decrease as a function of increasing stage temperature. Furthermore, it can be observed that only a part of the total GPC difference between films grown by DSBAS and BTBAS (Figure 4.3 **(a)** can be explained by this difference in precursor adsorption, especially at low stage temperatures ($\leq$ 200 °C).

In Figure 4.3 **(c)** it can be observed that the N over Si ratio (N/Si) is very close to stoichiometric Si_3N_4 (1.33), especially at 300 and 400 °C (1.3 and 1.4 respectively). At both low ($\leq$ 200 °C) and high (500 °C) temperatures more nitrogen rich SiN_x is grown. This trend differs from the

BTBAS-trend, which shows a monotonic decrease in N/Si as function of increasing stage temperature.

While at 500 °C nitrogen-rich SiN_x was grown, the highest mass density of 3.14 gram/cm^3 was also obtained at this condition, which is depicted in Figure 4.3 **(d)**. This value of 3.14 gram/cm^3 is very close to the mass density of stoichiometric Si_3N_4 (∼3.2 gram/cm^3), which can be obtained via a high temperature deposition process.[56] It can be concluded that DSBAS mass density is higher compared to BTBAS mass density, at all stage temperatures. This indicates that the films are of high quality and this aspect has been confirmed by preliminary wet etch-experiments performed in a diluted HF solution (100:1), of which the results showed no significant etch on top of planar surfaces, even at low substrate temperatures (∼ 250 °C). These wet etch-results will be discussed in more detail in Chapter 5. The high refractive indices, close to 2.0 at stage temperatures $>$ 300 °C (shown in Table 4.2), also indicate that the quality of the films is high.

Contamination ([C] and [O]) and [H]-content of both DSBAS and BTBAS films has also been compared in Figures 4.3 **(e)** and **(f)**. At all temperatures significantly lower [C], [O] and [H] content was obtained for the DSBAS films, compared to the films grown with BTBAS. At a stage temperature of 500 °C, both [C]- and [O]-content has decreased to values below the detection limit, to 2% and 1.4% respectively.

Table 4.3: GPC, refractive index at 2 eV and elemental composition of SiN_x films deposited at 200 °C by either a DSBAS or BTBAS precursor, at different N_2 pressures in the reactor. Typical uncertainties are given in the first row of the specific precursor. Note that stage temperature is typically lower than substrate temperature (see Table 3.1).

Precursor	Plasma pressure mTorr	GPC Å	Refractive index	RBS [C] at. %	RBS [O] at. %
BTBAS	13	0.24 +/- 0.02	1.91 +/- 0.05	5.5 +/- 2	5 +/- 2
	40	0.32	1.83	9.5	5
DSBAS	12	0.12 +/- 0.02	1.93 +/- 0.05	3 +/- 1.5	3 +/- 1
	40	0.12	1.89	6	4

The effect of increased plasma pressure on material properties of both BTBAS and DSBAS SiN_x films is shown in Table 4.3. The films deposited with DSBAS show higher refractive index and lower contamination content at both 12 and 40 mTorr (at 200 °C), compared to the films deposited with BTBAS. Furthermore, the GPC of BTBAS increases significantly when the plasma pressure is increased from 13 to 40 mTorr, whereas the GPC of DSBAS appears to not be affected by an increase in plasma pressure. The [C]-content of the films grown by both precursors show similar behaviour, apparently the film quality degrades somewhat at the higher plasma pressure.

In order to confirm whether the obtained film compositions shown in the previous sections are representative of the whole SiN_x film, depth profiles have been measured. These depth profiles

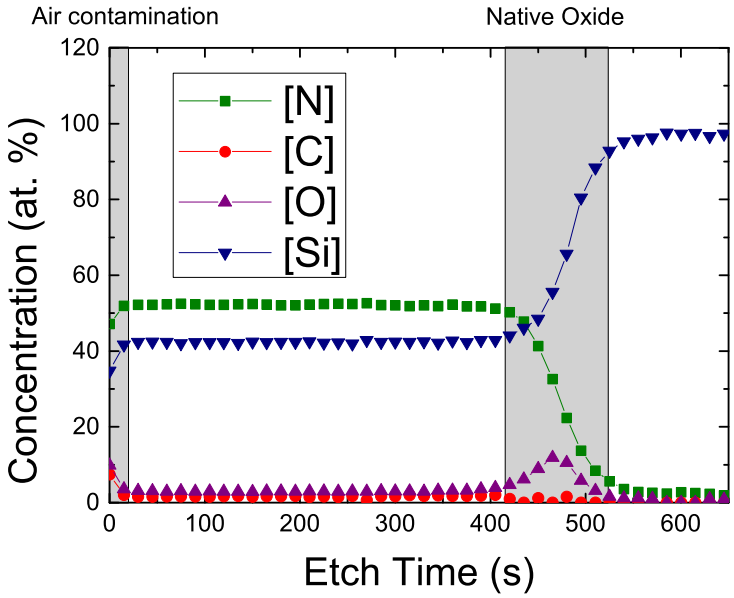

Figure 4.4: Depth profile of a SiN_x film deposited by DSBAS at a stage temperature of 400 °C, as determined by XPS. The native oxide layer can be identified at an etch time of 450 s. Small oxidation and [C] contamination peaks can also be observed near the air-surface interface.

are obtained by alternating XPS measurements and sputter steps and confirm the constant stoichiometry throughout the SiN_x film, which is depicted in Figure 4.4 for SiN_x deposited at a stage temperature of 400 °C. Elevated [C]- and [O]-content can be observed around the air-film interface, indicating some surface contamination. The elevated [O]-content at $\sim$ 450 s can be explained by the native oxide, which is present on the c-Si substrate.

4.4 Discussion

High quality films have been deposited at low stage temperatures ($<$ 500 °C) using the DSBAS precursor. The results show that films with properties relatively close to that of bulk Si_3N_4 (mass density $\sim$ 3.2 g/cm^3) can be obtained.[56] This is demonstrated by stoichiometric N/Si ratios (1.3 +/- 0.2), high mass densities ($>$ 2.9 g/cm^3) and low contamination rates ([C] $<$ 2 +/- 2% and [O] $<$ 3 +/- 1%) at stage temperatures between 300 and 500 °C. Furthermore, preliminary etch results have confirmed the high quality, which will be discussed in Chapter 5. The film quality reduces at lower stage temperatures. At 100 °C the sample suffered from severe surface oxidation near the air-surface interface, probably as a result of the low density of the material ($\sim$ 2.34 g/cm^3).

An important observation is that the typical GPC of films grown by DSBAS ($\sim$ 0.1 Å) is low compared to the GPC of films grown by BTBAS. The GPC, however, denotes the total thickness

increase of the film per cycle and neglects differences in density and stoichiometry (as discussed in Chapter 3). A better measure for comparing film growth between DSBAS and BTBAS, is by comparing the number of adsorbed silicon atoms per cycle per nm^2 (previously defined as GPC [Si][b]). This considered, it was shown that the difference in GPC [Si] between BTBAS and DSBAS was less pronounced, especially at high stage temperatures (> 300 °C). The lower GPC [Si] obtained for DSBAS compared to BTBAS is remarkable though, since the DSBAS precursor saturation curve shows a relatively rapid saturation, indicating a reasonably high reactivity of DSBAS. Support for this high reactivity has been given by Mallikarjunan *et al.*[57], who showed high reactivity of DSBAS in a similar ALD process for the deposition of SiO_2 films. Furthermore, they obtained higher GPC for the deposition of SiO_2 with DSBAS (1.3 Å) compared to BTBAS (1.1 Å), contrary to the results obtained in this work.[57] These results indicate that something is limiting SiN_x film growth in this process with DSBAS. Puurunen[58] showed either the number of reactive surface sites or steric hindrance of the ligands determines saturation of the surface. Since it is likely that steric hindrance is not the limiting factor in this process (which will be explained in Chapter 6), it is likely the number of reactive surface sites is the limiting factor in SiN_x film growth by DSBAS.

Reactive surface sites are created by the interaction of plasma species with the surface. For DSBAS, the GPC as a function of plasma exposure time showed soft saturation, even after 20 s of plasma exposure. This could indicate a slow creation of reactive surface sites. An exponential fit (see Appendix G) demonstrated the growth could be modelled accurately by two exponential functions involving two different time constants, $\tau_1 \approx 0.3$ seconds and $\tau_2 \approx 11$ seconds. This could indicate the presence of two different mechanisms responsible for creating reactive surface sites. However, since no material analysis was conducted on films deposited at different plasma exposure times, we cannot exclude the possibility that the DSBAS material properties change as a result of extended plasma exposure times. One of these effects that could play a role in film growth as a function of plasma exposure time is the redeposition-effect.

In the introduction section of this Chapter, we hypothesised that film quality could be improved by employing a precursor with only one carbon-containing ligand (DSBAS), compared to BTBAS, which contains two. This would result in a lower presence of carbon-containing ligands after the precursor step leading to a reduction of the redeposition-effect. Knoops *et al.*[21] visualised redeposition by observing a peak in GPC and subsequent decrease of GPC as function of plasma exposure time, which is depicted and explained in Figure 4.5. This redeposition-effect is more pronounced at low temperatures (< 300 °C), but still occurs at 350 °C as can be seen by the slightly decreasing GPC at longer plasma exposures. This characteristic redeposition behaviour appears to be absent in the DSBAS saturation curve. Furthermore, a significantly lower [C]- and [H]-content was observed in the SiN_x films deposited by DSBAS compared to BTBAS. This observation supports the hypothesised difference in adsorption mechanism between DSBAS and BTBAS, considering the fact that the total number of C-atoms in the precursors are equal and the number of H-atoms almost equal (22 H-atoms for BTBAS compared to 21 H-atoms for DSBAS). However, a complication arises from the observation that some carbon is also incorporated in films

[b] As argued in the previous section, GPC [Si] is a suitable measure for comparing the precursor adsorption of DSBAS and BTBAS. Since a BTBAS- and DSBAS-molecule both contain one silicon atom.

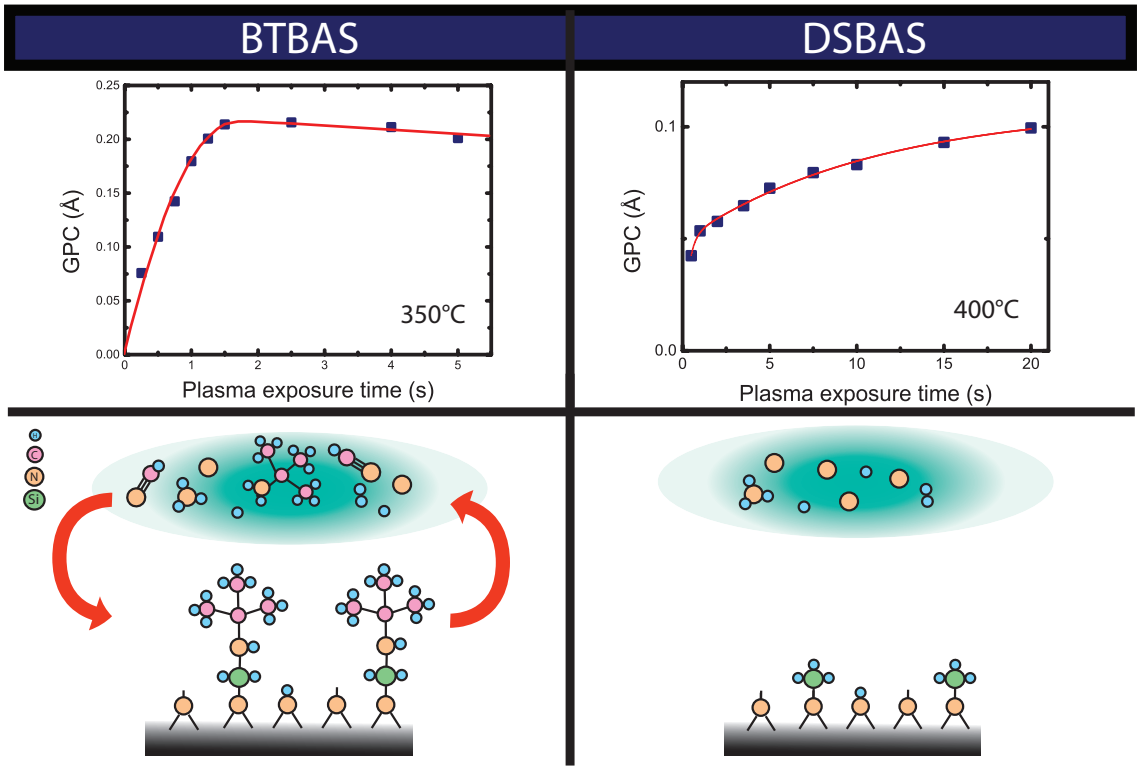

Figure 4.5: The upper images show the GPC of SiN_x deposited by BTBAS (stage temperature of 350 °C) and DSBAS (stage temperature of 400 °C) as a function of plasma exposure time. Note that the BTBAS process parameters (N_2 flow is 50 sccm, precursor dose time is 200 ms and plasma pressure was 25 mTorr) differed from the DSBAS process parameters. The BTBAS curve shows a peak in GPC at $\sim$ 2 seconds of plasma exposure, after which the GPC decreases as a function of increased plasma exposure time. It was suggested by Knoops *et al.* [21] that this peak is caused by redeposition of ligand fragments, which is schematically shown in the lower images. In case ligands are present on the surface when the plasma is ignited, the ligands can be removed and fragmented by the plasma. These reactive ligand fragments can redeposit back on the surface, causing an increase in GPC but decrease in material quality. For DSBAS, no peak in GPC as a function of plasma exposure can be observed. For DSBAS, it is hypothesised a majority of precursor reactions are completed in the precursor half-cycle, resulting in complete ligand split-off. Since almost no ligands are present on the surface in the subsequent plasma half-cycle, there are almost no ligand fragments that can redeposit on the SiN_x surface, explaining the generally high-quality SiN_x films obtained in this work with DSBAS.

deposited by DSBAS, at lower stage temperatures ($<$ 300 °C). This suggests that, in those cases, a significant amount of ligands are not removed after the precursor dose step. Since typically high activation energies (which will be discussed in Chapter 6) need to be overcome for the DSBAS precursor in order to completely split-off the ligand and adsorb to the surface, it is possible that at low temperatures not all those surface reactions have been completed in the precursor half-cycle. Therefore, some ligand parts could still be present on the surface in the beginning of the subsequent plasma half-cycle. In those cases, redeposition of ligand fragments could occur with DSBAS as well. This would also indicate that similar incomplete precursor reactions could occur at the reactor walls, which are relatively cool (150 °C). The remaining ligands, originating from the reactor cool walls, could also redeposit on the substrate surface, even at high stage temperatures. Altogether these findings support the hypothesis, but further investigations are recommended in order to prove this hypothesis.

4.5 Conclusion

We have developed a plasma-assisted ALD process to deposit high quality SiN_x films with a novel precursor DSBAS. Material properties have been characterised over a wide temperature range (100 - 500 °C) and have been compared to films grown with a similar aminosilane precursor BTBAS. DSBAS film growth was slightly lower compared to BTBAS, with GPC values typically lying between 0.01 and 0.02 nm. Overall, SiN_x films of high quality have been deposited with the DSBAS precursor, demonstrated by high mass densities (3.14 g/cm^3 at 500 °C) close to stoichiometric (Si_3N_4) films and low [C], [O] and [H] contents. The high quality is confirmed by preliminary etch results showing no significant etch of the SiN_x films on top of planar surfaces. The findings in this work further support a hypothesised reaction mechanism, in which the use of a precursor with only one amino-ligand would yield higher quality SiN_x films. The low carbon content suggests the majority of the DSBAS ligands are split off in the precursor half-cycle, reducing the redeposition of ligand fragments in the subsequent plasma half-cycle, contrary to the suggested BTBAS mechanism. Altogether, the high quality SiN_x films from this work could be suited as gate spacer in FinFETs and future three-dimensional FETs. However, obtaining conformal SiN_x films is not trivial and needs to be explored as well, which will be discussed in Chapter 5.

Chapter 5

Conformality

One of the main goals of this work comprised the development of a plasma-assisted ALD process with DSBAS, a novel aminosilane precursor, to grow high-quality SiN_x films at low temperatures. Furthermore, potential application of these SiN_x films in future transistors requires a process with which highly conformal depositions in high-aspect ratios can be obtained. In this chapter, the conformality and quality of SiN_x films deposited on high-aspect-ratio structures (HARS) will be studied systematically. In order to make this chapter a solid base for potential publication, it will be described in paper style. Both conformality and wet-etch rates are evaluated through TEM experiments, of which the results will be presented in the Results section 5.3.

Abstract

The deposition of high quality SiN_x layers showing high conformality is required in the manufacturing of state-of-the-art transistors, such as FinFETs. A low thermal budget is essential for application of SiN_x as gate spacers in such transistors. In this work we employed a novel precursor Di(*Sec*-Butyl)AminoSilane (DSBAS, $SiH_3N(C_4H_9)_2$) to develop a plasma-assisted ALD process to grow high-quality SiN_x on high-aspect-ratio structures (HARS) at low substrate temperatures (< 400 °C). Conformality and quality of the SiN_x has been investigated systematically by varying reactor pressure during the plasma, by varying temperature and by comparing with a similar aminosilane precursor, Bis(*Tert*-Butyl-Amino)Silane (BTBAS, $SiH_2[NH(C_4H_9)]_2$). These experiments were conducted in order to identify possible important processes that determine the quality and thickness throughout HARS. The SiN_x films deposited with DSBAS in this work showed high quality, demonstrated by zero wet etch-rates on top and bottom horizontal surfaces. The wet

etch-rate at the vertical side-wall near the bottom (side-near-bottom) showed decreased quality (4 nm/min at 500 °C). The quality further decreased at a reduced stage temperature (12 nm/min at 300 °C). Conformality was not satisfactory, as was demonstrated by reduced film thickness at the bottom (55-65%) and at the side-near-bottom (40-55%) of the trenches. Both the reduced quality and thickness at the vertical side-walls in the HARS, could indicate that the ions play a role in the surface reactions during the plasma-assisted ALD process determining the quality and thickness of the SiN_x film. The results demonstrated the complexity of simultaneously achieving high quality and high conformality and have yielded insight in the parameters that govern quality and conformality.

5.1 Introduction

SiN_x is one of the most widely used materials in thin-film applications. An important application of SiN_x is as a sidewall gate spacer in Field Effect Transistors (FETs), where it can have multiple functions. An important function of SiN_x is the application as barrier layer, in order to protect the high-k metal gate (HKMG) stack.[2] Since HKMG stacks are typically very sensitive towards oxygen ingress and damage during later processing steps, it is necessary to encapsulate them with a high-quality barrier layer.[9] Furthermore in transistor technology, SiN_x can also be important in defining source and drain regions in FETs, in strain engineering for increasing channel mobility or as a hard mask in spacer defined patterning.[2–6] An overview describing these opportunities for SiN_x in transistor applications has been given in Chapter 2.

Current FinFETs and future three-dimensional architectures require low temperature processes ($<$ 400 °C) with precise thickness control, high-quality films showing low wet-etch rates and high conformality in three-dimensional structures.[15] In Chapter 4 it is described how we developed a low temperature plasma-assisted atomic layer deposition (ALD) process, with which we were able to grow SiN_x films that met most of those requirements. However, growing highly conformal and high quality SiN_x films in high-aspect-ratio structures (HARS) is not trivial to achieve, not even with ALD.[17]

Typically not all these requirements have been achieved simultaneously in the literature. King[15] employed both plasma-assisted chemical vapour deposition (CVD) and plasma-assisted ALD to grow SiN_x:H films on high-aspect-ratio trenches (Aspect ratio (AR) $\sim$ 1:3.5). While the CVD method showed sidewall roughening, the plasma-assisted ALD process showed a conformal film throughout the trench. Material density, however, was relatively low, which is demonstrated by the low mass density of 2.5 g/cm^3 for the ALD process. Koehler *et al.*[9] reported high SiN_x conformality using a dichloro-silane (DCS) precursor and a NH_3 plasma. These films also suffered from reduced material quality at a substrate temperatures of 400 °C.[9] Another plasma-assisted ALD method that makes use of silicon halides precursors was reported by Ovanesyan *et al.*[8], who recently employed a Si_2Cl_6 precursor in combination with a NH_3 plasma to grown SiN_x films. At relatively low temperatures (350 °C - 450 °C) they were able to deposit SiN_x films showing high conformality (>95%) with a growth per cycle (GPC) of $\sim$ 1.2 Å in trenches with AR $\sim$ 1:4.5. However, a relatively large amount of hydrogen ($\sim$ 23%) was incorporated in the film

and low film density was reported (2.35 g/cm^3). In addition to that, halide containing precursors are not preferred since they can cause the incorporation of chlorines in SiN_x films, which can lead to detrimental effects.[17] Another process by Triyoso *et al.*[2] studied a plasma-assisted ALD process, using a trisilylamine ($N(SiH_3)_3$) precursor and a H_2/N_2 plasma. The plasma-assisted ALD process showed good material quality, as was demonstrated by a low wet-etch rate ($\sim$1 nm/min, 1:100 diluted HF dip) at a deposition temperature of 400 °C. Good conformality was reported, with side/top ratios of $\sim$ 80%. Despite these promising numbers, the aspect ratio was relatively low (AR = 1:2). In previous work conducted in our group, conformality was investigated of SiN_x films deposited with the BTBAS precursor and a N_2 plasma in HARS.[19] Side/top conformality of 90% was achieved in HARS with an aspect ratio of 3 at a plasma pressure of 80 mTorr. Reduced quality was observed after a 3 minute wet etch, but the wet etch-rate was uniform throughout the structure. Evaluating these and other results reported in the literature, it appears that either only high-conformality or high-quality films have been demonstrated in plasma-assisted processes. This has motivated this work, in which systematic experiments were designed in order to identify parameters that govern both film conformality and quality throughout high-aspect-ratio trenches. In order to facilitate this systematic investigation, theoretical results assisted in a proper setup of the experiments and aided the discussion of the results.

5.1.1 Conformality theory

With respect to conformality, Knoops *et al.*[59] identified three specific deposition regimes by performing Monte Carlo simulations of plasma-assisted ALD processes in HARS. In these deposition regimes different mechanisms can be distinguished, which can control thin film conformality. These deposition regimes are depicted schematically in Figure 5.1 and will be discussed first. In order to explain the deposition regimes, it is assumed that precursor dose and plasma dose are sufficient to reach saturation, and subsequent 100% conformality, in the high-aspect-ratio trench. This might seem trivial, but simulations performed by Knoops *et al.*[59] have shown that typically higher precursor doses or longer plasma exposures are required to reach 100% conformality in HARS, compared to the precursor doses and plasma exposures required to obtain saturation on planar substrates. Determining those required precursor doses and plasma exposures for film growth in HARS is not trivial and will, therefore, be discussed separately later in this section.

Deposition regimes

In the reaction-limited regime, depicted in Figure 5.1 **(a)**, the typical reaction time is slow compared to the time it takes for the particles to diffuse throughout the trench. As a result of this, the reactions of the particles with the surface occur at a similar rate throughout the whole trench. In this regime, the conformality should be constant throughout the trench, but saturation is slow (waiting times t_1 and t_2). Saturation occurs after a sufficient waiting time (t_3). In the diffusion-limited regime, depicted in Figure 5.1 **(b)**, the reaction probability of particles at the surface is high. Saturation occurs fast only at the top surfaces in the HARS (waiting time t_1). Due to diffusion of the species, the deposition front moves slowly deeper into the trench over time (waiting

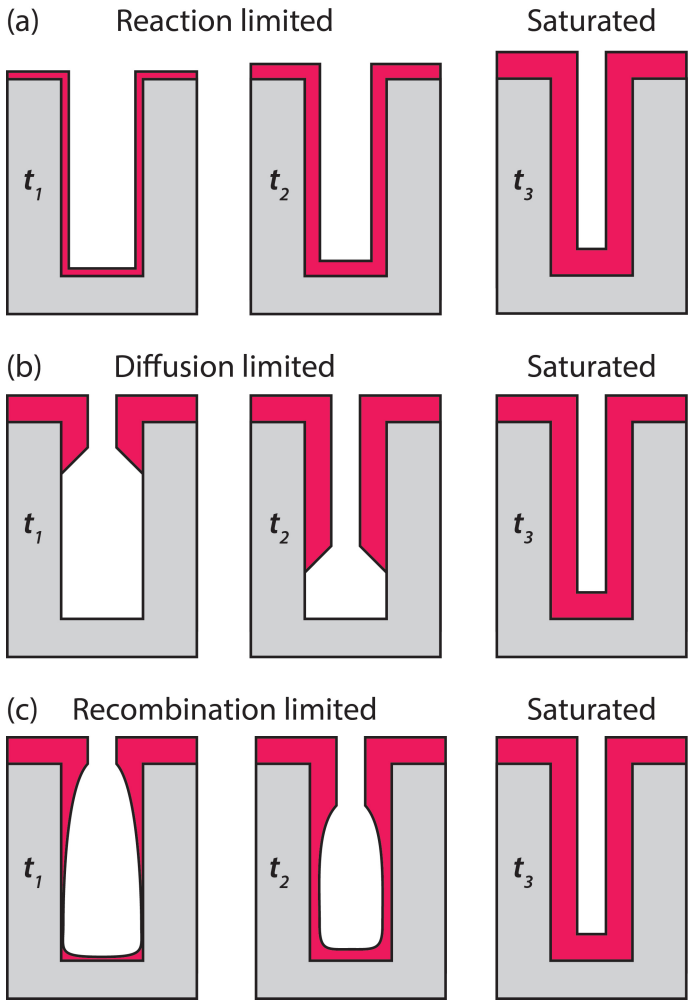

Figure 5.1: Schematic representation of the three deposition regimes that can be distinguished for ALD in high-aspect-ratio structures: (a) reaction-limited regime with growth occurring simultaneously in the entire trench until saturation is reached; (b) diffusion-limited regime in which a downward moving saturation front is observed; and (c) recombination-limited regime in which growth is reduced in the regions deeper in the trench due to surface recombination of radical species. The evolution of the growth over time is indicated from left to right at: t_1 the beginning of the deposition; t_2 the middle of the deposition; and t_3 the end of the deposition.[59]

time t_2), leading to saturation throughout the trench after a sufficient waiting time (t_3), which depends on the aspect ratio (AR). Note that both the reaction-limited and diffusion-limited regime can be caused by limited reactions or diffusion of either the precursor or reactant, or a combination of both.

Both reaction-limited and diffusion-limited regimes can typically be observed in thermal ALD

process and plasma-assisted ALD processes in which the recombination probability of radicals is low. However, in plasma-assisted ALD processes in which the recombination probability of radicals is high, another deposition regime can be distinguished; the recombination-limited regime. In the recombination-limited regime, depicted in Figure 5.1 **(c)**, radicals have a high chance of recombining when colliding with a surface. When this recombination-rate is high, large amounts of radicals will not reach the bottom of the trench, leading to a reduced flux of radicals at certain regions deeper in the trench (waiting times t_1 and t_2). Saturation occurs after a sufficient waiting time (t_3), depending on the flux profile of the radicals throughout the trench. As a result of this, it can take a fairly large waiting time before saturation is observed. In other words, much longer plasma exposure times might be required in order to reach saturation in HARS, compared to the plasma exposure times involved in depositions on planar substrates.

It is, however, not always trivial to distinguish between these deposition regimes and to understand which deposition regimes limit conformality in HARS in a specific process. Reaction-limited, diffusion-limited and radical recombination-limited regimes could all contribute to the film growth in HARS. Which deposition regimes might play a role in the SiN_x process in this work will be discussed later in the Discussion section 5.4.

Reactant doses in HARS

It was already briefly mentioned that determining the required precursor doses and plasma exposures for conformal and saturated film growth in HARS is not trivial. Monte Carlo simulations performed by Knoops *et al.* [59] have shown that typically higher precursor doses or longer plasma exposures are required to reach saturation in HARS, compared to the precursor doses and plasma exposures required to obtain saturation on planar substrates. It will be discussed how these findings can be used to estimate the required precursor dose and plasma exposure time, in order to hypothetically reach saturated film growth in the HARS used in this work. In order to this, the normalised saturation dose is introduced, which is a measure for the increase in dosing that is required to reach saturation in HARS. The normalised saturation dose is normalised on the dose required for reaching saturated film growth on planar substrates.

Precursor dose

Knoops *et al.* [59] have shown how the normalised precursor saturation dose depends on the reaction probability and aspect ratio (AR). This reaction probability is defined as the probability of a precursor molecule to stick to the surface, per collision with that surface. In this work, an AR of ~ 5 applies, but the magnitude of the reaction probability is not known. However, for all possible values of the reaction probability, the Monte Carlo simulations showed that a normalised precursor dose of three is sufficient, compared to the precursor dose required to reach saturation on a planar wafer substrate.

Plasma dose

Knoops *et al.*[59] have shown how the normalised plasma saturation dose, as compared to the required dose for saturation on planar substrates, depends on the recombination rate, aspect ratio (AR) and the reaction probability. In the reactant step of plasma-assisted ALD processes, the reaction probability denotes the probability of a radical to react with the surface. In this work, an AR of ~ 5 applies and a recombination rate of <0.01 (see Appendix H) has been estimated, but the value of the reaction probability is not known. However, for all possible values of the reaction probability, the Monte Carlo simulations showed that a two times higher plasma dose is sure to be sufficient to reach saturation, compared to the plasma dose required to reach saturation on a planar wafer substrate. Even in the *worst-case scenario*, for a recombination rate of 0.1[a], a three times higher plasma exposure time should lead to saturation.

5.2 Experimental setup

5.2.1 ALD reactor

The deposition experiments were carried out using a FlexAL®ALD reactor, which has been developed by Oxford Instruments Plasma Technology. The plasma is produced by a remote inductively-coupled plasma (ICP) source. The plasma RF source operates at a frequency of 13.56 MHz with a maximum input power of 600 W. The set temperature of the substrate table, to which from now on will be referred to as stage temperature, was set at 300 or 500 °C in the experiments. An extra 8" carrier wafer was used to carry the samples into the reactor. Due to poor thermal contacts between the stage table, carrier wafer and sample, the actual sample temperature is lower than the stage temperature. The relation between substrate and stage temperature has been discussed in Chapter 3 and shown in Table 3.1. Briefly summarising, it is estimated that a stage temperature of 300 °C corresponds with a sample temperature of 240 °C and a stage temperature of 500 °C corresponds with a sample temperature of 330 °C. Furthermore, the reactor is equipped with a butterfly valve, with which the pressure in the reactor can be accurately controlled. Other specifics of the reactor have been reported more elaborately in earlier work from our group.[45]

5.2.2 Silicon nitride deposition

SiN_x films have been deposited via a plasma-assisted atomic layer deposition (ALD) process using a Di(Sec-Butyl)AminoSilane (DSBAS) precursor and a N_2 plasma (the MSDS for DSBAS is given in Appendix A). Depositions have been performed on coupons, which contain HARS with aspect ratio 1:4.5. Further information regarding the coupons is explained in the next section 5.2.3 and sample lay-out is given in Appendix C. DSBAS precursor was held at a bubbler temperature of 40 °C and was vapour drawn into the reactor. During this step the butterfly valve was completely

[a]Which is 10 times higher than the expected recombination rate for nitrogen radicals on a SiN_x surface

Table 5.1: Reference process parameters for the DSBAS experiments mentioned in this work.

Parameter	Standard settings
Stage temperature (°C)	500
Precursor dose (ms)	500
Precursor purge (s)	1
Reaction step (s)	3
Plasma exposure (s)	20
Plasma purge (s)	2
Plasma power (W)	600
Plasma pressure (mTorr)	12

closed, in order to confine the precursor in the reactor. The precursor dose time was extended to 500 ms [b], compared to the 100 ms dose in the recipe used in the process development, which is reported in Chapter 4. After this, via a three second soaking step the precursor was granted extra time to react with the surface. During this step the butterfly valve was opened slightly at an angle of 10 ° to prevent the build-up of high pressures in the reactor. This was necessary, because during all steps a continuous 50 sccm flow of inert N_2 gas was introduced into the reactor through the plasma source. This N_2 gas flow prevented the precursor from adsorbing on the surface near the ICP-source in the reactor chamber. After the reaction step the reactor was purged using an nitrogen flow of 50 sccm, while the butterfly valve was completely open at 90 °. A two seconds gas stabilisation flow ensured a stable N_2 gas flow of 100 sccm at a minimum pressure of 12 mTorr (the butterfly valve was completely open now) before the N_2 plasma was ignited. The plasma exposure time was 20 seconds, which is a factor two higher than the standard deposition conditions described in Chapter 4. After the plasma exposure step, the reactor was purged again and the cycle was completed.

Standard deposition parameters are given in Table 5.1 and serve as the reference parameters for the experiments conducted in this work. Moreover, an overview of all experiments conducted in addition to all process parameters is shown in Appendix I. First, the effect of stage temperature on conformality and film quality was investigated by comparing SiN_x films deposited at 300 °C and 500 °C. Furthermore, a comparison between the BTBAS and DSBAS precursor was made, at an increased reactor pressure of 80 mTorr and with an added Ar-flow of 200 sccm during the plasma step. The choice for an increased pressure and flow was based on previous experiments conducted with BTBAS. This also facilitated a comparison between DSBAS films deposited at 12 mTorr and 80 mTorr.

[b] A justification of this factor of 5 was given in section 5.1.1, in which was argued that a factor of 3 was already sufficient in order to reach saturation in HARS (AR $\sim$ 5) trenches

5.2.3 TEM and wet chemical etch rate experiments

SiN_x deposition were performed on high-aspect-ratio (1:4.5) trenches (width ∼100 nm and height ∼450 nm). In order to create these trenches, first a SiO_2 film was deposited on a Si substrate via PECVD. Hereafter, the structures were etched into the Si, such that high-aspect-ratio trenches were obtained. Subsequently, the trenches were coated with a SiN_x layer via high-temperature CVD. Onto these trenches, a SiO_2 layer was deposited using ALD. These coupons containing the trenches have been prepared and provided by LAM research.

A JEOL 2010F ultra-high-resolution scanning TEM at 200 kV was used to obtain cross-sectional images of the trenches with deposited SiN_x films. In order to employ TEM, cross-sectional samples had to be prepared. Therefore, the samples were coated with a layer of spin-on epoxy in order to prevent damage to the SiN_x films during following sample preparation steps. Hereafter, the sample was placed on a sample holder (Cu TEM grid), before it was milled using an energetic ion beam (30 kV, 100 pA) and polished using a less energetic ion beam (5 kV, 40 pA). The TEM studies were conducted by LAM Research.

TEM experiments were conducted both before wet etch-treatment (as-deposited) and after wet etch treatment. For the wet chemical etch-experiments, the samples were dipped into a diluted HF solution (100:1) for 30 seconds.

5.2.4 Analysis procedure

Film conformality was determined by measuring the film thickness at specific positions in the trench. We have assigned four spots in the trench, depicted in Figure 5.2, at which we explicitly determined the thickness in order to compare the conformality for SiN_x films deposited under varying conditions. The percentages referred to in this work are relative to the thickness at the top (position 1) in Figure 5.2. Conformality has been determined as-deposited (as-dep.) and after wet etch (post-WE), to determine the quality of the SiN_x throughout the trench. Furthermore, stage temperature, plasma pressure and precursor have been varied to investigate the effect on conformality and quality.

5.3 Results

An overview of the conformality of the various experiments conducted in this work is given in Table 5.2. The TEM images of the experiments described in Table 5.2 SiN_x films (as-deposited), are shown together in Figure 5.3. The results will be discussed in specific sections, where the effects of varying temperature, precursor (DSBAS and BTBAS) and increased plasma pressure on film conformality and quality are shown. Typically, the conformality is not yet satisfactory, but material quality is high, demonstrating the robustness of the SiN_x films. The differences between the SiN_x films deposited in HARS under various deposition conditions denote that different mechanisms are likely to contribute to both conformality and quality.

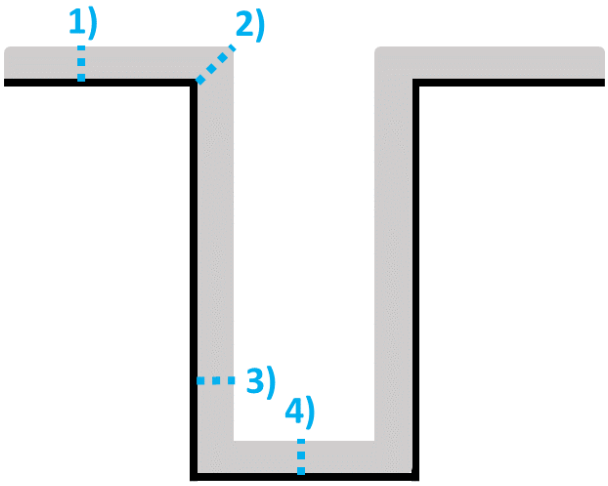

Figure 5.2: Schematic representation of a trench. Four positions are assigned at which film thickness and conformality was determined. Percentages are calculated relative to the thickness at the top surface; position 1). Position 2) is referred to as side-near-top, position 3) is referred to as side-near-bottom and position 4) is referred to as bottom.

Table 5.2: Conformality for SiN_x films deposited by DSBAS, while varying temperature and pressure. TEM was used to image the trenches and conformality, both as-deposited (As-dep.) and after a wet-etch (Post-WE). The typical uncertainty in the numbers is given in the second row.

Precursor	DSBAS						BTBAS[a]	
Temp (°C)	300		500		500		500	
Conditions	Standard 12 mTorr		Standard 12 mTorr 200 sccm Ar		High pressure 80 mTorr 200 sccm Ar		High pressure 80 mTorr	
Position	As-dep. (%)	Post-WE (%)	As-dep. (%)	Post-WE (%)	As-dep. (%)	Post-WE (%)	As-dep. (%)	Post-WE (%)
Top	*100*	*100*	*100*	*100*	*100*	*100*	*100*	*100*
Side-near-top	89 +/- 5	92	85	90	97	97	90	90
Side-near-bottom	55	29	43	36	49	36	31	26
Bottom	65	62	56	56	61	59	50	54

[a] This experiment was conducted before the upgrade of the substrate table in the FlexAL® reactor. As discussed previously in section 3.1.2, the upgrade seems to have resulted in a slightly increased heat conduction and subsequently sample temperature. As a result, this stage temperature could be significantly lower (a very rough estimate: $\sim$ 50 °C) compared to the other experiments conducted at a stage temperature of 500 °C in this Table.

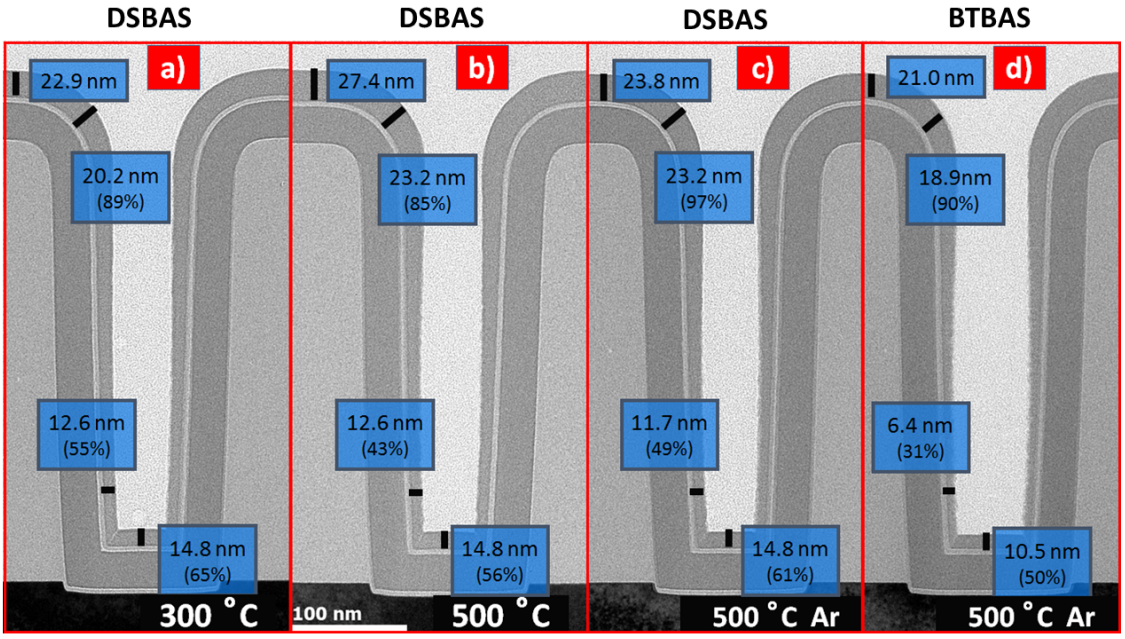

Figure 5.3: TEM image of a SiN_x film deposited at different stage temperatures (300 or 500 °C) deposited by **a)** a DSBAS precursor, at 300 °C, **b)** at 500 °C and **c)** at 500 °C with an extra Argon flow of 200 sccm at 80 mTorr pressure during the plasma step. Figure **d)** shows a TEM image of a SiN_x film deposited at a stage temperature of 500 °C deposited by a BTBAS precursor with an extra Argon flow of 200 sccm and at 80 mTorr pressure during the plasma step.

5.3.1 Temperature variation

TEM images have been obtained of SiN_x films deposited at stage temperatures of 300 °C, depicted in Figure 5.3 **a)**, and 500 °C, depicted in Figure 5.3 **b)**. It can be observed from the TEM images and conformality of the films, that the film deposited at 300 °C shows slightly better conformality at bottom (65%) and side-near-bottom (55%) positions in the trench, compared to the film deposited at 500 °C (56% bottom, 43% side-near-bottom).

Film quality of the SiN_x films is determined by conducting wet chemical etch-experiments on the trench-structures. In order to compare the quality, TEM images have been obtained of SiN_x films as-deposited, depicted in Figure 5.4 **a)** and after being dipped in a diluted HF solution for 30 seconds, which is depicted in Figure 5.4 **b)** for the film deposited at 500 °C.

In the Figure 5.4, it can be observed that the wet etch-rates at the top, bottom, and side-near-top positions, are not significant. This high quality was also confirmed for the film deposited at 300 °C (data not shown), also showing no significant wet etch-rates at top, bottom and side-near-top positions. For the film deposited at 500 °C, it can be further observed that the thickness at the side-near-bottom position decreased slightly as a result of the 30 seconds wet-etch. This is demonstrated by a wet-etch rate of $\sim$ 4 nm/min (+/- 3 nm/min) at the side-near-bottom position. For the film deposited at 300 °C the quality at the side-near-bottom position was worse, corresponding to

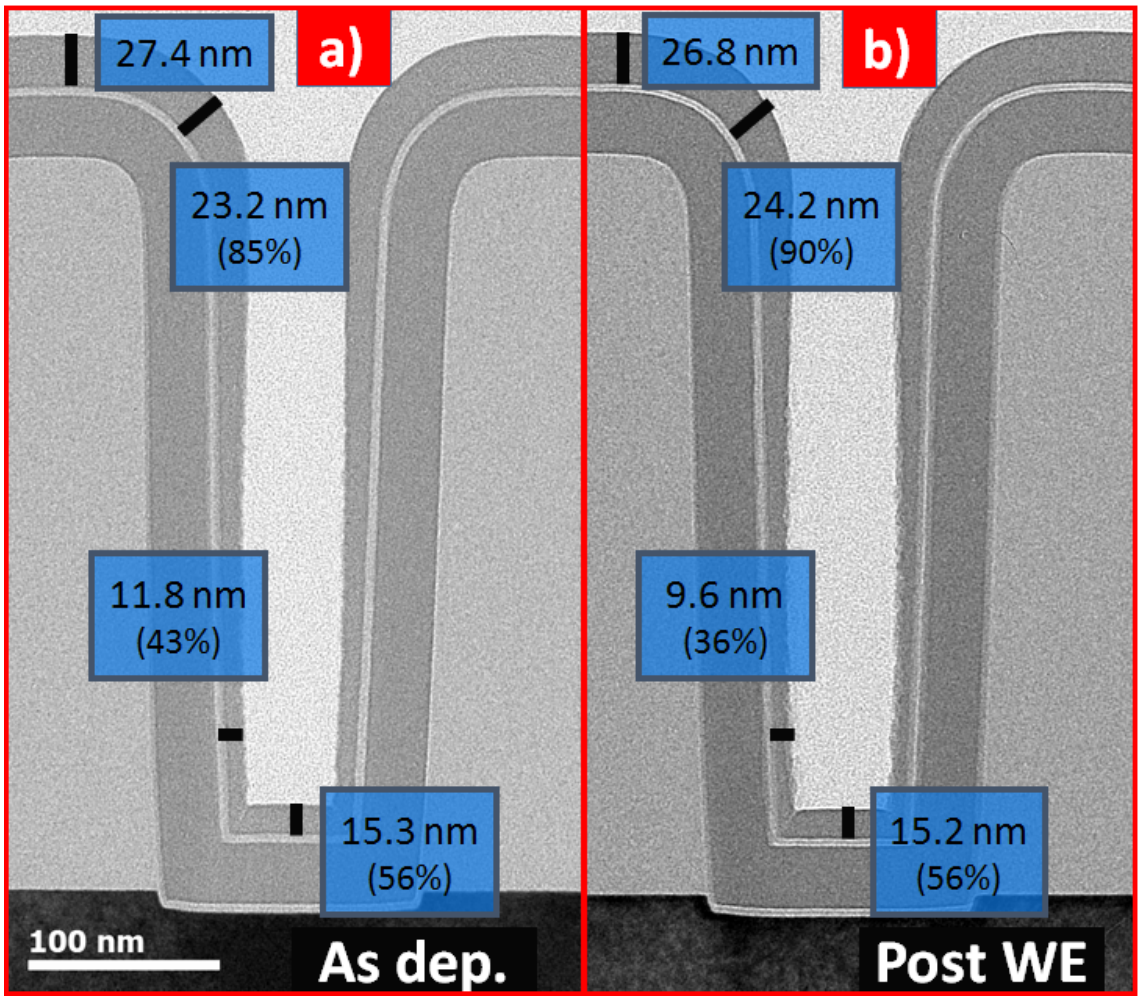

Figure 5.4: TEM image of a SiN_x film deposited at a stage temperature of 500 °C using a DSBAS precursor, as deposited **a)** and post wet-etch **b)**

a wet-etch rate of $\sim$ 12 nm/min (+/- 3 nm/min). This indicates that film quality is reduced at the side positions, or the vertical surfaces, near the bottom of the trench.

5.3.2 DSBAS vs. BTBAS

SiN_x films have been deposited by DSBAS, depicted in Figure 5.3 **c)**, and by BTBAS, depicted in Figure 5.3 **d)**. It can be observed that the film deposited by DSBAS shows slightly better conformality overall, compared to the film deposited by BTBAS. DSBAS conformality at the bottom is still not satisfactory, with conformalities of 49% at the side-bottom position and 61% at the bottom position.

The wet etch-rate of both the DSBAS and BTBAS films showed no significant etch at top, bottom

and side-near-top positions in the trench. For DSBAS, at the side-near-bottom position, however, a wet etch-rate of 7 nm/min (+/- 3 nm/min) showed reduced film quality. For BTBAS, a reduced wet etch-rate of 3 nm/min (+/- 3 nm/min) is obtained at the side-near-bottom position, which is only just significant. These results indicate that at the side-near-bottom position, BTBAS might show slightly better film quality than the DSBAS film quality, at increased plasma pressure.

5.3.3 Increased plasma pressure

SiN_x films have been deposited by DSBAS at a reactor pressure of 12 mTorr, depicted in Figure 5.3 **b)**, and at a reactor pressure of 80 mTorr during the plasma step, depicted in Figure 5.3 **c)**. Note that an extra flow of 200 sccm of Argon was added to facilitate the increase in reactor pressure, while keeping the residence time[c] low. The low residence time reduces redeposition of ligand fragments and film quality. It can be observed that the film deposited at 80 mTorr shows slightly better conformality at the side (vertical) positions compared to the 12 mTorr film. The differences in conformality are however small, with ~ 5 (absolute) percentage points difference in conformality between the two samples, at both the side-near-top and side-near-bottom positions.

The wet etch-rate of both the DSBAS films showed no significant etch at the top positions (both top, as side-near-top) and bottom position in the trench. At the side-near-bottom positions, both films showed significant wet etch-rates and subsequent reduced film quality. The 12 mTorr sample showed a wet etch-rate of 4 nm/min (+/- 3 nm/min) and the 80 mTorr sample a wet etch-rate of 7 nm/min (+/- 3 nm/min).

5.4 Discussion

Before discussing the results it has to be noted that, in this work, it is assumed that GPC in the trenches showed saturation in precursor dose time and plasma exposure time. The validity of this assumption was made plausible, by referring to Monte Carlo simulations, with which it was shown that saturated film growth in trenches with AR ~ 5 could be expected with the precursor and plasma doses used. However, preliminary results showed that the GPC increased significantly when not only the plasma exposure time was extended further, but also the precursor dose time was extended. The effect of increasing precursor dose and plasma exposure time has been systematically investigated, of which the parameters are shown in Appendix I. The results, however, arrived too late in order to be implemented in this thesis.

5.4.1 Film quality and conformality

The films deposited in high aspect ratio structures (1:4.5) by DSBAS in this work were of high-quality, as was visualised by the typically low wet-etch rates. In all shown samples no significant wet etch-rate was detected at the horizontal surfaces in the trench, both on the top as on the bottom

[c]Residence time is briefly explained in Appendix B.

of the HARS. However, typically reduced film quality was observed at the vertical side-walls in the bottom (side-near-bottom) of the trench. The quality reduced significantly at decreased stage temperatures, from 4 nm/min (500 °C) to 12 nm/min (500 °C). This is in line with the results obtained in Chapter 4, which show decreased material quality at reduced stage temperatures. Furthermore, the BTBAS film quality at the side-near-bottom position might show slightly higher film quality compared to the DSBAS film. This was somewhat surprising, considering the results discussed in Chapter 4, which generally show higher DSBAS SiN_x film quality. Furthermore, the 12 mTorr sample showed slightly higher material quality at the side-near-bottom position compared to the 80 mTorr sample. These differences could suggest that the ions play a role in the film growth in HARS, which will be discussed later in a specific section in this discussion.

Simultaneously obtaining highly conformal films showing high quality throughout a HARS is not trivial, as is also typically reported in the literature. The results in this work showed the complexity of achieving this, which was visualised by typically low conformality values of $\sim$ 50% at the bottom and side-near-bottom positions in the trench. Overall, the conformality varied only slightly as a result of the varied deposition parameters. The results show that an increase in stage temperature results in an increase of $\sim$ 10% at the bottom and side-near-bottom positions. Furthermore, the DSBAS conformality was slightly better compared to the conformality obtained with BTBAS. Further observing the results, it seems that an increase in plasma pressure resulted in a slightly improved conformality. This observation could also suggest that ions play a role, which will be discussed later in a specific section in this discussion.

Furthermore in this discussion section, it will be discussed what could explain the observed poor conformality and observed differences in material quality. First it will be discussed whether the previously mentioned deposition regimes apply on the films grown by the process employed in this work. Hereafter, it will be discussed how the soft saturation of the GPC as function of the plasma exposure time could limit conformal film growth in HARS. Furthermore, it will be discussed whether the ions are likely to play a role in the SiN_x film growth in HARS.

5.4.2 Deposition regimes

It was previously mentioned that both the reaction-limited regime and diffusion-limited regime can be caused by limited reactions or diffusion of either the precursor or reactant, or a combination of both. To organise the discussion, first the reaction-limited and diffusion-limited regime will be discussed for the precursor adsorption. Secondly, the reaction-limited, diffusion-limited and recombination-limited regimes will be discussed for the plasma step.

Precursor deposition regimes

The first regime that was considered, was the reaction-limited regime. The fast saturation in precursor dose time, as reported in Chapter 4, suggests that the precursor occupies the available reactive sites readily. This could indicate that the reactions occur relatively fast. However, preliminary Density Functional Theory (DFT) results have shown that typically high activation energies need

to be overcome and consequently longer reaction times apply, in order for the precursor adsorption reaction to fully complete. Combined with the preliminary additional conformality results, which showed an increase in GPC at an extended precursor dose, it cannot be excluded that the precursor reactions limit conformal SiN_x film growth. The second regime that was considered, was the diffusion-limited regime. When observing the typical profile of the diffusion-limited regime (as shown in Figure 5.1) it can be seen that it does not correspond to the profiles we obtained. In the profiles observed in the TEM images, the thickness at the vertical side-wall reduced gradually as a function of the depth in the trench. A typical diffusion-limited profile would show a more abrupt thickness reduction. This would suggest that precursor diffusion is not limiting the SiN_x film growth.

Plasma deposition regimes

For the plasma step, a discussion about the typical profiles is more complex. A complication follows from the soft saturation of the GPC as a function of plasma exposure time, as already discussed in Chapter 4. Another complication results from the different reactive species present in a plasma, which could all contribute to film growth in specific ways. Later in this discussion, the impact of the soft saturation of the GPC as a function of plasma exposure will be discussed, in addition to a discussion about the possible role of other specific plasma species, such as ions. As a result of these complications, it is difficult to generally consider the reaction-limited and diffusion-limited regime for the plasma. As a result, soft saturation and the role of ions will be discussed separately.

The third radical recombination-regime, however, can be considered explicitly, since it specifically considers interactions of the nitrogen radicals with the surface. It was shown by Profijt *et al.* [60] how surface chemistry, for low pressure conditions, is typically ruled by interaction of plasma radicals with the surface. In other words, it is important that the radicals reach the whole surface, including the regions deep inside the trench, so they can contribute to conformal SiN_x film growth. Whether radicals do reach all the regions deep inside the trench, depends on the recombination rate of radicals with the SiN_x material on the trench side-walls. For radicals interacting with a SiN_x surface, it is estimated the surface loss probability is relatively low < 0.01 (see Appendix H). This would indicate radical recombination does not limit SiN_x film growth in HARS. However, since the typical conformality profile matches the simulated profile of a recombination-limited regime relatively good, it cannot be completely excluded that radical recombination limits conformality. Furthermore, it is not known how many collisions radicals typically have to undergo in order to reach regions near the bottom of the trench. So, concluding, despite the low recombination rate (< 0.01), radical recombination could still play a role in the SiN_x film growth.

5.4.3 Soft saturation

As discussed previously, an extra complication follows from the soft saturation of the GPC as a function of plasma exposure time, as discussed in Chapter 4 and depicted in Figure 5.5. In the

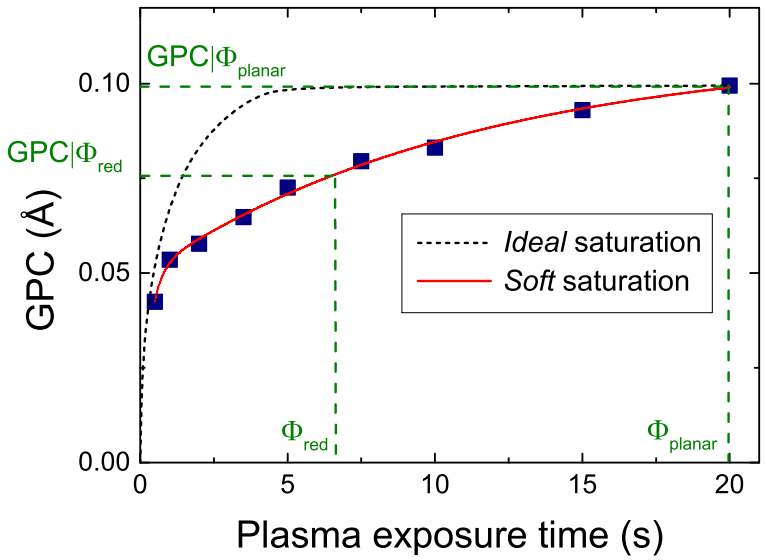

Figure 5.5: GPC as a function of plasma exposure time. The green dashed lines indicate that a reduced flux Φ_{red} (factor 3[a]) compared to the flux required to reach saturation on planar substrates is expected Φ_{planar}, in AR $\sim$ 5 structures. It can be seen how this leads to a reduced GPC$|\Phi_{red}$, compared to the GPC on planar substrates Φ_{planar}, due to the soft saturation of the GPC. The black dashed line shows how ideal saturation would give the same GPC at a reduced plasma exposure times, almost independent of the flux of reactive plasma species.
[a] It was shown in section 5.1.1, that even in the *worst-case scenario*, a three times higher plasma exposure time should lead to saturation in AR = 5 trenches.

determination of the normalised saturation doses, we referred to the dose required for saturation on planar substrates. The simulations assume that film growth was in *ideal* saturation instead of in soft saturation, which are both depicted in Figure 5.5. In the *ideal* saturation case, it can be observed that an increase in plasma exposure time has no effect on GPC. In soft saturation, it can be seen that an increase in plasma exposure time leads to a significant increase in GPC. Therefore, this soft saturation could have caused differences in thickness and even material quality, throughout the trench. In this section, we will try to estimate the maximum difference in thickness we could expect (in the *worst case-scenario*) as a result of the soft saturation of the GPC.

Based on the saturation curve and the normalised plasma exposure time it is possible to estimate a maximum difference in thickness throughout the trench. As was discussed in section 5.3.2, it can be expected that a normalised plasma dose of 3 should always be sufficient to reach saturation in AR=5 trenches[d], compared to the plasma exposure time required for saturation on a planar wafer. Since the flux of plasma species at the top horizontal surface of the trench does not differ from the planar substrate case, the increase in plasma exposure is required to expose certain position deep in the trench to a sufficient flux of species. Assuming plasma exposure time scales with the flux of plasma species, it can be concluded that all regions in the trench are exposed to at least 1/3rd of the flux that reaches the top of the trench. Based on the saturation curve, depicted in Figure 5.5, this factor 3 difference in plasma exposure time can be used to estimate the maximum difference in GPC that can be expected. Since the plasma exposure time used in the conformality experiments is 20 s, it is argued that some regions in the trench are exposed to only 1/3rd of the plasma exposure, so effectively a 6.7 s plasma exposure. Using this reasoning for a plasma exposure time of 20 seconds we used in our experiments, a difference in GPC ($\mathrm{GPC}|\Phi_{red} \sim 0.75\Phi_{planar}$) and consequently 75% thickness difference is expected, as depicted in Figure 5.5. This would be the maximum conformality difference that can be expected, considering the *worst-case scenario* assumptions that were made.

So based on the soft saturation behaviour, a maximum difference in conformality throughout the trench of $\sim$ 75% is expected. The experiments in this work showed differences of 50 %. As a result, it is likely that more factors play a role in the determination of the conformality in trenches. A solution for the soft saturation could be to extend the plasma time even further to a regime where the soft saturation-effect reduces, or even disappears. We can only speculate that this happens at longer plasma exposure times ($>$ 20 seconds). Further exploration of the saturation behaviour at larger plasma exposure times is, therefore, required. It has to be noted that extending the plasma exposure times to $>$ 20 seconds, would significantly increase the cycle time. Note that the different properties of the various species present in the plasma is neglected in this reasoning. The specific properties of the ions are not taken into account and need to be investigated specifically, since the results suggested that the ions might play a role in the SiN_x film growth.

[d] assuming a recombination rate of 0.1 (which is deliberately 10 times higher than the expected recombination rate of < 0.01)

5.4.4 The role of ions

Generally, the results in this work show thinner films at the side-bottom compared to the bottom position, which could indicate the ions play a role. It has been suggested by King [15] that N_2^+ ion bombardment plays an important role in the desorption of surface hydrogen and the creation of reactive bonding sites for atomic N species as well. The species in a plasma consists of various reactive species, e.g. N_2^+ ions and radicals, which could potentially all contribute to film growth in specific ways. Identifying the exact role of all those species individually is not trivial. Nonetheless, the role of the ions can be identified more readily compared to the role of the radicals, as a result of the anisotropy of the ions. This anisotropy is a result of the plasma sheath, which selectively accelerates the positively charged ions to the surface. When the gas pressure is relatively low, the mean free path of the ions is higher than the thickness of the plasma sheath (typically $\sim$ 1 mm), resulting in ions with a fair amount of energy (typically $<$ 15 eV[e]) that hit the surface perpendicularly. [12,60] Therefore, the ion flux at the trench (vertical) sidewall is small, compared to the ion flux at the horizontal surfaces (both top as bottom of the trench). King [15] even attributed the different growth rates they observed between the horizontal and vertical surfaces in trenches to the different N_2^+ ion fluxes at those surfaces, which they investigated for their plasma-assisted ALD process for growing SiN_x films. Using this argumentation, thickness and/or quality differences between horizontal and vertical surfaces could indicate that ions play a role in the growth of SiN_x films.

The results obtained in this work confirm that conformality is slightly improved when the pressure is increased to 80 mTorr, especially on the vertical surfaces (side-near-top and side-near-bottom). The quality at the side-near-bottom position however, is also reduced (12 nm/min for 80 mTorr, 4 nm/min for 12 mTorr). The increase in plasma pressure reduces the mean free path of the ions, and subsequently their energy and flux. The average ion energy is expected to drop significantly (with $\sim$ 5 eV[f]. [12,60]) when increasing the plasma pressure to 80 mTorr. Furthermore, Profijt *et al.* [12] showed that the ion flux dropped with a factor of 10 for oxygen radicals after a pressure increase from 12 to 80 mTorr. So considering both the reduced ion flux and reduced average ion energy, the results could indicate that the less energetic and simply fewer ions play a role in the determination of the quality of the SiN_x film. This is in line with King [15], who suggested that $N_2{}^+$ ion bombardment helps to desorb surface hydrogen and create reactive sites. Therefore, a decrease in GPC can be expected, which was also observed in this work by measuring the GPC on planar substrates (see Appendix I for descriptions of all experiments and their GPCs). The increase in plasma pressure led to a small decrease in GPC from 0.15 Å to 0.13 Å on the planar substrates.

Although these observations support that the ions might play a role in SiN_x film growth, the results cannot prove this yet. A way to prove that ions play a role is by biasing the substrate during SiN_x

[e] Profijt *et al.* [60] showed that oxygen ions have an ion energy of 15.3 eV, using a plasma source of 500 W and a pressure of 10 mTorr. Furthermore, they showed that increasing the plasma power decreases the ion energy, which we use in the estimation (since we use 600 W). They also showed that nitrogen ions have a slightly smaller average energy than oxygen ions. All summed up, this leads to an estimated average nitrogen ion energy of $<$ 15 eV

[f] Profijt *et al.* [60] showed that increasing the plasma pressure from 10 to 100 mTorr led to an decrease in average ion energy from 15.3 to 10.8 eV, for oxygen ions. A roughly similar decrease in average ion energy is assumed for nitrogen ions

film deposition. With a biased substrate, the ions can be selectively accelerated, increasing only their average energy. A first series of such experiments has already been conducted, however, results arrived too late for implementation in this thesis.

5.5 Conclusion

We have investigated the conformality and quality of SiN_x thin films deposited using a N_2 plasma-assisted ALD process by both a DSBAS precursor and BTBAS precursor. High quality films were deposited, showing no significant wet etch-rate on the top surface of the HARS ($\sim$ 1:4.5). For DSBAS, the wet etch-rate on the horizontal surface on the bottom of the high-aspect-ratio trench was also not significant. Typically reduced film thickness was observed at the bottom (55-65%) and at the side-near-bottom (40-55%). The soft saturation of the GPC as function of the plasma exposure time, and subsequently the reduced flux of reactive plasma species, probably also caused differences in conformality. The observed differences in thickness, however, could not be explained by only considering the soft saturation of the plasma exposure time. The reduced quality on the vertical side walls of the trench might indicate that the ions play a role in determining the quality of the film. The variation of the pressure during the plasma step from 12 to 80 mTorr led to a reduction of the film quality, which was demonstrated by the wet etch-rates (12 nm/min for 80 mTorr, 4 nm/min for 12 mTorr). These differences indicate that the ions might play a role in SiN_x film growth, but further experiments are required to prove this.

Chapter 6

Aspects regarding the deposition mechanism

Throughout this thesis, some aspects regarding the deposition mechanism of DSBAS have been discussed. In this chapter, these findings regarding the deposition mechanism of DSBAS will be summarised and discussed in more detail. In order to do this, insights regarding the deposition mechanism of BTBAS will be presented and discussed as well. BTBAS has been investigated in detail in our group PMP and comparisons between BTBAS and DSBAS could help identifying important properties regarding the reaction mechanisms of aminosilane precursors in general. In addition to experimental results, findings obtained via density function theory (DFT) simulations are used to discuss the reaction mechanism in more detail. This section will be concluded by some speculative ideas regarding the reaction mechanism of DSBAS.

6.1 Mechanisms controlling saturation

As has been explained in the Introduction Chapter, ALD revolves around the iteration of two half-cycles, which are both self-limiting. It is important that the reactions which occur in these half-cycles are self-limiting, since this facilitates the controlled growth, with respect to both film quality as film thickness. In addition to that, it was discussed that when plasmas are involved in aminosilane processes, long plasma exposures can be required in order to reduce redeposition of ligand fragments. Saturated half-reactions are, therefore, one of the foundations for the plasma-assisted ALD of aminosilane precursors. It has been shown by Puurunen[58] that saturation behaviour is caused by two factors: steric hindrance of the ligands and the number of reactive surface sites. First the mechanisms occurring in the precursor half-cycle will be discussed, before discussing the mechanisms in the plasma half-cycle. There will be a special focus on steric hindrance and reactive surface sites during both half-cycles, since they cause saturation of the half-cycles.

6.1.1 Precursor half-cycle

BTBAS precursor adsorption and ligand removal

In the beginning of the precursor half-cycle, the surface ideally consists of only reactive surface sites, which have been created by the plasma in the previous half-cycle. These reactive surface sites are required for the precursor molecules to adsorb on during the precursor half-cycle. A precursor adsorption mechanism for BTBAS has been proposed by Braeken *et al.* [18], which is depicted in Figure 6.1.

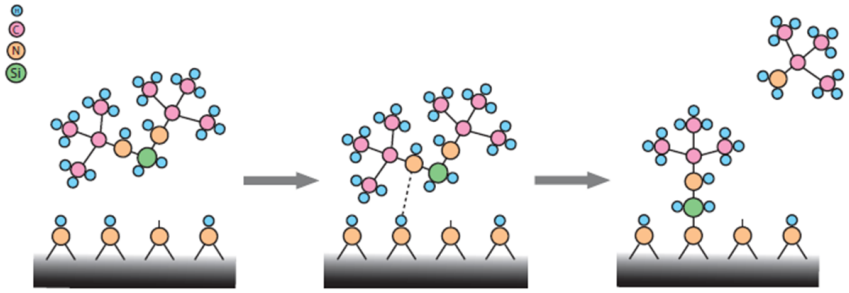

Figure 6.1: Schematic representation of the proposed reaction mechanism of BTBAS adsorbing on a surface which can consist of NH, dangling nitrogen bonds and other reactive surface sites. In the middle image, the transition state, the reaction in which the surface hydrogen is transferred to one of the BTBAS ligands is ongoing. In the right image, the hydrogen transfer is complete and the ligand splits off completely. The image is obtained from Braeken *et al.* [18]

In this schematic representation it is visualised how one of the ligands splits off, upon the transfer of an hydrogen atom from surface group, which has been proposed by Murray *et al.* [17]. However, only one of the ligands splits off, the other still remains bonded to the silicon and consequently the surface. The split-off of this second ligand is proposed to occur via a second hydrogen exchange reaction with a reactive site at the surface.[61] These results, however, were proposed based on DFT simulations. Experimental studies have shown that not all ligands were already removed in the precursor half-cycle.[18,20,21] It was shown experimentally that reaction products of the BTBAS-ligand were present in the plasma half-cycle as well, indicating they were removed by the plasma in the subsequent plasma half-cycle. This proves that, in a significant number of cases, at least one of the BTBAS-ligands remains bonded to the silicon on the surface in the precursor half-cycle. A consequence of this is that other neighbouring reactive sites can be blocked as a result of steric hindrance, which could limit the film growth. Steric hindrance will be discussed further in this

paragraph.

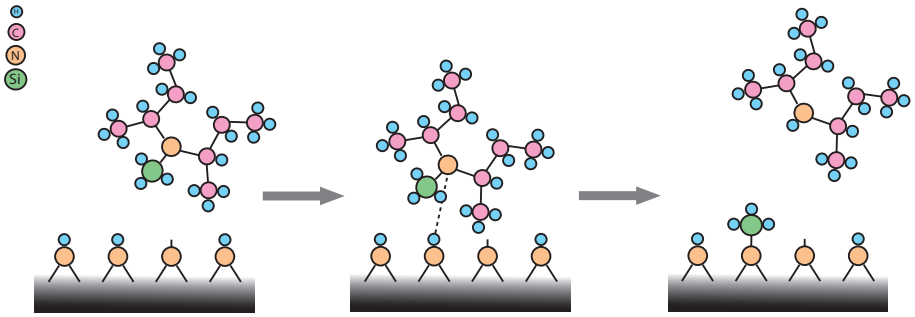

Figure 6.2: Schematic representation of the proposed reaction mechanism of DSBAS adsorbing on a surface consisting of NH and dangling nitrogen bonds. In the middle image, the transition state, the reaction in which the surface hydrogen in transferred to the DSBAS ligand is ongoing. In the right image, the hydrogen transfer is complete and the ligand splits off completely.

Proposed DSBAS precursor adsorption and ligand removal

For DSBAS, we propose a similar reaction mechanism, which is depicted in Figure 6.2. In the schematic representation it is visualised how the complete ligand splits off, while transferring a hydrogen atom from a surface-group to the ligand. This would result in a SiH_3-group bonded to the surface, without any remaining ligands attached. Where experimental studies supported the earlier mentioned BTBAS mechanism, experimental support for this mechanism is not yet available for the DSBAS process. However, the typically low carbon contents observed in the SiN_x films deposited by DSBAS in this work, supports the hypothesised reaction mechanism for DSBAS. These low carbon contents imply a reduced redeposition as a result of a reduced amount of remaining precursor ligands. For this reduction in redeposition to happen though, the vast majority of the reactions in which the DSBAS ligand splits off should be completed in the precursor half-cycle. In order to investigate this, DFT studies have been employed to investigate the kinetics involved in this precursor binding and ligand split-off.

DSBAS and BTBAS reaction kinetics

Preliminary DFT results in our group have shown that the split-off of a ligand is energetically favourable, indicating that the proposed ligand split-off reactions involved in both DSBAS and BTBAS adsorption are likely to occur. Furthermore, the preliminary DFT results have shown that both precursors typically show high activation energies ($\sim$1.9 eV for DSBAS, $\sim$1.4 eV for the first ligand of BTBAS and $\sim$1.6-1.8 eV for the second ligand of BTBAS) that need to be overcome simultaneously. These high activation energies indicate that at low substrate temperatures, it could take a long time for the reaction to complete. In other words, it is possible the reaction remains in a transition state, depicted in Figure 6.3 for DSBAS. In this figure, it can be seen how the

silicon has bonded to the surface nitrogen, but the hydrogen transfer from surface group to ligand has not completed yet. It is important to realise that for BTBAS, this activation energy needs to be overcome twice, since two ligands have to split off. Since, for BTBAS, experimental results showed that ligand reaction products were present in the plasma half-cycle, it can be assumed that these activation energies were not overcome twice, i.e. both ligands split off, in the precursor half-cycle.

However, the clearly sub-monolayer GPCs obtained for both BTBAS and DSBAS suggest that either the number of reactive surface sites or steric hindrance is limiting the film growth. Steric hindrance will be discussed in the following paragraph, while the reactive sites will be discussed in the next section about the plasma half-cycle.

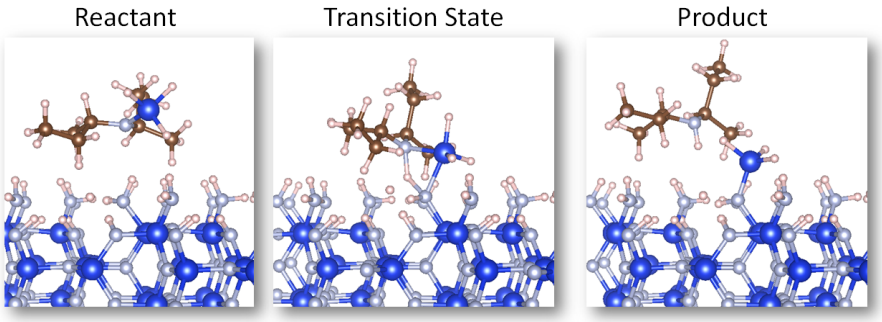

Figure 6.3: Schematic representation of the modelled reaction kinetics of DSBAS adsorbing on a surface consisting of NH_2 bonds.

Steric Hindrance

Steric hindrance occurs when reactive adsorption sites are blocked by ligands, effectively making those reactive surface sites unavailable for other precursor molecules to bond on. By comparing the size of the precursor molecules with the experimentally obtained silicon surface densities, it has been investigated whether steric hindrance could limit the SiN_x precursor adsorption, and consequently film growth.

Both the DSBAS- and BTBAS-molecule are relatively large, which can be approximated as spheres with radii of $\sim$ 5 Å. This would indicate at least 1 DSBAS or BTBAS molecule would fit on a square nanometre. Comparing this with typical silicon atom growth rates obtained in this work ($\sim$ 0.5 [Si] at. /cycle/nm^2), it is likely that steric hindrance is likely to not be the limiting factor in this process. If steric hindrance would be the limiting factor, the growth rate would be expected to be at least 1 [Si] at./cycle/nm^2[a]. However, putting this into perspective could help in determining the potential impact of steric hindrance on film growth. In other words, relating this rough maximum in [Si]-film growth to actual [Si]-densities in typical SiN_x films obtained for DSBAS in this work, can show the fraction of a monolayer that can be grown with this precursor.

[a] and can reach up to 1.5 [Si] at./cycle/nm^2

In order to make this comparison, the maximum silicon density was estimated by using the crystal structure of β-Si_3N_4[b]. Using this strategy, it can be shown that stoichiometric Si_3N_4 contains ~ 4 [Si] atoms per nm^2. Comparing this with typical silicon atom growth rates obtained in this work (~ 0.4 [Si] at. /cycle/nm^2), it can be seen that ~ 10 cycles would be required to fully cover this square nanometre with silicon atoms. In other words, in terms of [Si] atoms, every cycle roughly 10% of a monolayer is deposited. If steric hindrance would be the limiting factor, it was shown that the growth rate would be expected to be $\sim$ 1-1.5 [Si] at./cycle/nm^2. Even in this case of maximum growth, $\sim$ 3-4 cycles would be required to grow a monolayer of stoichiometric Si_3N_4. However, in this reasoning, it is assumed steric hindrance occurs during the whole precursor half-cycle. In other words, it is assumed that a ligand blocks the surrounding reactive adsorption surface sites during the entire precursor half-cycle.

For DSBAS, steric hindrance would only be an important factor when the reactions involved are relatively slow. The high activation energies discussed before, indicate the reaction is indeed relatively slow in case of low stage temperatures. In those cases, the DSBAS ligand could block reactive sites during the whole precursor half-cycle. Moreover, in cases that a lot of surface reactions are incomplete (see transition state in Figure 6.3), those ligands would even remain at the surface. In those cases, the ligand will be removed during the subsequent plasma step, eventually leading to redeposition. Redeposition will be discussed in the next section, where the plasma half-cycle will be discussed. Fast reactions at higher stage temperatures, however, would result in a more rapid ligand split-off. In those cases, neighbouring reactive surface sites would become available again for a new precursor molecule to bond on rapidly, in the same precursor half-cycle. The typically low carbon contents, especially at higher stage temperatures ($> 200\,^{\circ}C$), suggest that the vast majority of ligands has split off completely for DSBAS already in the precursor half-cycle. In the hypothetical case that ligand split-off would occur infinitely rapidly, the number of reactive sites would indisputably become the limiting factor in the SiN_x film growth. Since it is likely steric hindrance is not the limiting factor in SiN_x film growth, as discussed before, the identification and creation of reactive sites will be discussed in the next section.

6.1.2 Plasma half-cycle

The reactive sites to which the silicon precursor can bind are created by the nitrogen plasma. In this section an attempt will be made to identify the reactive surface sites and it will be discussed how those reactive sites are created by the plasma. Furthermore, it will be shown how redeposition of ligand fragments can cause contaminations to be incorporated in the SiN_x film.

Identification of reactive/surface sites

Experimentally identifying which surface groups can be considered as reactive sites in plasma-assisted ALD processes in general is not trivial. Ande *et al.*[55] recently showed how BTBAS adsorbs readily on under-coordinated nitrogen on the surface. This was also suggested by Huang

[b] Hexagonal structure (space group 176), using lattice constants of a = 7.63 Å and b = 2.91 Å

and Han[61] and Murray *et al.*[17]. Preliminary results obtained via DFT simulations have shown similar results for DSBAS, i.e. under-coordinated nitrogen-atoms can be considered as reactive sites for DSBAS as well. Identifying which surface group can be considered as the main reactive site is however hard. Cornelissen[20] showed experimentally that NH molecules were incorporated in the SiN_x films deposited by BTBAS, via Fourier transform infrared spectroscopy (FTIR) of the film. It is, however, complex to draw conclusions from such experimental results. Since hydrogen at the surface is rather mobile, hydrogen could be easily transferred from neighbouring surface sites to the precursor. As a result, when the precursor adsorbs to the surface, the hydrogen does not necessarily have to originate from the same reactive adsorption site. Considering the mobility of the hydrogen it is, therefore, not easy to identify which surface sites are the main reactive surface sites for the aminosilane precursor to bind to.

Perrine and Teplyakov[62] proposed that NH_x (with x=0,1,2) surface groups changed in reactivity as a function of temperature. As the temperature increases, Perrine and Teplyakov[62] suggested that the reactive surface sites changed from NH_2 to NH groups. These findings seem to correspond with the results in this work (described in Chapter 4), which showed that the hydrogen content in the SiN_x films decreased as a function of increasing surface temperature. Furthermore, based on the simulations by Perrine and Teplyakov[62], the change in reactivity of the NH_x surface groups is expected to lead to an increase in the number of adsorbed silicon atoms per nm^2 per cycle (GPC [Si][c]) as a function of increasing temperature. Studying the GPC [Si] as a function of stage temperature ((see Chapter 4, Figure 4.3)), different behaviour is observed in this work. For DSBAS films, GPC [Si] is rather constant as a function of increasing temperature, BTBAS films even showed a monotonic decrease in GPC [Si]. This indicates other growth mechanisms need to considered for contributing in the creation of reactive sites.

Creation of reactive/surface sites

The reactive surface sites are created during the plasma exposure step. Reactive plasma species interact with the surface hydrogen (SiH_3, resulting from the precursor adsorption) in order to supposedly create NH_x (with x=0,1,2) surface groups, which was made plausible in the previous paragraph. Previously, it has been shown in Figure 4.2 and discussed in Chapter 4 how the GPC showed only soft saturation as function of plasma exposure time. This indicates that separate mechanisms are responsible for the creation of reactive surface sites at different time scales ($\tau_1 \approx$ 0.3 seconds and $\tau_2 \approx 11$ seconds). Which reactive plasma species define these mechanisms is still an open question.

It has been shown how nitrogen plasma species have an important role in creating these reactive sites.[15] In Chapter 5, it has been speculated what the role of ions and radicals is in the film growth and material quality. Profijt *et al.*[12] showed that in many processes in general, surface chemistry is ruled by the radicals. However, in the process as developed in this work, it is likely the ions also play a role. It has been suggested that $N2^+$ ion bombardment helps in the desorption of surface hydrogen and creation of reactive surface sites for atomic [N]-species.[15] Furthermore,

[c] As previously defined in Chapter 4

King [15] suggested that N_2^+ ions can collide with enough energy to break some surface Si-Si and Si-N bonds, which could increase the amount of Si-N bonds and lead to film densification. King [15] furthermore suggested this could partially explain the slow saturation in GPC as function of plasma exposure time. This however, cannot explain the different saturation behaviour observed with films grown by BTBAS and DSBAS. Redeposition could play a role in this, which will be discussed in the next section.

Redeposition of ligand fragments

It has been shown by Knoops *et al.* [21] how redeposition of ligand fragments can lead to increased GPCs and lower quality films, which has already been discussed in Chapter 4 and schematically shown in Figure 4.5. Previously, it has been showed how ligands could remain on the surface, as is depicted in Figure 6.1 for BTBAS. During the subsequent plasma half-cycle, this remaining ligand can detach from the surface and enter the plasma, where it will be fragmented and other reactive species can be formed. If those reactive ligand fragments are not flushed out of the reactor rapidly, a significant amount of these reactive fragments can redeposit on the sample surface again. Knoops *et al.* [21] showed that this redeposition effect is ruled by the residence time, a measure for the time the gas species stay in the reactor before being pumped out. For short plasma exposure times, elevated GPCs and reduced material quality were observed, as a result of ligand fragments that were incorporated into the film. Knoops *et al.* [21] showed that reducing the gas residence time and increasing plasma exposure time reduce the redeposition of contaminant species. However, the composition of the SiN_x films deposited by BTBAS showed significant carbon contents, indicating redeposition still occurred, despite reduced residence times. Similarly, it could be possible some redeposition occurs in the plasma-assisted ALD processes by DSBAS as well. An incomplete ligand split-off reaction could result in DSBAS ligands that remain on the surface upon starting the plasma half-cycle. Also in this case, ligand fragments could enter the plasma, which could lead to redeposition and possible incorporation in the film.

Further experimental work identified CN molecules as one of the reactive ligand fragments, for BTBAS. By studying the emission of the nitrogen plasma during the plasma half-cycle via optical emission spectroscopy, CN* emission was observed.[21] The emission showed a peak in the first seconds of the plasma half-cycle before decreasing over time. These results suggest that ligands were removed from the surface, before being fragmented in the plasma, into for example CN*. The reduction of the signal suggests either the flushing of these reaction products out of the reactor or incorporation into the SiN_x film, or a combination of the two. Proof of the first statement was given by Knoops *et al.* [21], who showed that a reduction in gas residence time resulted in a decrease of the redeposition effect. Proof of the second statement has been given by Cornelissen [20], who identified CN-surface groups present at the surface of films grown by BTBAS at the end of the plasma half-cycle, which is depicted in Figure 6.5. By performing surface-FTIR, before and after the plasma half-cycle, they identified the formation of these triple-bonded CN groups during the plasma half-cycle. These results support how redeposition occurs for SiN_x films deposited by BTBAS, but do not necessarily show this for DSBAS. The similarities in the structure of BTBAS and DSBAS precursors, however, do make plausible that redeposition occurs in a similar way.

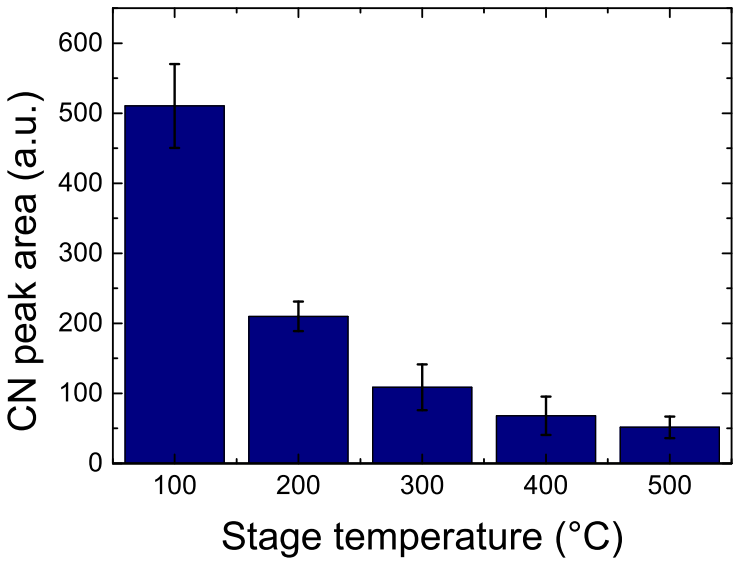

Figure 6.4: C-N peak area as a function of stage temperature, as determined for SiN_x films deposited with DSBAS via XPS.

Experimental results for DSBAS, depicted in Figure 6.4, further support that redeposition occurs for DSBAS. In this figure, it is shown how the amount of CN bonds in the film decrease as a function of increasing stage temperature. This trend is similar to the trend obtained by Braeken *et al.* [18], also for CN bonds in SiN_x films deposited by BTBAS. These results indicate that redeposition of reactive DSBAS ligand fragments, specifically CN, could be incorporated in the SiN_x film, especially at low stage temperatures (< 300 °C).

6.2 Implications regarding the deposition mechanism

The findings described previously in this chapter will be summarised and formed into a proposed reaction mechanism. This mechanism for DSBAS supports a proposed reaction mechanism for BTBAS, which has been proposed by Cornelissen [20] and is depicted in Figure 6.5. This visualisation of the BTBAS reaction mechanism can serve as a reference mechanism for DSBAS. Note that while the proposed BTBAS mechanism is supported by experimental data about the surface species present during both half-cycles, there is no direct evidence available for the DSBAS mechanism yet. As a result, the proposed mechanism is slightly speculative.

In the first half-cycle (A), the precursor enters the reactor. Based on experimentally determined saturation curves, it is expected that the precursor quickly occupies all reactive surface sites. These reactive adsorption sites are likely to consist of under-coordinated nitrogen sites. The DSBAS ligand is removed after the hydrogen transfer from a neighbouring surface group and the remaining

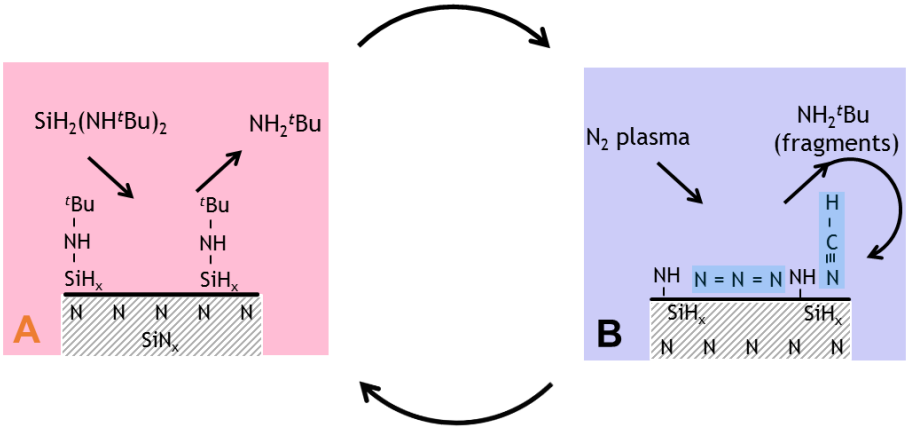

Figure 6.5: Schematic representation of the reaction mechanism of BTBAS using a N_2 plasma.[20] In the precursor half-cycle, BTBAS bonds to the surface, upon the split-off of one of the ligands. In the plasma half-cycle, the remaining ligands are removed and simultaneously, reactive NH bonds are created on the surface. It is shown how reactive ligand fragments can redeposit as for example triple-bonded CN. The images are obtained from Cornelissen[20].

SiH_3 group binds to the surface. However, considering the high activation energies and contamination present in the films, it is possible that not all adsorption reaction reactions did complete fully, especially at low stage temperatures ($<$ 300 °C). In this scenario, the DSBAS ligand would not split off completely and would be present in the reactor during the plasma exposure step.

In the second half-cycle (B), the reactive species present in the nitrogen plasma interact with the surface. Reactive surface sites (under-coordinated nitrogen) are formed in this step. The soft saturation of the GPC as function of plasma exposure step indicates two different reactive sites are created on two different time scales. Furthermore, based on the low [C]- and [H]-content at high deposition temperatures (>300 °C), it is expected that upon igniting the plasma, the vast majority of surface silicon groups consist of SiH_3. At low stage temperatures, it is expected that a significant amount of DSBAS ligand split-off reactions were not completed upon entering the plasma exposure step. This would indicate that ligand fragments entered the plasma and redeposited on the surface, especially at low stage temperatures (<200 °C). The presence of a significant amount of CN-bonds at low stage temperatures supports this hypothesis and agrees with the proposed reaction mechanism for BTBAS, depicted in Figure 6.5. It has to be noted that the cool reactor walls (150 °C[d]) could also play a role in the redeposition.

[d]The maximum temperature of the walls that can be achieved in the FlexAL®-setup

6.2.1 Open questions and outlook

In this chapter aspects regarding the reaction mechanism have been discussed. It has been discussed how the recently proposed reaction mechanism of BTBAS can suit as a reference mechanism for DSBAS. The results obtained support this mechanism, however, some open questions still remain.

It would be interesting to observe the surface species at the beginning and end of the half-cycles and compare those with BTBAS. In-situ diagnostics such as surface-FTIR could be employed to investigate which surface species groups are present after each half-cycle. Furthermore, via mass spectroscopy it could be possible to determine if possible reaction products of the DSBAS ligand are present during the plasma half-cycle. By conducting such an experiment at various temperatures, it might be possible to determine whether redeposition occurs for DSBAS as well. Another recommendation would be to investigate the saturation behaviour at lower stage temperatures. Knoops *et al.* [21] observed a characteristic redeposition peak for BTBAS, when the GPC as function of plasma exposure time was graphed. At low temperatures, it is possible a majority of precursor adsorption reactions are not completed, which could lead to redeposition. This should show up as a peak in GPC as function of plasma exposure time, similarly to what Knoops *et al.* [21] showed. Furthermore it is speculated what the role of ions is in determining film quality and growth. Via biasing the substrate the ion energy can be controlled, which could help in the investigation of the role of the ions in film growth and material properties.

Chapter 7

Conclusion and outlook

In this thesis, several aspects regarding the deposition of silicon nitride (SiN_x) thin films using plasma-assisted atomic layer deposition (ALD) have been discussed. It was shown that SiN_x can have an important function in Field Effect Transistors (FETs), where it serves as a gate spacer to act as a barrier to protect the HKMG stack against water and oxygen ingress and subsequent etch processing steps. Furthermore, it was shown that the SiN_x gate spacer has multiple other functions that can increase FET performance, which become increasingly important in future FET architectures. In order to apply SiN_x films in FETs, it is essential that the deposition temperature is low (< 400 °C). Furthermore, it is important that the SiN_x films simultaneously show high quality and high conformality throughout high-aspect-ratio structures (HARS). Therefore, a new plasma-assisted ALD process was developed employing a novel precursor Di(*Sec*-Butyl)AminoSilane (DSBAS, $SiH_3N(C_4H_9)_2$), after which the material properties were investigated.

Process Development

The main goal of this work comprised *the establishment and development of the silicon nitride plasma-assisted ALD process with DSBAS*. In order to establish the ALD process, a set of saturation experiments was conducted. Typical ALD behaviour was observed by studying growth per cycle (GPC) as a function of precursor dose and purge times. However, GPC as a function of plasma exposure time showed only soft saturation after 20 s of plasma exposure, which was discussed to have implications on the reaction mechanism. The saturation results have resulted in the definition of a standard ALD process. With this process, material properties have been characterised over a wide temperature range (100 - 500 °C). The results have been compared to films grown with a similar precursor BTBAS, of which the process is relatively well-known in our group. It was observed that DSBAS GPC was lower compared to BTBAS. The obtained GPC

values typically lie between 0.01 and 0.02 nm, which was shown to be $\sim$ 1/10th of a monolayer of Si_3N_4. The results further indicate that films grown with DSBAS show higher material quality compared to films grown with a BTBAS precursor and other plasma-assisted ALD processes reported in the literature. This was demonstrated by low C, O, and H content, high mass densities and N/Si values close to stoichiometric Si_3N_4. The high quality was also confirmed by preliminary etch results showing no significant etching of SiN_x deposited on top of planar surfaces.

Conformality

The first sub-goal of this work comprised a study into the conformality of SiN_x films deposited in HARS with DSBAS and BTBAS. High quality films were deposited, showing no significant wet etch-rate on the top surfaces of the HARS. Furthermore, for DSBAS, the wet-etch rate on the horizontal surface on the bottom of the high aspect ratio trench ($\sim$ 1:4.5) was also not significant. The reduced quality on the vertical side-walls of the trench, which became worse at increased plasma pressure, might indicate that ions play a role in determining the quality of the film and the growth in general. Typically, the conformality was not satisfactory: reduced film thickness was observed at the bottom (55-65%) and at the side-bottom (40-55%). The soft saturation of GPC as a function of the plasma exposure time suggests that increased exposure to reactive plasma species leads to an increase in GPC, contrary to typical saturation behaviour. As a result, different regions in the HARS could be exposed to reduced fluxes of reactive plasma species, which was discussed to be one of the causes for the observed differences in conformality.

Aspects regarding the reaction mechanism

The second sub-goal comprised the reaction mechanisms of both the DSBAS and BTBAS precursor. It was shown that the results obtained in this work for DSBAS provide support for a reaction mechanism, as was previously proposed for BTBAS. This mechanism explains how the split-off of the only amino-ligand in a DSBAS-molecule in the precursor half-cycle, reduces redeposition of ligand fragments in the subsequent plasma half-cycle. Furthermore, it was discussed what could limit the GPC in SiN_x film growth by DSBAS. It was discussed how steric hindrance can play a role, but is not likely to be the factor limiting the film growth. Moreover, it has been shown how the number of reactive surface sites is likely to be the factor limiting the SiN_x film growth.

Altogether, the results obtained in this work support the mechanism previously proposed for BTBAS. However, some open questions remain and more experimental work is recommended to be conducted to further prove this reaction mechanism, which will be discussed in the outlook.

XPS benchmark

The third sub-goal comprised the investigation into potential errors and uncertainties in X-ray Photoelectron Spectroscopy (XPS) of SiN_x thin films. Binding energy, peak area and preferential sputtering effects were investigated. It was shown that binding energy and peak area can be

affected as a result of charging and ion induced oxidation. A strategy was described in order to reduce and correct for these effects. It was further demonstrated that preferential sputtering is likely to not be a big issue in the analysis of SiN_x films. The results demonstrated the limitations in determining the absolute film composition with XPS, mainly because no hydrogen can be detected, which is typically present in SiN_x films.

SiN_x applications in FinFETs

A literature study has shown how Field-Effect Transistors have evolved over the years. Fundamentals have been discussed and it was discussed how SiN_x can be applied as a side-wall gate spacer. It was shown that SiN_x films can also be important in defining source and drain regions in FETs, in strain engineering for increasing channel mobility or as a hard mask in spacer defined patterning. By studying the FET manufacturing processes, it was shown that it is vital to deposit SiN_x films of high conformality, uniformity and precise thickness at low substrate temperatures.

7.1 Outlook

The results obtained in this work have led to an increased insight into the film growth of SiN_x films using aminosilane precursors. However, some open questions remain. In this section, a few brief recommendations will be given on how to improve material properties further and on how to provide more support for the proposed reaction mechanism.

Investigation of the effect of plasma exposures on SiN_x film quality

In this work, it was hypothesised how two different sorts of reactive sites are created at two different time scales ($\tau_1 \approx 0.3$ seconds and $\tau_2 \approx 11$ seconds). However, the material properties were not investigated. By characterising the material properties of SiN_x films deposited at different plasma exposure times, more insight into the effect of increased plasma exposure can be gained. The hypothesis that more reactive sites are created at increased plasma exposure times, could then be verified by observing the number of adsorbed silicon atoms per cycle per nm^2. Insight in the material quality as a function of different plasma exposure times could also help in explaining the quality differences observed throughout HARS.

Investigation of the reaction products

It was shown that the results obtained in this work for DSBAS provide support for a reaction mechanism, as was previously proposed for BTBAS. However, a part of the argumentation was based on experimental observations for BTBAS. In order to prove the reaction mechanism is similar, it is advised to conduct *in-situ* experiments to analyse reaction products or surface sites during the separate half-cycles. With for example quadruple mass spectroscopy, the reaction products

present in the reactor during the separate half-cycles could be analysed. By analysing the reaction products in the plasma half-cycle, the hypothesis for DSBAS about the complete ligand split-off can be tested. In case no ligand reaction products are visible in the plasma half-cycle, it is likely the majority of ligands split off in the precursor half-cycle. Furthermore, Cornelissen [20] developed a diagnostic, with which SiN_x film could be analysed via *in-situ* infrared spectroscopy for plasma-assisted ALD of SiN_x films deposited by BTBAS. They were able to identify the change in surface groups during both half-cycles. A similar method could help in identifying surface groups present in the DSBAS process. These experiments could help gaining insight why DSBAS has a high film quality and why the obtained GPC is low.

Additional conformality experiments

The conformality results obtained in this work have shown that conformality throughout the trench and the film quality at vertical side-walls was not satisfactory. A more systematic study has been conducted in order to investigate the effect of an increased plasma exposure and increased precursor dose separately. The experimental conditions are given in Appendix I. The results, however, did not arrive in time in order to be implemented in this thesis. Furthermore, the conformality results have shown how ions can play a role in determining the film quality in HARS. A method to investigate this in more detail would be to specifically control the energy of the ions. Recently, the substrate table in the FlexAL®reactor was upgraded, such that this table can be biased. By controlling the voltage of the substrate table, the ions can be accelerated individually, since the radicals are not charged. Experiments have been planned and are expected to increase the insight into the role of the ions in determining film quality and conformality in the plasma-assisted ALD of SiN_x films.

Density Function Theory (DFT) studies

In this work, preliminary Density Funtional Theory (DFT) results were used in order to compare activation energies between BTBAS and DSBAS. It is expected that these results will increase the understanding of the kinetics involved in the precursor surface reactions and the role of the nitrogen plasma in the creation of reactive sites. The results could also help in the further identification of the reactive sites.

Bibliography

[1] W. Jang, H. Jeon, C. Kang, H. Song, J. Park, H. Kim, H. Seo, M. Leskela, and H. Jeon, "Temperature dependence of silicon nitride deposited by remote plasma atomic layer deposition," Physica Status Solidi (a) **211**, 2166 (2014).

[2] D. H. Triyoso, K. Hempel, S. Ohsiek, V. Jaschke, J. Shu, S. Mutas, K. Dittmar, J. Schaeffer, D. Utess, and M. Lenski, "Evaluation of Low Temperature Silicon Nitride Spacer for High-k Metal Gate Integration," ECS Journal of Solid State Science and Technology **2**, N222 (2013).

[3] C.-H. C. C.-H. Chen, T. Lee, T. Hou, C. Chen, C. Chen, J. Hsu, K. Cheng, Y. Chiu, H. Tao, Y. Jin, C. Diaz, S. Chen, and M.-S. Liang, "Stress memorization technique (SMT) by selectively strained-nitride capping for sub-65nm high-performance strained-Si device application," Digest of Technical Papers. 2004 Symposium on VLSI Technology, 2004. , 56 (2004).

[4] H. Yang, R. Malik, S. Narasimha, Y. Li, R. Divakaruni, P. Agnello, S. Allen, A. Antreasyan, J. Arnold, K. Bandy, M. Belyansky, A. Bonnoit, G. Bronner, V. Chan, X. Chen, Z. Chen, D. Chidambarrao, A. Chou, W. Clark, S. Crowder, B. Engel, H. Harifuchi, S. Huang, R. Jagannathan, F. Jamin, Y. Kohyama, H. Kuroda, C. Lai, H. Lee, W.-H. Lee, E. Lim, W. Lai, A. Mallikarjunan, K. Matsumoto, A. McKnight, J. Nayak, H. Ng, S. Panda, R. Rengarajan, M. Steigerwalt, S. Subbanna, K. Subramanian, J. Sudijono, G. Sudo, S.-P. Sun, B. Tessier, Y. Toyoshima, P. Tran, R. Wise, R. Wong, I. Yang, C. Wann, L. Su, M. Horstmann, T. Feudel, A. Wei, K. Frohberg, G. Burbach, M. Gerhardt, M. Lenski, R. Stephan, K. Wieczorek, M. Schaller, H. Salz, J. Hohage, H. Ruelke, J. Klais, P. Huebler, S. Luning, R. V. Bentum, G. Grasshoff, C. Schwan, E. Ehrichs, S. Goad, J. Buller, S. Krishnan, D. Greenlaw, M. Raab, and N. Kepler, "Dual stress liner for high performance sub-45nm gate length SOI CMOS manufacturing," IEDM Technical Digest. IEEE International Electron Devices Meeting, 2004. , 1075 (2004).

[5] K. S. K. Shin, C. O. C. C. O. Chui, and T.-J. K. T.-J. King, "Dual stress capping layer enhancement study for hybrid orientation finFET CMOS technology," IEEE International-Electron Devices Meeting, 2005. IEDM Technical Digest. **00**, 0 (2005).

[6] H. Cho, P. Kapur, P. Kalavade, and K. Saraswat, "A Novel Spacer Process for Sub-10-nm-Thick Vertical MOS and Its Integration With Planar MOS Device," IEEE Transactions On Nanotechnology **5**, 554 (2006).

[7] F. Koehler, D. H. Triyoso, I. Hussain, B. Antonioli, and K. Hempel, "Challenges in spacer process development for leading-edge high-k metal gate technology," physica status solidi (c) **11**, 73 (2014).

[8] R. a. Ovanesyan, D. M. Hausmann, and S. Agarwal, "Low-Temperature Conformal Atomic Layer Deposition of SiNx Films Using Si2Cl6 and NH3 Plasma," ACS Applied Materials & Interfaces **7**, 10806 (2015).

[9] F. Koehler, D. H. Triyoso, I. Hussain, S. Mutas, and H. Bernhardt, "Atomic Layer Deposition of SiN for spacer applications in high-end logic devices," IOP Conference Series: Materials Science and Engineering **41**, 012006 (2012).

[10] P. Morin, G. Raymond, D. Benoit, D. Guiheux, R. Pantel, F. Volpi, and M. Braccini, "Study of stress in tensile nitrogen-plasma-treated multilayer silicon nitride films," Journal of Vacuum Science & Technology A: Vacuum, Surfaces, and Films **29**, 041513 (2011).

[11] D. H. Triyoso, V. Jaschke, J. Shu, S. Mutas, K. Hempel, J. K. Schaeffer, and M. Lenski, "Robust PEALD SiN spacer for gate first high-k metal gate integration," , 9 (2012).

[12] H. B. Profijt, P. Kudlacek, M. C. M. van de Sanden, and W. M. M. Kessels, "Ion and Photon Surface Interaction during Remote Plasma ALD of Metal Oxides," (2011).

[13] H. Goto, K. Shibahara, and S. Yokoyama, "Atomic layer controlled deposition of silicon nitride with self-limiting mechanism," Applied Physics Letters **68**, 3257 (1996).

[14] H. C. M. Knoops, E. M. J. Braeken, K. de Peuter, S. E. Potts, S. Haukka, V. Pore, and W. M. M. Kessels, "Atomic Layer Deposition of Silicon Nitride from Bis(tert-butylamino)silane and N2 plasma," ACS Applied Materials & Interfaces (2015).

[15] S. W. King, "Plasma enhanced atomic layer deposition of SiNx:H and SiO2," Journal of Vacuum Science & Technology A: Vacuum, Surfaces, and Films **29**, 041501 (2011).

[16] S. Yokoyama, H. Goto, T. Miyamoto, N. Ikeda, and K. Shibahara, "Atomic layer controlled deposition of silicon nitride and in situ growth observation by infrared reflection absorption spectroscopy," Applied Surface Science **112**, 75 (1997).

[17] C. A. Murray, S. D. Elliott, D. Hausmann, J. Henri, and A. Lavoie, "Effect of Reaction Mechanism on Precursor Exposure Time in Atomic Layer Deposition of Silicon Oxide and Silicon Nitride," ACS Applied Materials & Interfaces **6**, 10534 (2014).

[18] E. M. J. Braeken, C. M. Knoops, S. E. Potts, and W. M. M. Kessels, *Development and understanding of a plasma-assisted atomic layer deposition process for silicon nitride*, Msc. thesis (2013).

[19] K. de Peuter, *Mechanisms controlling silicon nitride growth by plasma-enhanced atomic layer deposition*, Msc. thesis (2014).

[20] L. Cornelissen, *In situ infrared spectroscopy for plasma-assisted ALD of SiNx films*, Msc. thesis (2015).

[21] H. C. M. Knoops, K. de Peuter, and W. M. M. Kessels, "Redeposition in plasma-assisted atomic layer deposition: Silicon nitride film quality ruled by the gas residence time," Applied Physics Letters **107**, 014102 (2015).

[22] G. E. Moore, "Creaming more components onto integrated circuits," Electronics **38**, 114 (1965).

[23] H. B. Profijt, *Plasma-Surface Interaction in Plasma-Assisted Atomic Layer Deposition*, Ph.D. thesis (2012).

[24] N. Storey, *Electronics A Systems Approach* (Pearson Education Limited, 2006).

[25] R. Clark, "Emerging Applications for High K Materials in VLSI Technology," Materials **7**, 2913 (2014).

[26] J. Robertson and R. M. Wallace, "High-K materials and metal gates for CMOS applications," Materials Science and Engineering: R: Reports **88**, 1 (2015).

[27] E. Seebauer and P. Gorai, *Comprehensive Semiconductor Science and Technology* (Elsevier, 2011) pp. 86–131.

[28] P. Colinge, *FinFETs and Other Muli-Gate Transistors* (2008).

[29] K. T. Gibb, "Tracing Samsung's Road to 14nm," (2015).

[30] R. H. Dennard, F. H. Gaensslen, H.-N. Yu, V. L. Rideovt, E. Bassous, and A. R. Leblanc, "Design of Ion-Implanted MOSFET's with Very Small Physical Dimensions," IEEE Journal of Solid-State Circuits **SC-9**, 256 (1974).

[31] M. Bohr, "A 30 Year Retrospective on Dennard's MOSFET Scaling Paper," IEEE Solid-State Circuits Newsletter **12**, 3 (2007).

[32] K. Nojiri, *Dry Etching Technology for Devices of Compound Semiconductor* (2013).

[33] J. Hruska, "This is what the death of Moore's law looks like: EUV rollout slowed, 450mm wafers halted and an uncertain path beyond 14nm," (2014).

[34] T. Ludwig, I. Aller, V. Gernhoefer, J. Keinert, E. Nowak, R. Joshi, A. Mueller, and S. Tomaschko, "FinFET technology for future microprocessors," SOI Conference, 2003. IEEE International , 33 (2003).

[35] B. Degroote, R. Rooyackers, T. Vandeweyer, N. Collaert, W. Boullart, E. Kunnen, D. Shamiryan, J. Wouters, J. Van Puymbroeck, A. Dixit, and M. Jurczak, "Spacer defined FinFET: Active area patterning of sub-20 nm fins with high density," Microelectronic Engineering **84**, 609 (2007).

[36] A. Loke, "The Journey to FinFETs," in *IEEE San Diego - CPMT Chapter & AP/MTT/ED/SSC/CAS Joint Chapter* (2015) pp. 1—-105.

[37] K. J. Kuhn, "Considerations for ultimate CMOS scaling," IEEE Transactions on Electron Devices **59**, 1813 (2012).

[38] R. Roelofs, *Energy-Enhanced ALD for Nano-manufacturing by Direct Spacer-Defined Double Patterning*, Ph.D. thesis (2012).

[39] X. Cai, R. Xie, and W. J. Taylor JR., "Methods of Forming Spacers on FinFETs and other Semiconductor Devices," (2015).

[40] B. Moyer, "Gate First vs Last," (2011).

[41] A. Kaneko, A. Yagishita, K. Yahashi, T. Kubota, M. Omura, K. Matsuo, I. Mizushima, K. Okano, H. Kawasaki, S. Inaba, T. Izumida, T. Kanemura, N. Aoki, K. Ishimaru, H. Ishiuchi, K. Suguro, K. Eguchi, and Y. Tsunashima, "Sidewall transfer process and selective gate sidewall spacer formation technology for sub-15nm finfet with elevated source/drain extension," IEEE InternationalElectron Devices Meeting, 2005. IEDM Technical Digest. **00** (2005), 10.1109/IEDM.2005.1609488.

[42] V. S. Basker, C. Kangguo, B. B. Doris, and J. E. Faltermeier, "FinFET spacer formation by oriented implantation," (2014).

[43] C. H. Ko, T. M. Kuan, K. Zhang, G. Tsai, S. M. Seutter, C. H. Wu, T. J. Wang, C. N. Ye, H. W. Chen, C. H. Ge, K. H. Wu, and W. C. Lee, "A novel CVD-SiBCN low-K spacer technology for high-speed applications," Digest of Technical Papers - Symposium on VLSI Technology **39**, 108 (2008).

[44] K. Endo, Y. Ishikawa, T. Matsukawa, Y. Liu, S. I. O'Uchi, K. Sakamoto, J. Tsukada, H. Yamauchi, and M. Masahara, "Enhancement of FinFET performance using 25-nm-thin sidewall spacer grown by atomic layer deposition," Solid-State Electronics **74**, 13 (2012).

[45] S. B. S. Heil, J. L. van Hemmen, C. J. Hodson, N. Singh, J. H. Klootwijk, F. Roozeboom, M. C. M. van de Sanden, and W. M. M. Kessels, "Deposition of TiN and \ce{HfO_2}in a commercial 200 mm remote plasma atomic layer deposition reactor," Journal of Vacuum Science & Technology A: Vacuum, Surfaces, and Films **25**, 1357 (2007).

[46] E. Langereis, S. B. S. Heil, H. C. M. Knoops, W. Keuning, M. C. M. van de Sanden, and W. M. M. Kessels, "Spectroscopic Ellipsometry As a Versatile Tool for Studying Atomic Layer Deposition," Journal of Physics D: Applied Physics **42**, 073001 (2009).

[47] N. Manavizadeh, A. Khodayari, and E. Asl-soleimani, "An Investigation of The Properties of Silicon Nitride (SiNx) Thin Films Prepared by Sputtering for Application in Solar Cell Technology," in *World Solar Energy Conference* (2007) pp. 1–3.

[48] R. L, *Transmission Electron Microscopy: Physics of Image Formation and Microanalysis* (2013).

[49] J. B. Metson, "Charge compensation and binding energy referencing in XPS analysis," Surface and Interface Analysis **27**, 1069 (1999).

[50] S. Morishita, S. Sugahara, and M. Matsumura, "Atomic-layer chemical-vapor-deposition of silicon-nitride," (1997).

[51] J. Klaus, A. Ott, A. Dillon, and S. George, "Atomic layer controlled growth of Si3N4 films using sequential surface reactions," Surface Science **418**, L14 (1998).

[52] W.-j. Lee, U.-j. Kim, and Y.-s. Lee, "Characteristics of Silicon Nitride Thin Films Prepared by Using Alternating Exposures of SiH 2 Cl 2 and NH 3," **47**, 598 (2005).

[53] K. Park, W. D. Yun, B. J. Choi, H. D. Kim, W. J. Lee, S. K. Rha, and C. O. Park, "Growth studies and characterization of silicon nitride thin films deposited by alternating exposures to Si2Cl6 and NH3," Thin Solid Films **517**, 3975 (2009).

[54] S. Riedel, J. Sundqvist, and T. Gumprecht, "Low temperature deposition of silicon nitride using Si3Cl8," Thin Solid Films **577**, 114 (2015).

[55] C. Ande, H. C. M. Knoops, K. de Peuter, M. van Drunen, S. D. Elliott, and W. Kessels, "Role of Surface Termination in Atomic Layer Deposition of Silicon Nitride," Journal of Physical Chemistry Letters **6**, 3610 (2015).

[56] F. L. Riley, "Silicon Nitride and Related Materials," Journal of the American Ceramic Society **83**, 245 (2000).

[57] A. Mallikarjunan, H. Chandra, M. Xiao, X. Lei, R. M. Pearlstein, H. R. Bowen, M. L. O 'neill, A. Derecskei-Kovacs, and B. Han, "Designing high performance precursors for atomic layer deposition of silicon oxide," Journal of Vacuum Science & Technology A Appl. Phys. Lett **33**, 1 (2015).

[58] R. L. Puurunen, "Surface chemistry of atomic layer deposition: A case study for the trimethylaluminum/water process," Journal of Applied Physics **97**, 121301 (2005).

[59] H. C. M. Knoops, E. Langereis, M. C. M. van de Sanden, and W. M. M. Kessels, "Conformality of Plasma-Assisted ALD: Physical Processes and Modeling," Journal of The Electrochemical Society **157**, G241 (2010).

[60] H. B. Profijt, S. E. Potts, M. C. M. van de Sanden, and W. M. M. Kessels, "Plasma-Assisted Atomic Layer Deposition: Basics, Opportunities, and Challenges," Journal of Vacuum Science & Technology A: Vacuum, Surfaces, and Films **29**, 050801 (2011).

[61] L. Huang and B. Han, "Density functional theory study on the full ALD process of silicon nitride thin film deposition via BDEAS or BTBAS and NH 3," Physical Chemistry ... **16**, 18501 (2014).

[62] K. A. Perrine and A. V. Teplyakov, "Reactivity of selectively terminated single crystal silicon surfaces." Chemical Society reviews **39**, 3256 (2010).

[63] J. F. Moulder, W. F. Stickle, P. E. Sobol, and K. D. Bomben, *Handbook of X-ray Photoelectron Spectroscopy* (1995) pp. 9–261.

[64] L. Meng, X. Zhang, Y. Tang, K. Su, and J. Kong, "Hierarchically porous silicon-carbon-nitrogen hybrid materials towards highly efficient and selective adsorption of organic dyes," Scientific Reports **5**, 1 (2015).

[65] L. Muehlhoff, W. J. Choyke, M. J. Bozack, and J. T. Yates, "Comparative electron spectroscopic studies of surface segregation on SiC(0001) and SiC(0001??)," Journal of Applied Physics **60**, 2842 (1986).

[66] N.-m. Park, S. H. Kim, and G. Y. Sung, "Amorphous Silicon Carbon Nitride Films Grown by the Pulsed Laser Deposition of a SiC-Si 3 N 4 Mixed Target," ETRI Journal **26**, 257 (2004).

[67] "XPS Knowledge Base," .

[68] "NIST X-ray Photoelectron Spectroscopy Database," .

[69] T. Goto and T. Hirai, "ESCA study of amorphous CVD Si3N4-BN composites," Journal of Materials Science Letters **7**, 548 (1988).

[70] J. R. Shallenberger, D. a. Cole, and S. W. Novak, "Characterization of silicon oxynitride thin films by x-ray photoelectron spectroscopy," Journal of Vacuum Science & Technology A: Vacuum, Surfaces, and Films **17**, 1086 (1999).

[71] P. R. Gray, P. J. Hurst, S. H. Lewis, and R. G. Meyer, *Analysis and Design of Analog Integrated Circuits* (2009) p. 896.

[72] W. Kessels, F. J. H. Van Assche, J. Hong, D. Schram, and M. Van de Sanden, "Plasma diagnostic study of silicon nitride film growth in a remote Ar-H2-N2-SiH4 plasma: Role of N and SiH N radicals," Journal of Vacuum Science & Technology A **22**, 96 (2004).

Appendix

Appendix A

MSDS

The purity of the N_2 gas was 99.9999%, the purity of the Ar gas was 99.999%.

Table A.1: An overview of the purity and characteristics of the materials used in this work. The purity is defined via an assay by gas chromatography (GC), which means that 99.7% of the volatile material which was eluted through the GC column was DSBAS.

Material	Assay by GC	Supplier
DSBAS	$\geq$ 99 %	Airproducts Inc.
BTBAS	$\geq$ 98.5%	Airproducts Inc.

Appendix B

Residence time

The following relation for the residence time has been determined by de Peuter [19]:

$\tau = \frac{pV}{p_0 q_{MFC}}$

In this relation, p is the pressure in the reactor in mTorr, V is the effective volume of the reactor ($\sim$ 13.8 +/- 0.4 l)[a], p_0 is the standard pressure of 760 mTorr and q_{MFC} is the particle flux through the mass flow controller (MFC) in standard cubic centimetre per minute (sccm).

[a] The effective volume of the reactor was estimated by determining the change in pressure over time, while filling the sealed reactor with various gas flows (5 and 10 sccm) using a calibrated mass flow controller.

Appendix C

Coupon sample lay-out

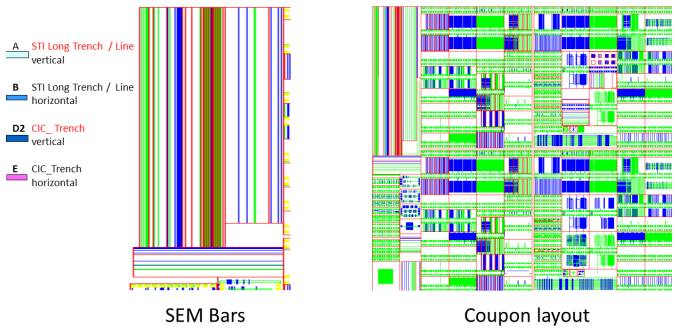

Figure C.1: Schematic representation of the sample lay-out of the coupons, containing HARS.

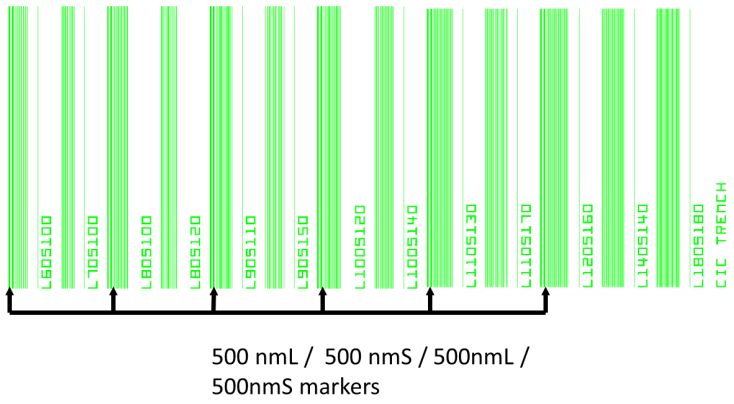

Figure C.2: Schematic representation of the sample lay-out of the coupons, containing HARS.

Appendix D

Uniformity

The uniformity has been studied by analysing SiN_x films deposited on 8 inch wafers. To this end, 8 inch wafers have been mapped in order to obtain spatially resolved thickness profiles. These experiments were performed at Roth & Rau B.V. using specific mapping software. A Cauchy model has been employed to analyse film thickness.

The results show that the uniformity is not 100%. It can be observed that the thickness decreases as a function of wafer diameter. The uniformity difference can be caused by either limited precursor or plasma interaction with the complete surface. However, considering the low pressure and long soaking time, it can be assumed that the precursor has spread out quickly and homogeneously over the reactor and is not causing the limited uniformity. Furthermore, the circle-symmetry of the thickness profile suggests that the flux of plasma species, which originates from the ICP source located in the middle and on the top of the reactor, is responsible for the limited uniformity. Since the samples considered in this work were positioned in the middle of the substrate table, it is assumed the limited uniformity does not play a role in the results obtained in this work.

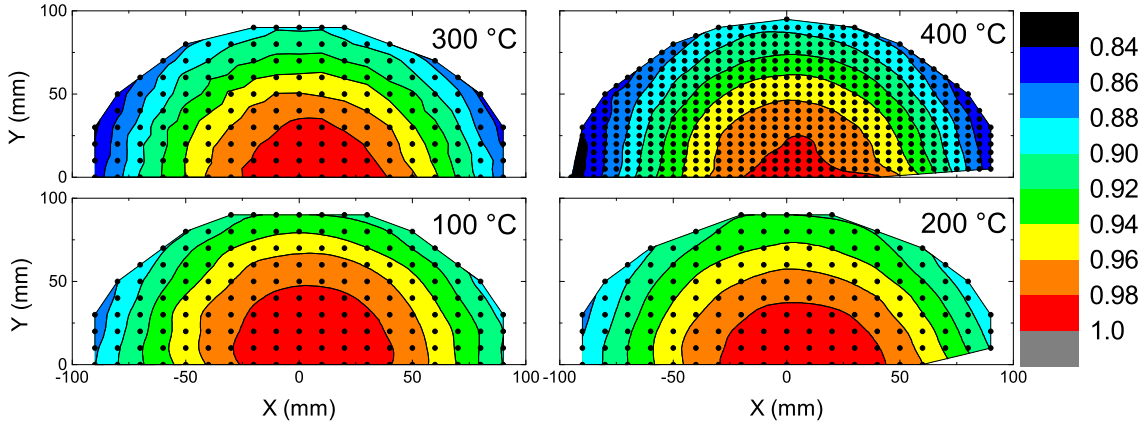

Figure D.1: Normalised thickness of the wafer as function of position on the wafer measured over a range in stage temperatures (100-400 °C). The wafer thickness is normalised on the maximum wafer thickness in the center of the wafer.

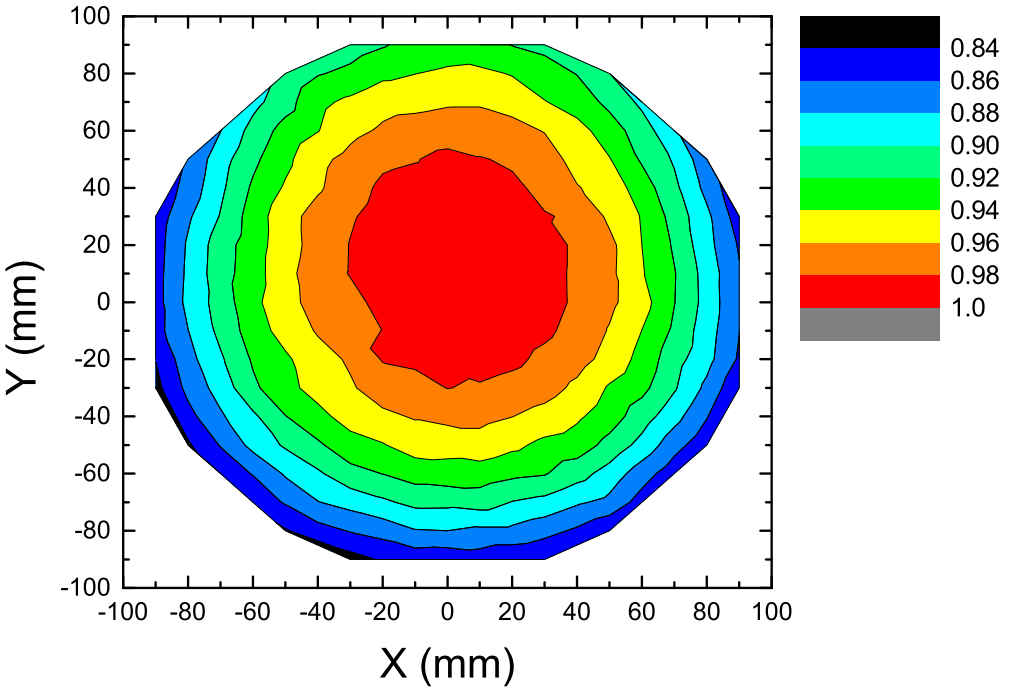

Figure D.2: Normalised thickness of the wafer as function of position on the wafer measured at 500 °C. The wafer thickness is normalised on the maximum wafer thickness in the center of the wafer.

Appendix E

XPS

E.1 XPS results

E.1.1 Stoichiometry at 200 °C

The effect of varying ion beam energy on stoichiometry, measured at a temperature of 200 °C.

Table E.1: The effect of varying ion beam energy during the sputter step on the film stoichiometry, at 200 °C. RBS reference values are used to compare with.

Ion Beam Energy (eV)	[C] at.%	[O] at.%	[Si] at.%	[N] at.%	N/Si [H] corr
200	4.1	3.4	37	49	1.3
1000	4.1	3.7	36	49	1.3
3000	4.2	4.2	37	47	1.3
RBS ref	3 +/- 1.2	4.3 +/- 0.6	35 +/- 0.5	50 +/- 1	1.4 +/- 0.1

E.1.2 XPS binding energy

The binding energy of deconvoluted XPS peaks has been determined for SiN_x films deposited at various stage temperatures.

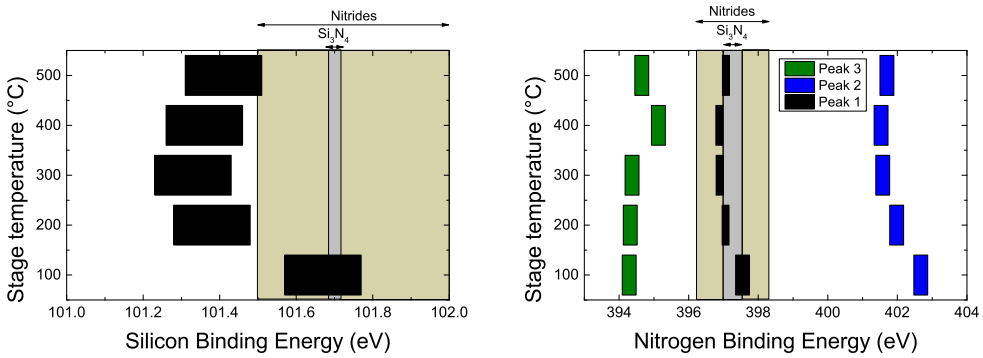

Figure E.1: The binding energy of the deconvoluted peaks for silicon (left) and nitrogen (right) as a function of stage temperature.

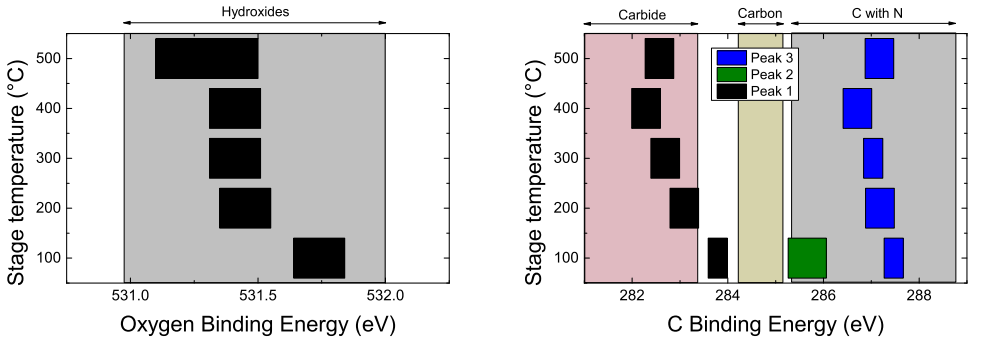

Figure E.2: The binding energy of the deconvoluted peaks for oxygen (left) and carbon (right) as a function of stage temperature.

E.1.3 XPS peak area

The peak area of deconvoluted XPS peaks has been determined for SiN_x films deposited at various stage temperatures.

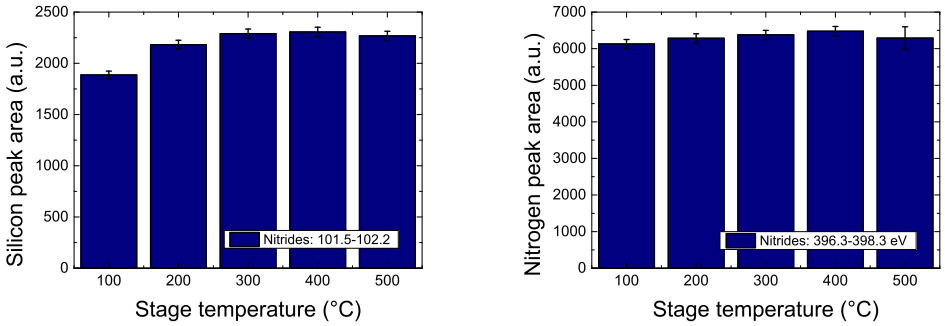

Figure E.3: The peak area of the deconvoluted peaks for silicon (left) and nitrogen (right) as a function of stage temperature.

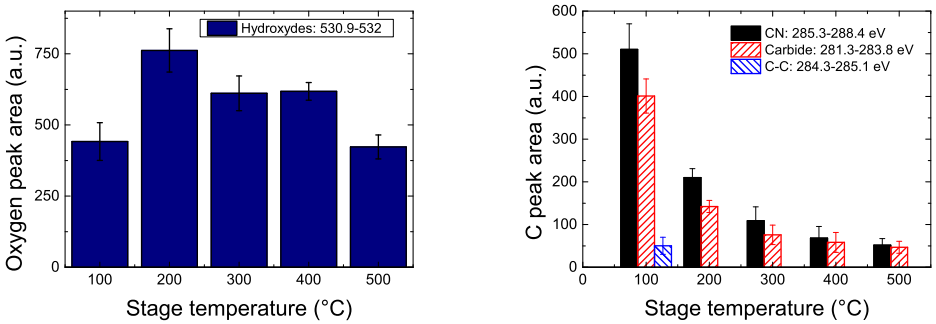

Figure E.4: The peak area of the deconvoluted peaks for oxygen (left) and carbon (right) as a function of stage temperature.

Table E.2: The sensitivity factors used in this work

	C1s	O1s	Si2p3	Si2p1	N1s
Sensitivity factor:	1.000	2.881	0.596	0.304	1.676

E.2 XPS sensitivity factors

The sensitivity factors used in this work are given in Table E.2.

E.3 XPS literature values

Table E.3: An overview showing reference XPS peak values of [Si], [N], [C] and [O] bonds. For comparison purposes, XPS bible and NIST database have often been used as reference values.

[Si]		[N]		[C]		[O]	
Bond	Peak Range (eV)	Bond	Peak Range (eV)	Bond	Peak Range (eV)	Bond	Peak Range (eV)
Silicon	98.8 - 99.5 [63]	Si-N-C	369.9 [64]	Carbides	281.3 - 283.4 [63]	Hydroxides	530.9 - 532 [63]
Carbides	99.9 - 100.8 [63]	Si-N-Si	398 [64]	Si-C	283.6 [65]		
Nitrides	101.5 - 102.2 [63]	Si-N-O	399.2 [64]	C-N	285.3 - 288.4 [63]	Si-C:O	532 [66]
Si_3N_4	101.7 [67]	N-(Si,O)	400 [66]	C-O	286.1 - 289.3 [63]	Nitrates	532.6 - 533.7 [63]
Si-C	100.3 [68]	Si_3N_4	397.7 [69]	C-C	284.3 - 285.1 [63]		
		Si_3N_4	397.1 - 397.7 [63]	C-C	284.8 [67]	SiO_2	532.6-533.3 [63]
		Nitrides	396.3 - 398.3 [63]				
		NH_3	398.8 - 399.7 [63]				
		$Si-N(-H)_2$	399.7 - 401.0 [70]				

Appendix F

FET: additional information

F.1 Saturation current

The saturation current I_d^{sat} of a MOSFET can be calculated by the following relation[71]:

$I_d^{sat} \propto \frac{W}{L} \mu C_{inv} \frac{(V_{gs}-V_{th})^2}{2}$

In this relation W indicates the width of the parallel plate in cm, L indicates the length of the plate in cm and the channel length in a MOSFET, μ the mobility of the mobile carriers in the channel (in $\frac{cm^2}{V \cdot s}$) and the width of the channel, C_{inv} the capacitance in F, V_{gs} the gate source voltage and V_{th} the threshold voltage.

F.2 Mobility

Carrier mobility is defined as $\mu = \frac{q\tau}{m^*}$ in which q is the elementary charge of the carrier, τ is the mean scattering time and m^* the effective mass of the carrier.

Appendix G

Saturation of the GPC as function of the plasma exposure time

The GPC as function of the plasma exposure time showed soft saturation. The data was fitted with the following relation:

GPC$= A_1(1-\exp\frac{-t}{\tau_1})+A_2(1-\exp\frac{-t}{\tau_2})$

In this relation A_1 and A_2 are derived weighing parameters with values $A_1 = 0.05$ and $A_2 = 0.06$. In the aforementioned relation τ_1 and τ_2 are derived time constants with values $\tau_1 = 0.3s$ and $\tau_2 = 11.0s$. The adjusted R-square value, a measure of the accuracy of the fitting model, is 0.995.

Appendix H

Nitrogen radical recombination

In this section an estimation will be made of the upper limit of the radical recombination rate of nitrogen radicals interacting with a SiN_x surface. In order to draw this conclusion, it will be referred to experiments performed by Kessels *et al.* [72], who investigated the nitrogen density as a function of SiH_4 flow, depicted in Figure H.1 **(b)**.

When there is no SiH_4 flow, SiN_x film growth will be zero and no radicals will be incorporated in the SiN_x film. In the Figure, however, it can be seen that the nitrogen radical density is relatively low at a SiH_4 flow rate of zero. In this case, the only loss source for nitrogen radicals occurs from recombination with the reactor wall, which is made of stainless steel. In Figure H.1 **(b)** it can be observed how an initial increase in SiH_4 flow to 2 sccs increases the density of radicals in the plasma by a factor of ~ 6. The reactor wall is now coated with SiN_x instead of stainless steel, in steady state situation. In this case, two loss-mechanisms apply. Both the built-in of nitrogen radicals in the SiN_x film which is depositing at the reactor walls and recombination of radicals at the reactor wall, on which now a SiN_x film is now deposited, are expected to lead to a loss of nitrogen radicals. Those two cases can be compared, briefly summarising: 1) no flow, with the only loss mechanisms being recombination at the stainless steel surface, and 2) a SiH_4 flow, with which nitrogen radicals are lost at the SiN_x reactor wall or with which nitrogen radicals are built in the SiN_x film. Since the nitrogen density increases in the second case, by a factor of six, it can be concluded that the recombination rate of radicals at the SiN_x surface is at least six times lower than the recombination rate of radicals at stainless steel. Assuming that the SiN_x film growth is positive, which should lead to even more radicals that are lost. In Figure H.1 **(a)** it can be seen that the surface loss probability of nitrogen radicals at a stainless steel surface is ~ 0.05 at 20 mTorr, which is a typical pressure for the experiments conducted in this work. As a result it can be estimated that the nitrogen radical recombination rate at the SiN_x surface is < 0.01.

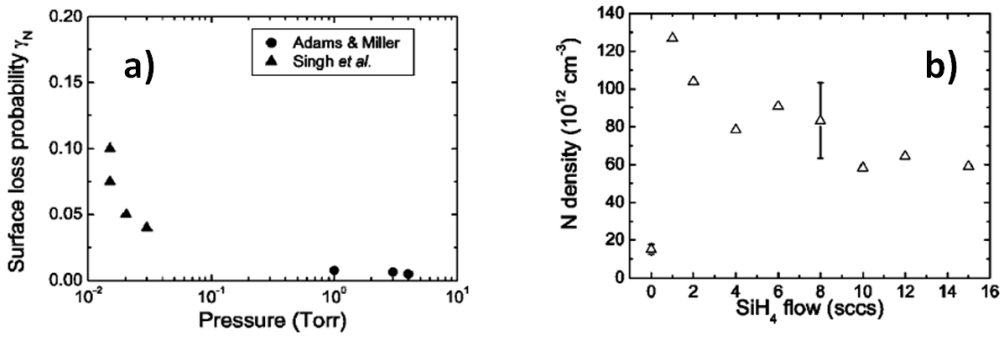

Figure H.1: Nitrogen recombination rate at stainless steel surfaces as function of reactor pressure **a)** and nitrogen density as function of silane (SiH_4) flow, as determined by Kessels *et al.* [72].

Appendix I

Overview conformality experiments

Table I.1: Process parameters and optical properties of SiN_x films deposited with DSBAS in the conformality study of HARS (trenches with AR 1:4.5), described in Chapter 5. The experiments highlighted in grey were carried out, but the results could not yet be included into this thesis. Optical properties are determined via SE. The typical uncertainty in the film thickness, GPC and refractive index is given in the first row.

Experiment: Parameter	Standard	Longer prec and plasma	Increase of pressure extra Ar flow	Lowered temperature	Longer plasma	Longer prec.	Extreme prec. and plasma	Extreme prec. and plasma
Set temperature	500 °C	500 °C	500 °C	300 °C	500 °C	500 °C	500 °C	500 °C
Plasma pressure	12 mTorr	12 mTorr	80 mTorr	12 mTorr	12 mTorr	12 mTorr	12 mTorr	12 mTorr
Flow	100 sccm N_2	100 sccm N_2	100 sccm N_2 200 sccm Ar	100 sccm N_2	100 sccm N_2	100 sccm N_2	100 sccm N_2	100 sccm N_2
Precursor	DSBAS	DSBAS	DSBAS	DSBAS	DSBAS	DSBAS	DSBAS	DSBAS
Precursor dose	100 ms	500 ms	500 ms	500 ms	100 ms	500 ms	1s	2s
Plasma exposure	10 s	20 s	20 s	20 s	20 s	10 s	40 s	40 s
Film thickness	22 +/- 1 nm	26 nm	23 nm	23	24 nm	23 nm	20 nm	22 nm
GPC	0.09 +/- 0.02 Å	0.15	0.13	0.15	0.11	0.13	0.19	0.22
Refractive index	1.98 +/- 0.03	1.94	1.93	1.92	1.99	2.02	1.99	2.00